Antonio Jesús López Quiñones

The Roles of the Polyspecific Organic Cation Transporters in the Disposition of *meta*-Iodobenzylguanidine and Implications for Toxicities and Drug Interactions

Antonio Jesús López Quiñones

A dissertation

submitted in partial fulfillment of the

requirements for the degree of

Doctor of Philosophy

University of Washington

2021

Reading Committee:

Joanne Wang, Chair

Edward Kelly

Yvonne Lin

Program Authorized to Offer Degree:

Pharmaceutics

University of Washington

Abstract

The Roles of the Polyspecific Organic Cation Transporters in the Disposition of *meta*-iodobenzylguanidine and its Implications for Toxicities and Drug Interactions

Antonio Jesús López Quiñones

Chair of the Supervisory Committee:
Professor Joanne Wang
Department of Pharmaceutics

meta-Iodobenzylguanidine (mIBG) is a radiopharmaceutical used as diagnostic agent and a targeted radiotherapy for neuroendocrine cancers. ^{131}I-mIBG enters the cancer cells through the human norepinephrine transporter (hNET) where radioactive decay of ^{131}I causes DNA damage, cell death, and tumor necrosis. Despite its selective accumulation in neuroendocrine tumors, mIBG distributes in several normal tissues and leads to tissue-specific radiation toxicities. The overall goal of this dissertation is to understand the mechanisms involved in the pharmacokinetics and tissue distribution of mIBG. The studies were designed to: 1) characterize the uptake kinetics and interactions of the polyspecific organic cation transporters and their role in the disposition of mIBG and 2) elucidate the impact of organic cation transporter 3 (OCT3) on the pharmacokinetics and tissue distribution of mIBG.

To characterize the contribution of the human organic cation transporter 1, 2, and 3 (hOCT1, hOCT2, and hOCT3) and the human multidrug toxin and extrusion protein 1 and 2-K

(hMATE1 and hMATE2-K), we conducted *in vitro* uptake and inhibition assays in HEK293 cells transfected with the transporters. We showed that mIBG is efficiently transported by hOCT1-3 and hMATE1/2-K with comparable uptake kinetics to hNET. We further demonstrated that mIBG is transported across a hOCT2h/MATE1 double-transfected MDCK monolayer, suggesting that the hOCT2/hMATE pathway is involved in renal secretion of mIBG. We conducted an inhibition screen of mIBG uptake by anticancer drugs used for neuroblastoma and showed that irinotecan selectively inhibited hOCT1 while crizotinib preferentially inhibited hOCT3. We proposed that the polyspecific organic cation transporters mediate the tissue distribution and elimination of mIBG and these transporters can be targeted to reduce tissue accumulation and toxicity, enhance the tumor-to-tissue uptake ratio, and predict and prevent adverse drug interactions for mIBG.

To elucidate the impact of OCT3 on the pharmacokinetics and tissue distribution of mIBG, we conducted an *in vivo* pharmacokinetic and biodistribution study in a Oct3 knockout mouse model. We first developed and validated a bioanalytical LC-MS/MS method for the quantification of non-radiolabeled mIBG in plasma and tissue samples. We demonstrated that the method was accurate, specific, and was devoid of matrix effects in the different biological matrices. The pharmacokinetic data revealed that intact mIBG accumulates in the thyroid, a site of long-term and severe hypothyroidism in neuroendocrine patients. Deletion of Oct3 did not affect the plasma pharmacokinetics of mIBG. Most importantly, we found that Oct3 is a key facilitator for accumulation of mIBG in the heart. In contrast to the conventional but unproven notion that cardiac mIBG uptake is mediated by the norepinephrine transporter, this study in Oct3 knockout mice unequivocally showed that approximately 83% of mIBG exposure in the heart is mediated by OCT3. OCT3-mediated uptake of mIBG in the heart is likely responsible

for the severe cardiotoxicities seen in neuroendocrine cancer patients receiving ^{131}I-mIBG therapy. Besides its use in radiotherapy for neuroendocrine cancers, ^{123}I-mIBG is FDA-approved for cardiac imaging and evaluation of heart failure and ventricular arrhythmias. Thus, our finding that OCT3 is the major determinant for mIBG uptake in the heart has important diagnostic implications for ^{123}I-mIBG imaging of cardiovascular diseases. In addition to the reduced accumulation in the heart, deletion of Oct3 reduced the accumulation of mIBG in the skeletal muscle, salivary glands, and the lung. These data indicate that reducing OCT3 activity can lead to drastic changes to tissue exposure of mIBG and may reduce toxicities of ^{131}I-mIBG therapy.

In summary, this dissertation research has greatly contributed to our understanding of the mechanisms involved in the disposition, toxicity, and drug interactions of mIBG. A clinically relevant finding of this research is that OCT3 is a key determinant of tissue accumulation of mIBG in several tissues, especially in the heart. Ultimately, these findings will help introduce clinical strategies in modulating OCT3 activity to improve the diagnosis and therapeutic efficacy of mIBG in neuroendocrine cancers and other diseases.

TABLE OF CONTENTS

LIST OF FIGURES

LIST OF TABLES

ACKNOWLEDGEMENTS

My time at the University of Washington has been the most rewarding academic experience I have had. The writing of this dissertation has been a bittersweet and emotional ride as it ends a chapter of my life and opens up a wide window of opportunities. My research accomplishments depicted in this dissertation are all thanks to the people who have supported me throughout this journey.

First of all, I thank my mentor, Joanne Wang, for her guidance and patience with me these past few years. She accepted me into her lab during a difficult time in my life and helped me grow as a person and as a scientist. I treasure her never-ending support in me and our fruitful conversations about life and science. She has instilled in me confidence in my strengths and acceptance of my weaknesses. She has been instrumental in getting me to this stage of my scientific career. And of course, I am grateful for the solid understanding of pharmacokinetics and critical thinking she helped me build.

To my thesis committee, Yvonne Lin, Ed Kelly, Bhagwat Prasad, and Edith Wang, I would like to thank you all for your insights and time on my dissertation research. I am thankful for your questions and suggestions that you all provided me during examinations. Thank you, Ed and Yvonne, for reading this dissertation and all your advice and comments. Thank you, Bhagwat, for staying on my committee after moving to WSU and for your mentorship on my proteomic research. And thank you, Edith, for your comments and being my GSR.

To the past members of the Wang Lab, I am thankful for all your support and encouragement when I first joined the lab. I appreciate you all for the time and willingness to help me with research and all the wonderful conversations we had. And a thank you to the

current members of the lab, Austin and Leticia (and Tim), who made Wang Lab feel like home. I truly appreciate both of you and cannot express well in words how thankful I am to you both. I have appreciated our insightful conversations throughout our times in the Wang Lab. You are my academic siblings, and I am stoked to continue growing as scientists with you and seeing where our paths take us.

I would also like to thank my roommate, Chris, and all of my classmates for all the wonderful experiences these past few years. Thank you all for the support, friendship, and all the great food, drinks, and games we have shared. You all made my graduate career enjoyable, and I thank you all for creating such a positive environment for me. I would also like to extend my thanks to all the faculty and staff in the department of pharmaceutics who created supportive community fit for learning.

Lastly, I thank my family for their constant support and confidence in me to achieve the impossible. I have learned a lot from you all and I appreciate the similarities and differences we share. I reached this milestone because you all have been there for me, so this achievement is as much yours as it is mine. Please enjoy this achievement as much as I have! Thank you.

DEDICATION

To my mom,

Thank you for all the sacrifices you made and your unconditional love. You have always been my biggest role model and I hope I can inspire others as much as you inspire me.

To my grandparents,

Thank you abuelo, papa Luis, and mama Gela for raising me and all your wonderful memories. Your “orgullo puertorriqueño” made it and I wish you all could be here to celebrate. And to abuela, thank you for taking care of me all these years and always making me feel special.

Chapter 1. INTRODUCTION

1.1 HISTORY OF MIBG

Development of noninvasive imaging tools to detect and characterize irregularities in the adrenal gland have been the subject of intense research since the 1950s. The adrenal gland is comprised of two embryologically distinct tissues, the cortex and medulla (Dutt et al., 2021; Willenberg and Bornstein, 2000). The cortex arises from the mesoderm and is involved in steroidogenesis while the medulla is derived from the neuroectoderm and is involved in the regulation of catecholamines. Early imaging efforts exploited the physiological role of these tissues through the use of radio-iodinated cholesterols and radio-labeled catecholamines that were shown to accumulate in the adrenal system (Beierwaltes et al., 1978; Fowler et al., 1975). Since the adrenal medulla is like a specialized sympathetic ganglion, compounds with an affinity for adrenergic nerves would be expected to accumulate in the adrenal system. In the early 1960s, two antihypertensive drugs, guanethidine and bretylium, entered the US market and were found to be potent and selective adrenergic blocking agents. This led to the development of benzylguanidines as potential anti-adrenergic agents by combining the halogenated benzyl group of bretylium and the guanidine group in guanethidine (**Figure 1.1**) (Short and Darby, 1967).

In the late 1970s, Dr. Beierwaltes' group at the University of Michigan set out to develop a radiopharmaceutical that can image the adrenal medulla and its neoplasms (Wieland et al., 1980). This group radiolabeled the benzylguanidines with ^{131}I and investigated their accumulation in the adrenal glands and other tissues. They showed *para*-iodobenzylguanidine (pIBG) and *meta*-iodobenzylguanidine (mIBG) were highly concentrated in the adrenal glands of dogs for up to 192 hours. The concentrations in the other tissues (e.g. liver, kidney, heart, and

lung) decreased over time with minimal to no radiation after 48 hours. Although pIBG had greater accumulation in the adrenal glands, mIBG was shown to have less accumulation in the thyroid gland, less *in vivo* de-iodination, and was more metabolically stable (Wieland et al., 1984; Wieland et al., 1980). Therefore, mIBG was selected for further investigations as a diagnostic imaging tool for the adrenal medulla and related cancers.

Following its success in multiple imaging studies and shown to be safe following intravenous administration, ^{131}I-mIBG (Iobenguane) was approved by the US Food and Drug Administration (FDA) in 1994 to diagnose neuroendocrine cancers. However, there are limitations to the use of ^{131}I-mIBG as an imaging agent. The conventional gamma camera inefficiently captures the principal photon (364 keV) emitted by the radioactive decay of the ^{131}I isotope, leading to scatter and image noise (Liu et al., 2013). In addition, 90% of radioactive decay for the ^{131}I isotope is via β-emission and its decay half-life (8 days) does not contribute to favorable image formation. In contrast, the principal photon of the ^{123}I isotope (159 keV) is more suited for imaging with conventional gamma cameras and has a relatively shorter decay half-life (13 hours) than ^{131}I. The improved image resolution, better dosimetric profile, and single photon emission computed tomography (SPECT) capabilities led to FDA approval of ^{123}I-mIBG (AdreView) in 2008. Although ^{131}I-mIBG has been withdrawn as an imaging agent, the use of either isotopes for diagnostic studies depends on the availability and local preference (Sharp et al., 2016).

In addition to its adrenergic imaging capabilities, $^{123/131}$I-mIBG is successful in cardiac imaging and as a targeted radiotherapy. The high and distinguishable uptake in the heart made ^{123}I-mIBG viable as a cardiac imaging agent and was approved by the FDA in 2013 to image the sympathetic innervation of the myocardium. Due to its selective accumulation in neuroendocrine

tumor cells, mIBG was tested as a targeted radiotherapy to treat several neuroendocrine cancers (Parisi et al., 2016; Pryma et al., 2019). In this case, the β emission by ^{131}I is more favorable than ^{123}I as the strong radiation emission can penetrate surrounding cancer cells and result in DNA damage and cell death. High dose ^{131}I-mIBG (Azedra), approved by the FDA in 2018, proved efficacious in the treatment of advanced pheochromocytoma and paraganglioma. ^{131}I-mIBG is currently also under investigation in multiple clinical trials for the treatment of neuroblastoma (Parisi et al., 2016; Pryma et al., 2019).

1.2 Clinical Applications of mIBG

1.2.1 mIBG use in neuroblastoma

Neuroblastoma is the most common extracranial solid tumor in children and accounts for over 15% of all pediatric cancer mortalities in the US (Maris et al., 2007). Most patients are diagnosed at infancy, with a median age at diagnosis of 19 months (Ward et al., 2014). Neuroblastoma is a malignancy of the sympaticoadrenal lineage of the neural crest cells and can arise anywhere in the sympathetic nervous system. Approximately 70% of primary tumors occur within the abdomen region, with at least half of the primary tumors arising in the adrenal gland. Unfortunately, approximately half of the patients are metastatic at diagnosis, most commonly to the bone and bone marrow, lymph nodes, and liver (DuBois et al., 1999).

Neuroblastoma is heterogenous in its clinical presentation and can spontaneously regress or progress as an aggressive metastatic cancer. Patients with neuroblastoma are stratified as low, intermediate, or high-risk based on age, tumor stage, and biological factors, and the classification affects prognosis and treatment strategies (Park et al., 2008). Low- and intermediate-risk patients undergo surgery and/or chemotherapy with survival rates greater than 90% (Irwin and Park, 2015). In contrast, high-risk neuroblastoma patients undergo a combination of surgery,

autologous transplantation, chemotherapy, and whole-body radiation with survival rates less than 40-50% (Matthay et al., 1999; Parisi et al., 2016).

^{123}I-mIBG is routinely used in the clinic to diagnose neuroblastoma by detecting primary tumors and to identify sites of metastasis (Matthay et al., 2010). In a cohort of 66 confirmed neuroblastoma cases, ^{123}I-mIBG scintigraphy had a sensitivity of 88% and specificity of 83% for diagnosing neuroblastoma (Vik et al., 2009). When combined with planar and SPECT imaging, the sensitivity rose to 91%. With the inclusion of histopathology information, the sensitivity and specificity rose to 93% and 92%, respectively (Vik et al., 2009). Of note, false positive interpretations in this cohort were due to atypical adrenal or normal tissue uptake. Another study had similar results, with false negative rates of approximately 8% in 196 patients with pathologically proven neuroblastoma (Biasotti et al., 2000). Patients with bone metastasis at diagnosis had increased false-negative rates up to 21% without additional diagnostic tests (Gordon et al., 1990). Nevertheless, ^{123}I-mIBG scintigraphy has proven to be an essential imaging agent for diagnosing and monitoring disease progression of neuroblastoma.

The use of ^{131}I-mIBG as a therapeutic agent began in the early 1980s and was predominantly focused on the treatment of relapsed or refractory neuroblastoma (Treuner et al., 1988). Subsequently, multiple strategies have been undertaken to improve the clinical outcomes of relapsed or refractory neuroblastoma. These strategies include: the use of ^{131}I-mIBG as a monotherapy, as a combination therapy with radiosensitizers, in conjunction with bone marrow transplantation, and as part of the induction therapy with concomitant chemotherapeutic regimens (DuBois et al., 2015; Johnson et al., 2011; Matthay et al., 1999; Yanik et al., 2015). These strategies have shown complete response rates similar to or better than the standard-of-care for high-risk neuroblastoma patients. Additionally, ^{131}I-mIBG is under investigation as a

front-line treatment for neuroblastoma patients and has shown a response rate of up to 73%, higher than the typical response for high-risk patients (de Kraker et al., 2008).

Toxicity is a major concern for ^{131}I-mIBG therapy. Toxicities are associated with the radioactive ^{131}I whereas non-radiolabeled mIBG is non-toxic. Hematological toxicities are the most common and severe toxicities but patients are rescued by autologous stem cell infusion (Bleeker et al., 2013). Thyroid uptake of $^{123/131}$I-mIBG is usually blocked by co-administration with potassium iodine or Lugol's solution to saturate the sodium-iodine symporter (Matthay et al., 2007; Parisi et al., 2016). However, radiation to the thyroid is still observed in patients and can lead to hypothyroidism months after treatment (Van Santen et al., 2002). Transient cardiac toxicities can occur during ^{131}I-mIBG infusion and require continuous and automated blood pressure monitoring (Parisi et al., 2016). Tachycardia and hypertension are the most common cardiac toxicities in neuroblastoma patients and occurs in approximately 10% of neuroblastoma patients receiving ^{131}I-mIBG therapy (Shusterman et al., 2011). Other significant toxicities include gastro-intestinal disturbances (nausea, vomiting), sialadenitis (swelling of the salivary glands), and hepatic-related toxicities (Bleeker et al., 2013; Parisi et al., 2016). When ^{131}I-mIBG is used in combination with other anticancer drugs, improvements to the response rates can be variable and the ^{131}I-mIBG associated toxicities can be exacerbated (Matthay et al., 2006).

1.2.2 mIBG use in pheochromocytoma and paraganglioma

In addition to neuroblastoma, ^{123}I-mIBG has been successfully used in the localization and evaluation of various neuroendocrine cancers, in particular pheochromocytoma and paraganglioma. Unlike neuroblastoma, sporadic forms of pheochromocytoma and paraganglioma are usually diagnosed in individuals aged 40-50 years and are rare in children (Neumann et al., 1993). Pheochromocytoma and paraganglioma arise from the chromaffin cells that produce

catecholamines in the adrenal medulla or accessory adrenal tissue (Lenders et al., 2005). The two tumor types cannot be differentiated based on histology alone, hence anatomical location of the tumors is used to distinguish between them (Lam, 2017). Based on the 2017 World Health Organization (WHO) classification, pheochromocytoma is an adrenal tumor while paraganglioma is an extra-adrenal tumor. Approximately 80% of pheochromocytoma patients present with primary tumors in the adrenal medulla and frequently produce excessive levels of catecholamines (Eisenhofer et al., 2003). The rest of primary tumors are typically localized in the paravertebral sympathetic ganglia of the abdomen region and typically do not present with hypersecretion of catecholamines. Pheochromocytoma and paraganglioma are both rare cancers with a prevalence of 0.3% in patients with hypertension (Anderson et al., 1994). However, fatal complications preceded diagnosis in a significant proportion of patients with pheochromocytoma as evidenced in over 8000 autopsies, indicating that the cancer is often undetected and left untreated (Lo et al., 2000).

^{123}I-mIBG scintigraphic imaging has been proved to successfully help diagnose pheochromocytoma. ^{123}I-mIBG SPECT imaging has a reported sensitivity of 83-100% and a specificity of 95-100% for detecting pheochromocytomas (Nielsen et al., 1996). However, ^{123}I-mIBG has a lower sensitivity (56-75%) for detecting the extra-adrenal paragangliomas and in patients with genetic mutations of succinate dehydrogenase, an enzyme involved in the Krebs cycle and associated with metastasis (Wiseman et al., 2009). Nonetheless, patients that exhibit positive ^{123}I-mIBG scintigraphy may benefit from ^{131}I-mIBG radiotherapy (Rao et al., 2019).

The goals for ^{131}I-mIBG as treatment for pheochromocytoma are focused on alleviating symptoms, lowering blood pressure, reducing catecholamine secretion, and ultimately shrink tumors with minimal systemic toxicity (Beierwaltes, 1987). The early non-controlled clinical

trials with ^{131}I-mIBG for treating pheochromocytoma showed a failure to achieve complete remission in most patients, but produced an improvement in sustained remission or stable disease for up to 2 years (Loh et al., 1997). More recent studies have used ^{131}I-mIBG therapy in patients with predominantly non-resectable and malignant pheochromocytoma and paraganglioma (Kotecka-Blicharz et al., 2018; Pryma et al., 2019; Wakabayashi et al., 2019). These studies showed high rates of stable disease in patients treated with ^{131}I-mIBG therapy and a significant reduction in the use of hypertension medication. In addition, ^{131}I-mIBG therapy to reduce tumor size prior to surgery in a case study of two patients highlighted the potential of ^{131}I-mIBG as an adjunctive therapy with surgery for pheochromocytoma (Dhingra and Halkar, 2020). The toxicities in pheochromocytoma patients given ^{131}I-mIBG were similar to those in neuroblastoma patients, with hematological toxicities being the most common and reported hypothyroidism, hypertension, dry mouth, and gastro-intestinal disturbances.

1.2.3 123I-mIBG as a myocardial scan

The heart is innervated by sympathetic and parasympathetic nerve fibers. The sympathetic nerves follow along the coronary arteries in the subepicardium before penetrating the myocardium (Wan and Travin, 2020). Epinephrine and norepinephrine are the two main catecholamines that can activate or deactivate sympathetic receptors within the cardiovascular system. Stimulation of the sympathetic nervous system by norepinephrine can increase heart rate, cardiac contractility, and can be affected by exercise and pathological conditions (Gordan et al., 2015). In view of the clinical importance and frequency of myocardial lesions, a technique that can visualize myocardial lesions in patients was needed.

Early development of radiotracers for heart imaging were performed in dogs with free radionuclides and radio-iodinated bretylium analogs (Carr et al., 1964; Counsell et al., 1974).

With the development of radio-iodinated mIBG as an adrenomedullary imaging agent, Dr. Beierwaltes' group tested whether mIBG could be a successful imaging agent for the cardiac sympathetic innervation (Raffel and Wieland, 2010; Wieland et al., 1980). The researchers showed that mIBG accumulated in the hearts of rats, dogs, and monkeys with heart-to-blood ratios 2- to 3-fold higher than ^{201}Tl, a commonly used heart radiotracer (Wieland et al., 1981). Shortly thereafter, a clinical study in healthy volunteers demonstrated that ^{123}I-mIBG could be used as a myocardial imaging agent (Kline et al., 1981).

As a norepinephrine analog, ^{123}I-mIBG can visualize alterations in the sympathetic nerve function (**Figure 1.1**). The common semi-quantitative indices for interpretation of cardiac sympathetic nerve images are the heart-to-mediastinum ratio (H/M) and the washout rate (WR) that represent the myocardial norepinephrine content and the presynaptic norepinephrine kinetics at the myocardial sympathetic nerve endings, respectively (Kasama et al., 2016). ^{123}I-mIBG has been used extensively in patients with heart failure, a disease with poor prognosis that affects about 2% of the adult population worldwide (Metra and Teerlink, 2017). The increased sympathetic activation in heart failure leads to reduced norepinephrine reuptake that contributes to the low mIBG concentration in neurons (reduced (H/M) while the increased norepinephrine secretion causes greater mIBG washout (higher WR) (Teresińska, 2012). A decrease in H/M or increase in WR are strongly correlated with poor prognosis in heart failure patients and predict an increased risk of arrhythmia and sudden cardiac death (Merlet et al., 1992; Verberne et al., 2009). ^{123}I-mIBG has been widely investigated for detection of coronary artery disease and cardiomyopathies, for cardiac devices for lethal arrhythmia, diagnosis of neurodegenerative diseases, and decision-making for heart medication (Nakajima et al., 2018).

1.3 PHARMACOKINETICS AND MECHANISM OF TRANSPORT OF MIBG

The broad clinical applications of radio-iodinated mIBG are due to its favorable pharmacokinetic and its similarities to the mechanism of transport of norepinephrine in neurons and neuroendocrine cells. mIBG is administered as an intravenous infusion over 1-2 minutes for ^{123}I-mIBG diagnostic imaging and 60-120 minutes for ^{131}I-mIBG radiotherapy (Parisi et al., 2016). The blood concentrations of mIBG rapidly decrease in a biphasic manner with a half-life of the initial phase of approximately 0.2-0.3 hours and a long terminal half-life greater than 38 hours (**Table 1.1**). The amount of mIBG in the blood after 5 minutes corresponds to about 10% of the dose. mIBG has a large volume of distribution of 3-5 L/kg, indicating a substantial distribution into tissues. After 1 hour, 2-4% of the dose remains within the vascular compartment. mIBG is rapidly eliminated by the kidney (Chin et al., 2014; Lashford et al., 1988).

The majority of the administered dose is rapidly excreted into the urine unchanged with 50% of the dose excreted into the urine within 24 hours (**Table 1.1**) (Blake et al., 1989; Lashford et al., 1988; Parisi et al., 2016). Besides glomerular filtration, mIBG likely undergoes active secretion in the kidney (Ehninger et al., 1987). The renal clearance of mIBG was 2.5- to 3-fold greater than the unbound glomerular filtration rate (GFR) in neuroblastoma patients (Blake et al., 1989). Similarly, metformin (contains guanidine group) and bretylium (contains halogenated benzyl group) exhibit renal clearance greater than their GFR, indicating significant contribution of active secretion for these chemical moieties (Anderson et al., 1980; Gong et al., 2012). Other elimination pathways have minimal impact on the systemic elimination of mIBG (**Figure 1.2**). Fecal excretion accounts for less than 1% of the total mIBG dose while dissociation of the ^{123}I/^{131}I from mIBG accounts for less than 5% of the total dose. Metabolism of mIBG accounts

for less than 10% of the dose with the major metabolite being meta-iodohippuric acid (Chin et al., 2014; Coleman et al., 2009; Mangner et al., 1986).

The transport of mIBG in neurons and neuroendocrine cancer cells is similar to that of norepinephrine. The majority of mIBG is actively transported by the sodium-dependent norepinephrine transporter (NET) in neurons and neuroendocrine cancer cells (Streby et al., 2015). A non-saturable, passive transport pathway has been suggested for mIBG, however active transport is over 50-fold more efficient than passive transport at low mIBG concentrations. Similar to norepinephrine, inversion of the sodium gradient across the cell membrane or by trans-stimulation by norepinephrine may cause mIBG to be released out of the neuron and subsequently, mIBG may undergo re-uptake by NET (Streby et al., 2015). Once mIBG enters the cancer cells, mIBG remains in the cytoplasm and can accumulate in the storage vesicles and mitochondria. mIBG is actively transported by the vesicular monoamine transporters (VMATs) into storage vesicles (Kölby et al., 2003). The mechanism of transport into the mitochondria is currently unknown. In contrast to normal physiological neuroendocrine tissues, neuroblastoma cancer cells tend to have fewer storage vesicles, hence only 7% of mIBG is stored in vesicles while 93% is found in the cytoplasm and mitochondria (Lashford et al., 1991). The efflux out of the cancer cells is thought to be through carrier-mediated efflux and passive diffusion. The reverse transport of mIBG by NET has been suggested as an active efflux pathway, but a recent uptake study suggested that multidrug resistance protein 1 and 4 (MRP1/4; *ABCC1/4*) can transport mIBG and may contribute to the active efflux of mIBG in neuroendocrine cancer cells (Kobayashi et al., 2020). Unlike norepinephrine, metabolism does not contribute to the elimination of mIBG in the neuroendocrine cells as mIBG is not a substrate of monoamine oxidase (MAO) or catechol-O-methyltransferase (COMT) (Graefe et al., 1999).

The mechanism of transport in the heart is thought to be similar to that of the neuroendocrine cancer cells. Once in the systemic circulation, mIBG diffuses out of cardiac blood vessels and enters the interstitium. NET rapidly transports mIBG into the neurons where mIBG is stored in the norepinephrine storage vesicles. Non-neuronal uptake of mIBG can contribute to cardiac accumulation but is thought to play a lesser role relative to neuronal uptake in humans (Dae et al., 1992; Sisson et al., 1987).

Aside from the heart, mIBG exhibits extensive physiological distribution into healthy tissues. Based on whole-body scintigraphy scans, mIBG distributes and accumulates in the salivary glands, liver, intestines, thyroid, lungs, spleen, muscle, urinary bladder, and adrenal glands (Chin et al., 2014; Coleman et al., 2009; Nakajo et al., 1983). In particular, the salivary glands, a highly sympathetically innervated tissue, exhibits the highest radiation exposure of mIBG and can consistently be visualized in scintigraphic images. The tissue distribution and accumulation are similar between ^{123}I-mIBG and ^{131}I-mIBG (Nakajo et al., 1983; Parisi et al., 1992). NET is predominantly expressed in neurons but is also expressed in the lung and may contribute to the accumulation of mIBG in the lungs (Torres et al., 2003). However, the mechanisms of transport in other tissues are not well understood (**Table 1.2**). Uptake studies in cells expressing dopamine transporter (DAT) or serotonin transporter (SERT) showed that neither DAT nor SERT transport mIBG (Glowniak et al., 1993). However, recent evidence supports that mIBG is a substrate of human SERT and contributes to the platelet accumulation of mIBG, leading to the common hematological toxicities in ^{131}I-mIBG therapy (Blom et al., 2020).

Mechanisms of transport of mIBG into the various tissues have not been elucidated. The high accumulation of radioactive mIBG in the normal tissues presents several challenges for ^{123}I-mIBG imaging and ^{131}I-mIBG radiotherapy for neuroendocrine cancers. First, uptake into normal

tissues may interfere with ^{123}I-mIBG tumor imaging, leading to increased rate of false negatives for diagnosing neuroendocrine cancers (Eisenhofer et al., 2003; Parisi et al., 2016; Vik et al., 2009). Additionally, the H/M ratio used for ^{123}I-mIBG myocardial scan can be affected by liver and lung accumulation that causes image scattering (Verschure et al., 2015). Furthermore, uptake of ^{131}I-mIBG into normal tissues can compete with tumor uptake, leading to reduced antitumor efficacy. Lastly, the high uptake and accumulation in normal tissues are associated with common and often severe radiation-induced toxicities (Bleeker et al., 2013). Therefore, an understanding of how mIBG is transported in normal tissues is essential for developing strategies to enhance mIBG efficacy and minimize toxicity.

1.4 POLYSPECIFIC ORGANIC CATION TRANSPORTERS AND THEIR ROLE IN MIBG PHARMACOKINETICS AND TISSUE DISTRIBUTION

The polyspecific organic cation transporters are a group of soluble carrier transporters that mediate the cellular uptake and efflux of various organic cations. This group consists of the organic cation transporter 1-3 (OCT1-3; *SLC22A1-3*), the plasma membrane monoamine transporter (PMAT; *SLC29A4*), and the multidrug and toxin extrusion protein 1 and 2-K (MATE1/2-K; *SLC47A1/2*). The transport by the OCTs is electrogenic, sodium-independent and bi-directional (**Table 1.2**) (Koepsell, 2004). In general, the expression of the OCTs overlaps with tissues that exhibit extensive uptake and accumulation of mIBG. OCT1 is predominantly expressed on the sinusoidal membrane of hepatocytes in the liver (Giacomini et al., 2010). OCT1 has been detected at lower expression levels in multiple tissues, such as the adrenal gland, small intestine, lung, kidney, and skeletal muscle (Gorboulev et al., 1997; Koepsell, 2004; Wagner et al., 2016). A previous study done in *Oct1*$^{-/-}$ mice observed around a 75% decrease in liver

concentrations of mIBG 30 min after intravenous injection, suggesting that OCT1 may contribute to the hepatic accumulation of mIBG (Jonker et al., 2001).

OCT2 is predominantly expressed in the kidney with low expression in other tissues (**Table 1.2**) (Koepsell, 2004; Wagner et al., 2016). Many cationic xenobiotics undergo active secretion across the renal proximal tubule cells through the OCT2 and MATE1/2-K pathway (Giacomini et al., 2010). For mIBG, the high renal clearance relative to its filtration clearance (Blake et al., 1989) suggests that mIBG undergoes renal secretion and may be subject to active elimination by OCT2/MATEs in the proximal tubule cells. Currently, it is not known whether mIBG can be actively secreted by the renal OCT2/MATEs pathway.

Lastly, OCT3 exhibits varied expression in multiple tissues, such as the salivary glands, heart, skeletal and smooth muscle, lung, intestine, kidney, and adrenal glands (**Table 1.2**) (Koepsell, 2004; Lee et al., 2014; Wagner et al., 2016). OCT3 is the major polyspecific organic cation transporter expressed in both mouse and human acinar cells, the epithelial cells involved in saliva production and secretion into the ductal cells (Lee et al., 2014). OCT3 is localized on both the apical and basolateral membrane of the acinar cells lining the salivary glands, suggesting that OCT3 is involved in both uptake into the salivary glands and secretion into saliva of organic cations. OCT3 expression in the heart is localized to vascular endothelial cells and myocardiocytes (Grube et al., 2011; Solbach et al., 2011). Deletion of Oct3 in mice caused a decrease in heart concentrations of metformin and MPP+, a classical substrate of OCTs (Lee et al., 2014; Zwart et al., 2001). Strategies to block OCT3 uptake and decrease normal physiological distribution of mIBG have been attempted with corticosteroids but the small change in tissue uptake and non-selective inhibitory nature of corticosteroid make it difficult to specifically interpret the impact of OCT3 on mIBG disposition *in vivo* (Bayer et al., 2016).

Once organic cations are transported into hepatocytes or proximal tubule cells, they undergo excretion into the bile or urine by MATE1 and/or MATE2-K (Giacomini et al., 2010). Transport by the MATEs is through an electroneutral exchange between a H^+ and a cationic substrate (Otsuka et al., 2005). Both MATE1 and MATE2-K are highly expressed in the apical membrane of the proximal tubule cells in the kidney (**Table 1.2**). MATE1 has also been shown to be expressed in the liver, heart, skeletal muscle, and adrenal gland. In mouse hearts, Mate1 was localized to the endothelial cells (Hiasa et al., 2006). However, the functionality of MATE1 in the heart is not understood as the MATEs require a pH gradient to be active (Otsuka et al., 2005).

In addition to OCTs and MATEs, another polyspecific organic cation transporter, PMAT, was first cloned and characterized by our laboratory (Engel et al., 2004). The transport of small organic cations by PMAT is electrogenic and pH sensitive (Duan and Wang, 2010; Zhou et al., 2010). PMAT is highly expressed in the brain and also has varied expression in the kidney, small intestine, and the heart (Dahlin et al., 2007; Duan and Wang, 2013; Xia et al., 2007; Zhou et al., 2007). In addition, unpublished data from our laboratory showed that PMAT is highly expressed in neuroblastoma cells. However, the role of this transporter in mIBG uptake in tumor cells is not understood and is currently under investigation.

To improve mIBG efficacy, the major goal is to increase mIBG tumor-to-organ distribution ratios with higher targeted tumor uptake and decreased non-tumor tissue exposure. Thus, understanding the molecular mechanisms mediating mIBG transport in tumor and normal tissues is critical for developing strategies to block non-cancerous tissue distribution of mIBG. Since OCTs and MATEs are not expressed in neuroendocrine cancer cells, targeting these pathways may lead to improved efficacy and reduced toxicities in ^{131}I-mIBG therapy (Dubois et

al., 2012). Previous work has implicated organic cation transporters as potential transporters of mIBG (Bayer et al., 2009; Ito et al., 2012). However, the uptake kinetics of mIBG have not been determined nor compared to NET-mediated uptake (Ito et al., 2012). Furthermore, the OCT2/MATE pathway has not been characterized as a mechanism for renal secretion of mIBG. Lastly, the specific and quantitative contribution of OCT3 to mIBG tissue uptake and distribution in normal physiological tissues *in vivo* is unclear.

1.5 Hypothesis and Specific Aims

The overall goal of my research project is to improve our understanding of the role of polyspecific organic cation transporters in the disposition, interaction, and tissue-specific toxicities of mIBG. We hypothesize that polyspecific organic cation transporters are major determinants for mIBG disposition in normal tissues and its elimination from the body, and thus can be targeted to improve mIBG therapy. The specific aims of my thesis are:

Specific Aim 1: a) Determine the kinetics and interactions of mIBG transport by the polyspecific organic cation transporters; b) Elucidate the involvement of OCT2/MATEs in the renal elimination of mIBG.

In this Aim, I will systematically determine the detailed interactions, including substrate status, transport kinetics, and inhibitor interaction, of mIBG with human OCT1–3 and MATE1/2-K in comparison with the classic mIBG transporter NET using HEK293 cell lines stably expressing these transporters. I will also use an *in vitro* cell culture model (hOCT2/hMATE1 double-transfected MDCK cells) to investigate the OCT2/MATE pathway as the molecular mechanism for renal secretion of mIBG. Together, my study will validate the major transporters involved in tissue-specific uptake and systemic elimination of mIBG. Results

obtained from studies under Aim 1 will help to predict and prevent adverse drug interaction with therapeutic ^{131}I-mIBG and develop clinical strategies to reduce ^{131}I-mIBG accumulation and toxicity in normal tissues and organs.

Specific Aim 2: Develop a quantification method to measure non-radiolabeled mIBG in biological matrices.

In this Aim, I will develop a LC-MS/MS quantification method to measure non-radiolabeled mIBG concentrations in mouse plasma and tissues. The validation of this method will be conducting according to the recommendations by the Food and Drug Administration guidance of bioanalytical methods for small molecules (Food and Drug Administration, 2018). I will validate the reproducibility of this extraction method based on the specificity, selectivity, precision, accuracy, recovery, and matrix effect in the plasma and liver homogenates. The validated method from this aim will allow for a reproducible and rapid analysis of non-radiolabeled mIBG concentrations to support studies in preclinical species.

Specific Aim 3: Determine the impact of OCT3 on the pharmacokinetics and tissue distribution of mIBG.

In this Aim, I will determine the substrate status and transport kinetics of mIBG using HEK293 cells stably expressing the mouse ortholog of Oct3. I will conduct a comprehensive pharmacokinetic and biodistribution study in wild-type and Oct3 knockout mice and construct full concentration-time profiles in plasma and multiple tissues. The plasma pharmacokinetic parameters and the tissue exposures determined from the concentration-time profiles will be compared between the wild-type and Oct3 knockout mice. This study will determine the impact

OCT3 has on the pharmacokinetics and the distribution of mIBG into several tissues. The results obtained from Aim 3 will help support the use of OCT3 inhibitors as a viable clinical strategy to reduce ^{131}I-mIBG accumulation and toxicity healthy tissues. In addition, these results will help in understanding and interpreting results of cardiac ^{123}I-mIBG scintigraphic images.

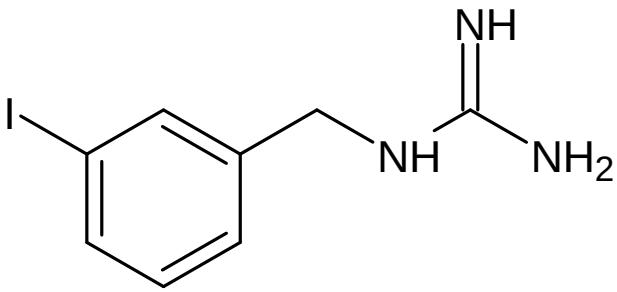

meta-iodobenzylguanidine (mIBG)

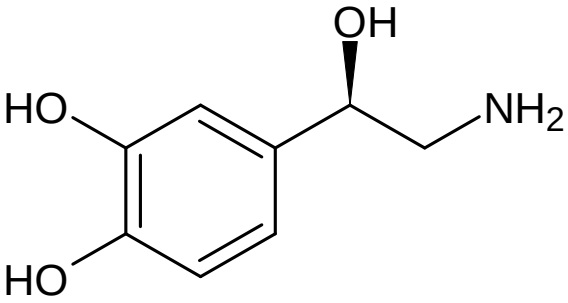

Norepinephrine

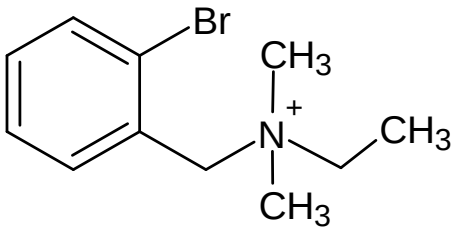

Bretylium

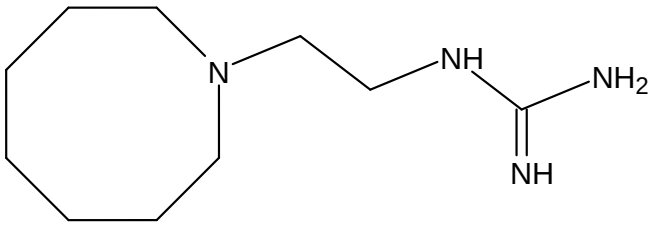

Guanethidine

Figure 1.1. Chemical Structures of mIBG, norepinephrine, bretylium, and guanethidine.

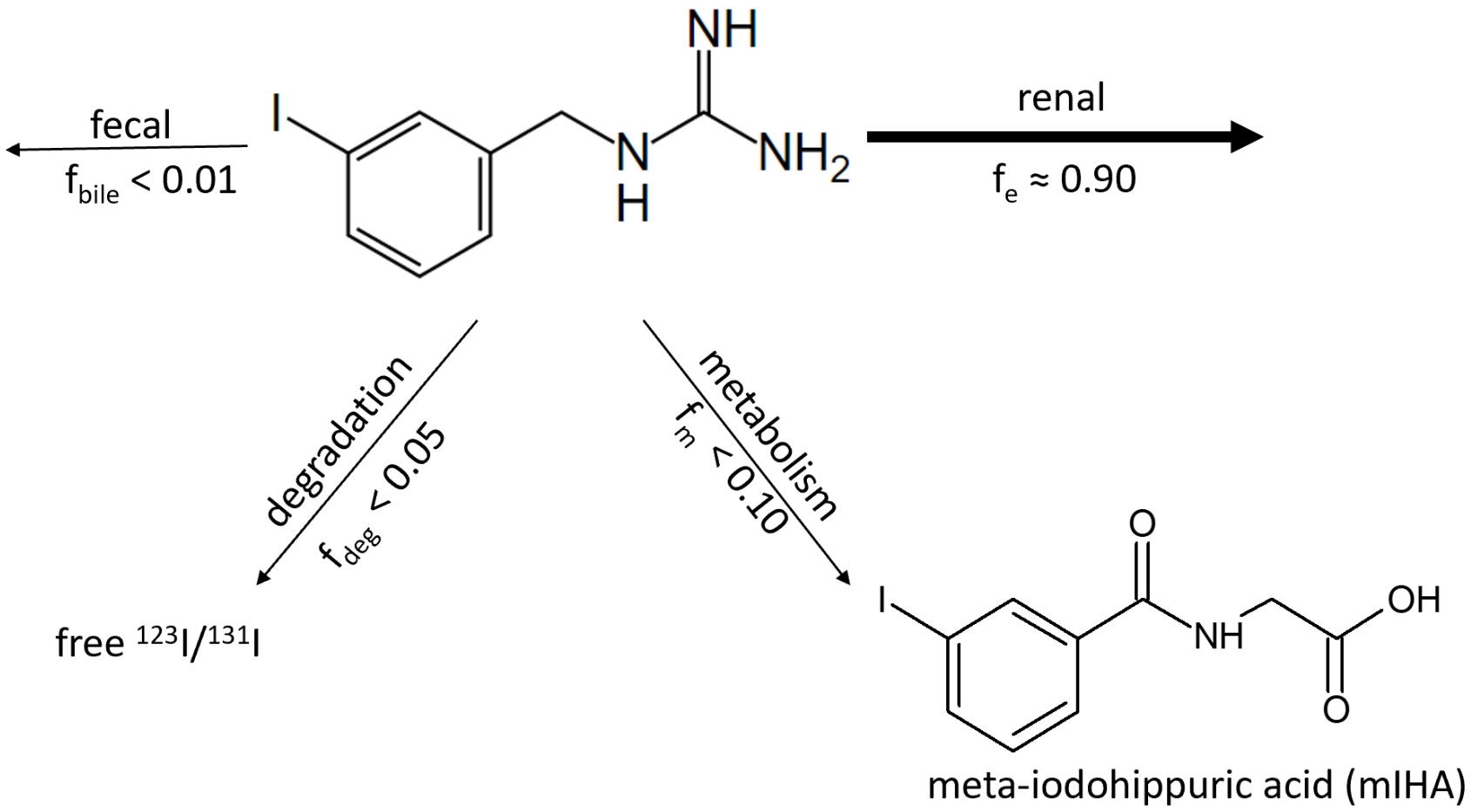

Figure 1.2. Elimination pathway of mIBG in humans.

Table 1.1. Pharmacokinetic parameters of mIBG in humans.

Parameter	High specific activity ^{123}I-mIBG[a]	High specific activity ^{131}I-mIBG[b]
C_{max} (μCi/mL)	N.D.	0.06 ± 0.02
CL (mL/hr/kg)	58.1 ± 50.2	62 ± 24
V_{ss} (L/kg)	4.85 ± 1.18	2.96 ± 0.15
$t_{1/2, \alpha}$ (hr)	0.22 ± 0.09	0.3 ± 0.03
$t_{1/2, \beta}$ (hr)	78.7 ± 33.3	38.3 ± 3.4
$f_{e, 24\ hrs}$ (%)	53.7 ± 9.46	49.8 ± 3.1
$f_{e, 120\ hrs}$ (%)	N.D.	80.3 ± 2.8
f_u (%)	N.D.	37 - 39

N.D. = Not determined
[a]Parameters obtained from (Chin et al., 2014)
[b]Parameters obtained from Azedra FDA label and (Coleman et al., 2009)

Table 1.2. Molecular characteristics of the monoamine and polyspecific organic cation transporters.

Transporters	Gene	Transport Mode	Tissue Distribution	References
NET	*SLC6A2*	Co-transport with Na^+ and Cl^-	Central and peripheral noradrenergic neurons, adrenal medulla (chromaffin cells), lung, placenta	(Eisenhofer, 2001; Giros et al., 1991; Gu et al., 1994; Hoffman et al., 1998; Kimelberg and Katz, 1985; Pacholczyk et al., 1991; Ramamoorthy et al., 1993; Schroeter et al., 1997; Talvenheimo and Rudnick, 1980; Torres et al., 2003; Wade et al., 1996)
DAT	*SLC6A3*	Co-transport with 2 Na^+ and Cl^-	Dopaminergic neurons, stomach, pancreas, kidney	
SERT	*SLC6A4*	Co-transport with Na^+ and Cl^-	Serotoninergic neurons, platelets, GI tract, adrenal gland, astrocytes	
VMAT1	*SLC27A1*	$2H^+$/monoamine exchange	Adrenal medulla (chromaffin cells), endocrine/paracrine cells associated with GI tract and sympathetic nervous system	(Höltje et al., 2003; Peter et al., 1995; Weihe et al., 1994; Wimalasena, 2011)
VMAT2	*SLC27A2*	$2H^+$/monoamine exchange	Adrenal medulla (chromaffin cells), neuronal cells in the central and peripheral nervous system, platelets	
OCT1	*SLC22A1*	Electrogenic	Liver, small intestine, kidney, lung, brain, heart, skeletal muscle, placenta, mammary gland, adrenal gland, immune cells, adipose tissue	(Gorboulev et al., 1997; Gründemann et al., 1998; Koehler et al., 1997; Koepsell, 2004; Lee et al., 2014; Wagner et al., 2016; Zhang et al., 1997)
OCT2	*SLC22A2*	Electrogenic	Kidney, brain, lung, small intestine, thymus, placenta	
OCT3	*SLC22A3*	Electrogenic	Salivary gland, heart, brain, lung, adrenal lung, skeletal and smooth muscle, adrenal gland, liver, kidney, placenta, small intestine, cornea	
PMAT	*SLC29A4*	Electrogenic pH sensitive	Brain, choroid plexus, skeletal muscle, kidney, heart, liver, small intestine, endometrium	(Dahlin et al., 2007; Duan and Wang, 2010; Duan and Wang, 2013; Engel and Wang, 2005; Engel et al., 2004; Xia et al., 2007; Zhou et al., 2007)
MATE1	*SLC47A1*	Electroneutral (H^+/OC^+ exchange)	Liver, kidney, heart, skeletal muscle, adrenal gland	(Hiasa et al., 2006; Masuda et al., 2006; Otsuka et al., 2005; Wagner et al., 2016)
MATE2/2-K	*SLC47A2*	Electroneutral (H^+/OC^+ exchange)	Kidney	

Chapter 2. CHARACTERIZATION OF MIBG TRANSPORT BY THE POLYSPECIFIC ORGANIC CATION TRANSPORTERS – IMPLICATION FOR MIBG THERAPY

This chapter was published in:

López Quiñones, A. J., Wagner, D. J., Wang, J. "Characterization of *meta*-Iodobenzylguanidine (mIBG) Transport by Polyspecific Organic Cation Transporters - Implication for mIBG Therapy." *Molecular Pharmacology*, 98 (2): 109-119 (2020).

2.1 ABSTRACT

Radiolabeled *meta*-iodobenzylguanidine (mIBG) is an important radiopharmaceutical used in the diagnosis and treatment of neuroendocrine cancers. mIBG is known to enter tumor cells through the norepinephrine transporter. Whole-body scintigraphy has shown rapid mIBG elimination through the kidney and high accumulation in several normal tissues, but the underlying molecular mechanisms are unclear. Using transporter-expressing cell lines, we show that mIBG is an excellent substrate for human organic cation transporters 1-3 (hOCT1-3) and the multidrug and toxin extrusion proteins 1 and 2-K (hMATE1/2-K), but not for the renal organic anion transporter 1 and 3 (hOAT1/3). Kinetic analysis revealed that hOCT1, hOCT2, hOCT3, hMATE1, and hMATE2-K transport mIBG with similar apparent affinities (K_m of 19.5 ± 6.9, 17.2 ± 2.8, 14.5 ± 7.1, 17.7 ± 10.9, 12.6 ± 5.6 μM, respectively). Transwell studies in hOCT2/hMATE1 double-transfected MDCK cells showed that mIBG transport in the basal (B)-to-apical (A) direction is much greater than in the A-to-B direction. Compared to control cells, the B-to-A permeability of mIBG increased by 20-fold in hOCT2/hMATE1 double-transfected cells. Screening of 23 drugs used in the treatment of neuroblastoma identified several drugs with the potential to inhibit hOCT- or hMATE-mediated mIBG uptake. Interestingly, irinotecan selectively inhibited hOCT1 whereas crizotinib potently inhibited hOCT3-mediated mIBG uptake. Our results suggest that mIBG undergoes renal tubular secretion mediated by hOCT2 and hMATE1/2-K; and hOCT1 and hOCT3 may play important roles in mIBG uptake into normal tissues.

2.2 INTRODUCTION

Neuroblastoma is a neuroendocrine cancer derived from the neural crest cells of the sympathetic nervous system. It is the most common extracranial solid tumor in children and accounts for over 15% of all pediatric cancer mortalities in the US (Maris et al., 2007). Prognosis and treatment strategies for neuroblastoma is stratified to low, intermediate, or high-risk based on age, tumor stage, and biological factors (Park et al., 2008). Although low- and intermediate-risk patients often have great treatment outcomes, many high-risk neuroblastoma patients are metastatic at time of diagnosis and undergo aggressive multimodal therapy with overall survival rates still less than 50% (Matthay et al., 1999; Parisi et al., 2016). Therefore, there is an urgent need for new therapeutic agents and strategies for high-risk neuroblastoma patients.

Radioiodine-labeled *meta*-iodobenzylguanidine (mIBG) is a targeted radiopharmaceutical used in both the diagnosis and treatment of neuroendocrine cancers (e.g. neuroblastoma, pheochromocytoma, and paraganglioma). Originally developed as a structural analog of norepinephrine for adrenal cortex imaging, mIBG is taken up into tumor cells by the norepinephrine transporter (NET, *SLC6A2*) which is highly expressed in neuroendocrine tumors (Streby et al., 2015). ^{123}I-labeled mIBG (iobenguane I-123 or AdreView) was approved by United States Food and Drug administration (FDA) in 2008 for gamma detection of primary or metastatic neuroblastoma and pheochromocytoma. When mIBG is labeled with iodine-131, the β emission penetrates tumor cells, resulting in DNA damage and cell death. In 2018, ^{131}I-mIBG (iobenguane I-131 or Azedra) was FDA approved for treatment of advanced or metastatic pheochromocytoma and paraganglioma in adults. Currently, ^{131}I-mIBG is under clinical

investigation as a frontline therapy for high-risk neuroblastoma either as monotherapy or in combination with other agents with improved clinical response (Parisi et al., 2016).

Clinically, mIBG is given to patients by intravenous infusion. The drug does not undergo hepatic metabolism, and majority of the administered dose is rapidly excreted into the urine unchanged (Blake et al., 1989; Parisi et al., 2016). Besides glomerular filtration, clinical evidence suggests that mIBG may also undergo active secretion in the kidney (Ehninger et al., 1987). Whole-body scintigraphy scans show that besides NET-mediated uptake into tumor lesions, mIBG also has extensive uptake and accumulation in several normal tissues, including the liver, salivary glands, heart, intestines, and adrenal glands (Chin et al., 2014; Coleman et al., 2009). The high accumulation of radioactive mIBG in the normal tissues presents several challenges. First, uptake into normal tissues may interfere with ^{123}I-mIBG tumor imaging, leading to increased rate of false negatives (Parisi et al., 2016). Alternatively, uptake of ^{131}I-mIBG into normal tissues can compete with tumor uptake, leading to reduced antitumor efficacy. Lastly, the high uptake and accumulation of mIBG in normal tissues is associated with several radiation-induced toxicities (Bleeker et al., 2013). Therefore, an understanding how mIBG is transported in normal tissues is essential for developing strategies to enhance mIBG efficacy while minimizing toxicity.

The organic cation transporters (OCT) are a group of solute carrier transporters expressed in various tissues and mediate cellular transport of a wide array of endogenous and exogenous organic cations (Giacomini et al., 2010; Wagner et al., 2016). This group includes the membrane potential driven OCT1 (*SLC22A1*), OCT2 (*SLC22A2*), and OCT3 (*SLC22A3*) and the electroneutral multidrug and toxin extrusion proteins 1 (MATE1, *SLC47A1*) and 2-K (MATE2-K, *SLC47A2*). In humans, OCT1 is the major isoform expressed in the liver and mediates

organic cation uptake into the hepatocytes. In the kidney, OCT2 and MATE1/2-K are expressed at the basolateral and apical membranes, respectively, of renal proximal tubule cells and work cooperatively to mediate tubular secretion of organic cations (Giacomini et al., 2010; Wagner et al., 2016). OCT3 is broadly expressed in many tissues including salivary glands, heart, and placenta, and we previously demonstrated an important role of OCT3 in drug uptake and transport in these tissues (Lee et al., 2014; Lee et al., 2018; Wagner et al., 2018).

Previous data have implicated OCTs and MATEs in the transport of mIBG (Bayer et al., 2009; Ito et al., 2012). However, the transport kinetics of mIBG have not been determined for these transporters. It is not known whether mIBG can be actively secreted by the renal OCT2/MATEs pathway. In this study, we characterized the detailed interactions of mIBG with hOCT1-3 and hMATE1/2-K in comparison to the classic mIBG transporter NET. The possibility of hOCT2/hMATE-mediated renal secretion of mIBG was investigated using an in vitro model of renal transepithelial transport. Lastly, the potential for an interaction with other FDA-approved oncology drugs on the transport of mIBG by OCTs and MATEs was evaluated.

2.3 METHODS

2.3.1 Materials.

Meta-iodobenzylguanidine, glyburide, and pyrimethamine were purchased from Sigma Aldrich (St. Louis, MO). [^{3}H]methyl-4-phenylpyridinium (MPP+, 80 Ci/mmol), [^{14}C]*para*-aminohippuric acid (PAH, 55 mCi/mmol), [^{3}H]estrone sulfate (ES, 50 Ci/mmol), and [^{3}H]mannitol (20 Ci/mmol) were purchased from American Radiolabeled Chemicals, Inc. (St. Louis, MO). [^{14}C]metformin (112 mCi/mmol) was purchased from Moravek Biochemicals, Inc. (Brea, CA). Optima grade of acetonitrile and formic acid were obtained from Thermo Fisher (Rockford, IL). Cell culture media and reagents were purchased from Invitrogen (Carlsbad, CA).

The Pierce bicinchoninic acid (BCA) protein assay kit was obtained from Thermo Fisher (Rockford, IL).

2.3.2 Cell Culture.

Flp-In human embryonic kidney (HEK) 293 cells stably transfected with human OCT1 (hOCT1), hOCT2, hOCT3, human organic anion transporter 1 (hOAT1, *SLC22A6*), hOAT3 (*SLC22A8*), hMATE1 and hMATE2-K and the empty pcDNA5/FRT vector (control) were previously generated in our laboratory (Duan and Wang, 2010; Yin et al., 2015). The cells were maintained in Dulbecco's modified Eagle's medium (DMEM) supplemented with 10% fetal bovine serum, 2mM L-glutamine, 100 U/mL penicillin, 100 µg/mL streptomycin, and 150 µg/mL hygromycin B. The surface of the flasks was coated with 0.01% poly-D-lysine in phosphate-buffered saline to promote HEK293 cell attachment. The Madin-Darby Canine Kidney (MDCK) cells double-transfected with hOCT2 and hMATE1 or empty vector were previously generated in our laboratory (Yin et al., 2015). The MDCK cells were maintained in minimum essential medium (MEM) supplemented with 10% fetal bovine serum, 500 µg/mL G418, and 200 µg/mL hygromycin B. Cells were cultured in a 37°C incubator with 5% CO_2.

2.3.3 Uptake and Inhibition Assays in HEK293 Cells.

Uptake and inhibition assays were conducted as previously described with slight modifications to analyze mIBG by liquid chromatography tandem mass spectrometry (LC-MS/MS) (Duan and Wang, 2010; Wagner et al., 2017). The cells were seeded on 96-well plates and grown to greater than 90% confluency. Cells were washed with warm Hank's balanced salt solution (HBSS) buffer (1.3 mM $CaCl_2$, 0.4 mM KH_2PO_4, 0.8 mM $MgSO_4$, 0.3 mM Na_2HPO_4, 5.4 mM KCl, 137 mM NaCl, 4.2 mM $NaHCO_3$, and 5.6 mM D-glucose) three times. Experiments were initiated by addition of 100 µL of HBSS containing mIBG with or without an

inhibitor. Uptake was quenched by removing the warm HBSS with mIBG and subsequently washing the cells three times with 200 µL ice-cold HBSS. For hMATE1/2-K uptake assays, the pH in the HBSS was adjusted to pH 8.0 to create an outwardly directed proton gradient. After washing, cells were lysed with 200 µL acetonitrile containing glyburide as an internal standard. Twenty microliters of lysate were diluted in water to 10% acetonitrile for mIBG quantification. In all mIBG uptake experiments, the activities of the expressed transporters were verified with a ^{3}H- or ^{14}C-labeled probe substrate (MPP+ and metformin for hOCT1-3 and hMATE1/2-K; PAH for hOAT1; ES for hOAT3) (data not shown). In these reference experiments using probe substrates, cells were lysed with 100 µL 1 M NaOH and neutralized with 100 µL 1M HCl after one hour. At the end of the uptake experiment, a 150 µL aliquot of the lysates was taken from the cell lysate for analysis of the total radioactivity using a Tri-Carb Liquid Scintillation Counter (Perkin Elmer, Waltham, MA). Twenty microliters of the lysate were taken from the reference cell lysates to estimate the total protein amount using the BCA method. Variation in total protein amount was less than 10% CV.

2.3.4 Transwell Studies in hOCT2/hMATE1 double-transfected MDCK Cells.

mIBG transepithelial transport in control and hOCT2/hMATE1 double-transfected MDCK cells were conducted as previously described with slight modifications (Yin et al., 2015). MDCK cells were seeded at a density of 1 x 10^5 cells/mL on Falcon inserts (12-well, translucent, high-density PET membrane, 0.4 µM pore size) in 12-well plates and grown for five days. The inserts and wells were washed three times with warm HBSS. The transepithelial electrical resistance (TEER) was measured and monolayers with TEER values greater than 180 $\Omega*cm^2$ were used for the study. Apical-to-basal (A-to-B) transport of mIBG was initiated by adding 800 µL of HBSS (pH=6.0) containing 1 µM of mIBG to the A chamber. For B-to-A transport, 2 mL

of HBSS (pH=7.4) containing 1 µM of mIBG was added to the B chamber. For the inhibition study, the HBSS buffer in both chambers contained either no pyrimethamine or varying concentrations (10 or 100 µM) of pyrimethamine. At each time point, 50 µL of sample from the opposite chamber was collected for mIBG quantification and replaced with an equal volume of the appropriate HBSS buffer. At the end of the experiment, transport was terminated by removing the buffers from A and B chambers and the inserts were washed three times with ice-cold HBSS. To quantify mIBG by LC-MS/MS, 20 µL aliquots of the collected samples were diluted to 10% HBSS and with addition of 10% acetonitrile with 50 nM glyburide as the internal standard. Cells on the inserts were lysed by adding 1 mL of 10% acetonitrile containing 50 nM glyburide. The lysates were centrifuged and 100 µL of the lysate was analyzed for LC-MS/MS quantification of mIBG. Twenty microliters of the lysates were used for total protein quantification by BCA method.

2.3.5 Inhibition Screen of mIBG Uptake by FDA-Approved Oncology Drugs.

The FDA-approved oncology drugs were obtained from the Developmental Therapeutics Program at National Cancer Institute (NCI). The 96-well plates provided from NCI had 20 µL of 10 mM of each drug in DMSO. The drugs selected for screening were drugs used as part of the standard treatment for high-risk neuroblastoma or used in clinical trials in combination with ^{131}I-mIBG targeted radiotherapy. These drugs were diluted to 20 µM for the experiments. The uptake was initiated by addition of 1 µM mIBG to uptake buffer with or without the inhibitors and incubated for 2 minutes. At the end of the uptake experiment, cells were lysed by adding 200 µL of 10% acetonitrile containing 50 nM glyburide and were analyzed by LC-MS/MS to quantify mIBG.

2.3.6 Quantification of mIBG by LC-MS/MS

Due to concerns of radiation and rapid isotope decay ($t_{1/2}$ ~ 13 hours for ^{123}I and 8 days for ^{131}I), nonradioactive mIBG was used and quantified by LC-MS/MS. An AB-Sciex API 4000 QTrap mass spectrometer (Foster City, CA) coupled with an Acquity UPLC system (Waters Corporation, Milford, MA) operated in the positive electrospray ionization mode was used to quantify mIBG. The cell lysates or transwell samples diluted to 10% acetonitrile and containing 50 nM glyburide as an internal standard were injected (10 µL) onto the column (Zorbax Eclipse Plus C18, 2.1 x 50mm, 1.8 µm; Agilent Technologies, Santa Clara, CA). The mobile phase consisted of 0.1% (vol/vol) formic acid in water (A) and 0.1% (vol/vol) formic acid in acetonitrile (B) with gradient elution at 0.4 mL/min flow as follows: 3% B until 0.1 min, increased to 90% B by 2 min, then returning to 3% B over 0.1 min and holding with a total run time of 4 min. The mass-to-charge (*m/z*) transitions used for quantification of mIBG and glyburide were 276.1 → 216.97 and 494.1 → 369, respectively. The lower limit of quantification for mIBG was 0.1 nM, and the method was linear up to 8 µM. Instrument control and data processing were performed using Analyst software 1.6 (AB Sciex). Accuracy was within 20% for each batch.

2.3.7 Data Analysis.

The uptake and inhibition studies were performed in triplicate and repeated three times independently. The data were fitted by non-linear regression using GraphPad Prism 7.0 (GraphPad Software Inc., La Jolla, CA) to obtain graphs and kinetic parameters. The uptake kinetics data were fitted to the Michaelis-Menten equation:

Equation 2.1: $$v = \frac{V_{max} * [S]}{K_m + [S]}$$

where v is the uptake velocity, V_{max} is the maximum uptake velocity of the system, K_m is the Michaelis-Menten constant, and [S] is the substrate concentration. For the transwell experiments, the apparent permeability (P_{app}) of mIBG was calculated using the following equation:

Equation 2.2: $$P_{app} = \left(\frac{dQ}{dt}\right) \Big/ (A * C_o)$$

where Q is the amount of compound transporter over time, t is time, A is the insert membrane surface area, and C_o is the initial compound concentration in the donor chamber. For the dose-dependent inhibition of transporter-mediated uptake of mIBG, the IC_{50} was calculated using the following equation:

Equation 2.3: $$v = \text{Bottom} + \frac{\text{Top}-\text{Bottom}}{1+\left(\frac{[I]}{IC_{50}}\right)^H}$$

where v is the rate of uptake in the presence of the inhibitor, bottom is the non-inhibitable baseline value, top is the rate of uptake in the absence of the inhibitor, [I] is the concentration of the inhibitor, IC_{50} is the concentration to inhibit 50% of the transporter activity, and H is the Hill coefficient. Statistical significance was determined using a one-way ANOVA followed by Dunnett's test or an unpaired Student's t test using the Bonferroni method as specified in the figure legends. A P value less than 0.05 was considered statistically significant.

2.4 RESULTS

2.4.1 Uptake of mIBG by Organic Cation and Anion Transporters

Uptake of mIBG was measured in vector-transfected HEK293 cells and in cells stably expressing hOCT1, hOCT2, hOCT3, hMATE1, or hMATE2-K. We also tested hOAT1 and hOAT3 as some drugs can be transported by both renal organic cation and anion transporters (Yin et al., 2019). Compared to the vector control, mIBG (1 μM) uptake was substantially increased in

cells expressing hOCT1, hOCT2, hOCT3, hMATE1, and hMATE2-K after a 30-minute incubation (**Figure 2.1A** and **B)**. Cells expressing the renal organic anion transporters, hOAT1 or hOAT3, showed a negligible increase in mIBG uptake (**Figure 2.1C**). The classic OAT inhibitor probenecid had no effect in mIBG uptake in these cells. These data demonstrated that mIBG is a substrate of hOCT1-3 and hMATE1/2-K, but not hOAT1/3.

2.4.2 Time-dependent mIBG Uptake by hNET, hOCT1, hOCT2, and hOCT3.

Selection of time points in the initial linear phase (i.e. initial uptake rates) is critical for accurate determination of transporter kinetic parameters (Brouwer et al., 2013). To define the initial rate range of mIBG uptake by hNET, hOCT1, hOCT2 and hOCT3, time-dependent uptake of mIBG (1 μM) was examined. As shown in **Figure 2.2**, mIBG uptake in hNET-expressing cells increased linearly in the early time points and reached plateau around 20 min. Similarly, mIBG uptake in cells expressing hOCT1, hOCT2 and hOCT3 also increased linearly within the first 2-5 min and reached a plateau around 20 min. In contrast, mIBG uptake in vector-transfected HEK293 cells were much lower at all tested time points. At 45 min, mIBG concentrations in cells expressing hNET and hOCT1/2/3 were about 9- to 62-fold higher than that in control cells.

2.4.3 Concentration-dependent mIBG Uptake by hNET, hOCT1, hOCT2, and hOCT3.

mIBG time course in hNET and hOCT1-3 expressing cells showed that the initial linear phase lasted up to 5-10 min (**Figure 2.2**). Hence, kinetic studies were performed using 2 min as the incubation time. Transporter-specific uptake was obtained by subtracting uptake in the control cells from that in transporter-expressing cells. As shown in **Figure 2.3**, hNET, hOCT1, hOCT2, and hOCT3 mediated uptake of mIBG display typical Michaelis–Menten saturation curves. The corresponding K_m and V_{max} values for each transporter were derived from nonlinear

regression fitting to equation 1 and summarized in **Table 2.1**. Interestingly, hOCT1-3 displayed similar apparent affinities for mIBG in the low micromolar range (K_m values of 19.5 ± 6.9, 17.2 ± 2.8, 14.5 ± 7.1 μM for hOCT1, hOCT2, and hOCT3, respectively). The K_m values for hOCT1-3 were about 2-fold higher than that of hNET (8.7 ± 1.4 μM) determined under the same experimental condition (**Table 2.1**).

2.4.4 mIBG Uptake Kinetics by hMATE1 and hMATE2-K.

hMATE1 and hMATE2-K function as proton/organic cation exchangers and require a proton gradient to drive substrate transport (Otsuka et al., 2005). The transport kinetics of mIBG for hMATE1 and hMATE2-K were determined in uptake studies with the buffer pH adjusted to 8.0. Similar to hOCT1-3, hMATE1/2-K exhibited linear uptake in the first 5 min (**Figure 2.4A** and **B**) and kinetic measurement was conducted with a 2-min incubation time. hMATE1 and hMATE2-K mediated uptake of mIBG was saturable with K_m values of 17.7 ± 10.9 and 12.6 ± 5.6 μM, respectively (**Figure 2.4C** and **D**, **Table 2.1**). These K_m values are comparable to those of hOCT1-3, suggesting mIBG interacts with hMATEs and hOCTs with similar apparent affinities.

2.4.5 Transcellular Transport of mIBG in hOCT2/hMATE1-Transfected MDCK Cells.

In renal proximal tubule cells, hOCT2 and hMATE1/2-K cooperatively mediate transepithelial secretion of organic cations from the blood side to the urine side. To determine whether mIBG can be secreted by this pathway, transepithelial flux of mIBG was measured in MDCK cells stably expressing hOCT2 and hMATE1. Transport studies were performed under a pH gradient (apical pH 6.0 and basal pH 7.4) to simulate the physiological condition. ^{14}C-Metformin and ^{3}H-Mannitol transport in this system were run in parallel to ensure monolayer integrity and transporter activity (data not shown). The mIBG flux rate was constant for 120 minutes in both control and hOCT2/hMATE1 cells. In the hOCT2/hMATE1 double-transfected

cells, flux of mIBG in the B-to-A direction was much greater than in the A-to-B direction (**Figure 2.5A**). In contrast, mIBG flux in the control cells in B-to-A and A-to-B directions was substantially lower. The calculated B-to-A permeability of mIBG in hOCT2/hMATE1-transfected cells was 12.6 ± 2.7 x 10^{-6} cm/sec, which is 20-fold higher than control cells (**Figure 2.5B**), suggesting that the presence of hOCT2/hMATE1 in proximal tubules cells greatly facilitates secretory transport of mIBG from the blood side to the lumen side. Interestingly, despite a 20-fold increase in mIBG B-to-A permeability, intracellular mIBG accumulation in hOCT2/hMATE1 cells was marginally increased when compared to control cells (**Figure 2.5C**). Pyrimethamine, a known inhibitor of hMATE1/2-K and hOCT2, inhibited the B-to-A flux and permeability of mIBG in hOCT2/hMATE1 double-transfected cells in a dose-dependent manner, but had no effect in vector-transfected control cells (**Figure 2.6**), confirming that the observed vectorial transport of mIBG was mediated by hOCT2/hMATE1. These proof-of-concept studies suggest that mIBG undergoes hOCT2/hMATE1-mediated secretion in the kidney. Given that mIBG is also transported by hMATE2-K with similar apparent affinities, we expect that hMATE2-K contributes to mIBG efflux alongside hMATE1 at the apical membrane of renal proximal tubule cells.

2.4.6 Inhibitory Effect of Selected FDA-approved Oncology Drugs on mIBG Uptake by hOCT1-3 and hMATE1/2-K.

The uptake and transwell studies strongly suggest that mIBG can be taken up into normal tissues by hOCTs and secreted by the renal hOCT2/hMATEs transporters. As mIBG is frequently used with other anticancer drugs, this raises a concern of potential drug-drug interaction (DDI) at the site of these transporters. We therefore screened 23 FDA-approved oncology drugs obtained from NCI. The drugs are either used in standard treatment regimens of high-risk neuroblastoma or in clinical trials for combination use with ^{131}I-mIBG therapy. These drugs were screened at a

relatively low concentration (20 μM) to identify potential inhibitors of mIBG transport mediated by hOCT1-3 and hMATE1/2-K. At the tested concentration, irinotecan selectively inhibited hOCT1-mediated mIBG uptake by more than 50% (**Figure 2.7A**). Dose-dependent inhibition studies further revealed that irinotecan was at least 17-fold more potent for hOCT1 than for hOCT2 and hOCT3 (**Figure 2.8A**, **Table 2.2**). Several tyrosine kinase inhibitors (gefitinib, sunitinib, crizotinib, vandetanib) inhibited one or more hOCTs by more than 50% (**Figure 2.7A**). Interestingly, crizotinib, a targeted tyrosine kinase inhibitor (TKI) used in the treatment of high-risk neuroblastoma, showed potent and preferential inhibition of hOCT3, blocking hOCT3-mediated mIBG uptake by approximately 85%. The IC_{50} determined from the dose-dependent inhibition studies showed that crizotinib inhibition of hOCT3 was 6.7-fold and 18-fold more potent than for hOCT2 and hOCT1, respectively (**Figure 2.8B**, **Table 2.2**). Uptake of mIBG by hMATE1 and hMATE2-K appeared to be less affected by the tested drugs (**Figure 2.7B**). Crizotinib and *cis*-retinoic acid showed 25-55% inhibition of hMATE1 and hMATE2-K. No other compounds showed greater than 50% inhibition of hMATE1 and hMATE2-K at the tested concentration.

2.5 DISCUSSION

The use of radiolabeled mIBG has been routinely incorporated into the diagnosis of neuroblastoma and other neuroendocrine tumors. With the recent FDA approval of high dose ^{131}I-mIBG for the treatment of advanced pheochromocytoma and its ongoing clinical trials to treat high-risk neuroblastoma, there is a great need to understand the molecular mechanisms involved in mIBG disposition in normal organs and tissues. Previously, mIBG was reported to be a substrate for OCT1-3 and MATE1/2-K (Bayer et al., 2009; Ito et al., 2012). However, the transport kinetics of mIBG has not been analyzed for any of these transporters. It is also unknown if renal excretion, the major pathway of mIBG elimination, involves OCT2/MATEs.

In addition, the potential of mIBG interaction with other anticancer drugs at the site of OCTs and MATEs has not been characterized. In this study, we comprehensively analyzed the transport kinetics of hOCT1-3 and hMATE1/2-K and demonstrated that renal elimination of mIBG involves the hOCT2 and hMATE1/2-K. After screening 23 oncology drugs, we identified several selective inhibitors for mIBG transport. Findings from our study have important implications for using mIBG as a theranostic agent for neuroblastoma and other neuroendocrine cancers.

Our detailed kinetic analysis showed that hOCT1-3 and hMATE1/2-K have similar K_m values towards mIBG ranging from 14.5 to 19.5 μM (**Figure 2.3**, **Figure 2.4**, **Table 2.1**). These K_m values are only slightly higher than that of hNET (~8.7 μM) determined under the same experimental conditions (**Figure 2.3**, **Table 2.1**), suggesting that the polyspecific organic cation transporters and NET have comparable affinities for mIBG. Previously, using transfected HeLa cells, Glowniak *et al.* reported a much lower K_m (264 nM) for NET (Glowniak et al., 1993). The discrepancy may be due to differences in expression systems and uptake conditions, as the Glowniak study did not determine the initial rate range and used a much longer incubation time in the kinetic studies. The total plasma concentrations of mIBG estimated from radioactivity in high dose ^{131}I-mIBG therapy are typically in the nanomolar range (Ehninger et al., 1987). These concentrations are well below our determined K_m values for all tested transporters, suggesting that at clinically used doses, mIBG transport mediated by these transporters is unlikely to be saturated. Our kinetic analyses also revealed that hOCT1-3 and hNET have comparable K_m values towards mIBG, suggesting that these transporters are somewhat similarly competitive in binding to extracellular mIBG. Nevertheless, as OCTs are not expressed in neuroblastoma (Dubois et al.,

2012), selective inhibition of OCTs may provide a valid approach to enhance tumor specific uptake of ^{131}I-mIBG.

The liver, heart, salivary glands, and intestines are the main tissues with high mIBG accumulation in humans (Chin et al., 2014; Coleman et al., 2009). Consistently, cardiac, hepatic, and salivary gland toxicities have been observed with high dose ^{131}I-mIBG therapy (Bleeker et al., 2013; Modak et al., 2008; Parisi et al., 2016). Based on *in vitro* mIBG transport (**Figure 2.2**, **Figure 2.3**, **Table 2.1**) and transporter tissue expression, we propose that hOCT1 and hOCT3 are important determinants for mIBG uptake and accumulation in normal tissues as illustrated in **Figure 2.9**. While the liver is not a site for mIBG elimination, hepatic accumulation accounts for approximately 30% of injected dose (Chin et al., 2014; Parisi et al., 2016). A previous study done in *Oct1*$^{-/-}$ mice observed around a 75% decrease in liver concentrations of mIBG 30 min after intravenous injection (Jonker et al., 2001). Using *Oct3*$^{-/-}$ mice, we previously showed that Oct3 has a major impact on organic cation uptake in salivary glands and heart *in vivo* (Lee et al., 2014; Lee et al., 2018; Wagner et al., 2018). Accumulation of metformin, a probe substrate of the OCTs, is substantially reduced in salivary glands and heart in *Oct3*$^{-/-}$ mice (Lee et al., 2014). Previously, Bayer *et al.* proposed to improve tumor selective uptake of mIBG by reducing Oct3-mediated tissue uptake (Bayer et al., 2016). They showed that mIBG uptake was decreased in small intestine and kidney in mice treated with corticosteroids. However, corticosteroids are not specific inhibitors of OCT3 and salivary gland accumulation of mIBG was not analyzed in their study. Characterization of mIBG disposition in *Oct3*$^{-/-}$ mice should provide more insightful information regarding the *in vivo* impact of Oct3 on mIBG tissue distribution.

mIBG is almost exclusively eliminated by the kidney with more than 90% of the administered dose excreted unchanged in the urine (Lashford et al., 1988). Although the FDA

labels for Azedra and AdreView only state that renal elimination of mIBG occurs by glomerular filtration, several pharmacokinetic studies suggested a net tubular secretion component (Blake et al., 1989; Ehninger et al., 1987). For example, the renal clearance of mIBG was reported to be 226 mL/min in a patient cohort with a mean glomerular filtration rate (GFR) of 94 mL/min (Blake et al., 1989). Considering the fraction unbound, f_u, provided in the Azedra FDA label ($f_u = 0.39$), the estimated glomerular filtration clearance (f_u*GFR) is about 37 mL/min, suggesting that about 84% of the dose is eliminated through tubular secretion. Our data strongly support that mIBG undergoes active renal secretion sequentially mediated by hOCT2 and hMATE1/2-K (**Figure 2.1**, **Figure 2.5**, **Figure 2.6**, **Figure 2.9**). Interestingly, despite a large increase in mIBG B-to-A permeability, intracellular mIBG accumulation in the hOCT2/hMATE1 cells was minimal (**Figure 2.5C**). These observations agree with ^{123}I-mIBG whole-body imaging results which revealed rapid and substantial bladder accumulation of ^{123}I-mIBG but only moderate kidney accumulation in both neuroblastoma patients and healthy adults (Chin et al., 2014; Lashford et al., 1988). These data suggest that hOCT2-mediated uptake, but not hMATE-mediated efflux, is likely the rate-limiting step in the secretion process. Our findings have important implications for mIBG therapy as changes in hOCT2 and/or hMATE activities could alter the pharmacokinetics and toxicity of radioactive mIBG. For instance, inhibition of the basolateral hOCT2 may reduce mIBG renal clearance, resulting in increased systemic exposure. On the other hand, blockage of hMATE-mediated efflux may increase intracellular accumulation of radioactive mIBG in proximal tubular cells, leading to increased risk of nephrotoxicity.

Transporters are increasingly recognized as targets for clinically relevant DDIs and assessment of transporter-mediated DDIs are recommended by the 2020 FDA drug interaction guidance for drug development. This raises a concern of potential ^{131}I-mIBG interaction with drugs

used either in conventional chemotherapy for neuroblastoma, in combination as radiosensitizers, or in induction chemotherapy. We thus explored the potential of 23 oncology drugs to inhibit mIBG uptake mediated by hOCT1-3 and hMATE1/2-K (**Figure 2.7**). As OCTs and MATEs are known to exhibit substrate-dependent inhibition (Belzer et al., 2013; Martinez-Guerrero and Wright, 2013; Yin et al., 2016), the inhibition screen was carried out using mIBG as the substrate. The majority of the tested drugs showed moderate to no inhibition at a concentration (i.e., 20 µM) much greater than their therapeutic unbound concentrations (**Figure 2.7**). However, irinotecan potently and selectively inhibited hOCT1 (**Figure 2.7A**, **Figure 2.8A**, **Table 2.2**). Irinotecan is currently being explored as a radiosensitizer in combination with ^{131}I-mIBG. Considering a typical range of unbound maximum plasma concentrations of 1.2 to 6.0 µM in cancer patients (Chabot, 1997), there is a potential for irinotecan to inhibit hOCT1-mediated hepatic uptake of ^{131}I-mIBG (**Figure 2.8**). This may reduce liver accumulation of ^{131}I-mIBG, leading to a potentially beneficial effect in reducing hepatic toxicities.

Several tyrosine kinase inhibitors (TKIs) are in clinical trials as treatments for neuroblastoma and other neuroendocrine tumors (Umapathy et al., 2019). The anaplastic lymphoma kinase (ALK) is found in the majority of neuroblastoma tumors (Trigg and Turner, 2018), and ALK mutation is associated with poor prognosis (Bresler et al., 2014; Janoueix-Lerosey et al., 2008). Crizotinib, an inhibitor of ALK, has shown improvements in the response rates for high-risk neuroblastoma in ALK-positive tumors (Mosse et al., 2013). Crizotinib exhibits potent and preferential inhibition of hOCT3 with a calculated IC_{50} of 2.14 µM (**Figure 2.7A**, **Figure 2.8B**, **Table 2.2**). The total and unbound maximum plasma concentrations of crizotinib in pediatric cancer patients are 1.6 µM and 0.14 µM, respectively (Balis et al., 2017). Although the unbound plasma concentrations of crizotinib may not be sufficient to inhibit hOCT3, TKIs can

accumulate in cells and may also exhibit novel protein kinase-dependent inhibition of the OCTs (Sprowl et al., 2016). Thus, further evaluation is necessary to evaluate the potential of crizotinib in inhibiting OCT3-mediated mIBG uptake *in vivo* in neuroblastoma patients.

In summary, our study demonstrated that mIBG is efficiently transported by hOCT1-3 and hMATE1/2-K with similar affinities. Our data suggest that hOCT1 and hOCT3 are important determinants for mIBG distribution into normal tissues, whereas hOCT2 and hMATE1/2-K are involved in its renal elimination. mIBG uptake by these transporters can be differentially inhibited by several FDA-approved drugs used in the treatment for neuroblastoma. These findings may help to predict and prevent adverse drug interaction with therapeutic ^{131}I-mIBG as well as develop clinical strategies to reduce ^{131}I-mIBG accumulation and toxicity in normal tissues and organs. Findings from our study have important implications for using mIBG as a theranostic agent for neuroblastoma and other neuroendocrine cancers.

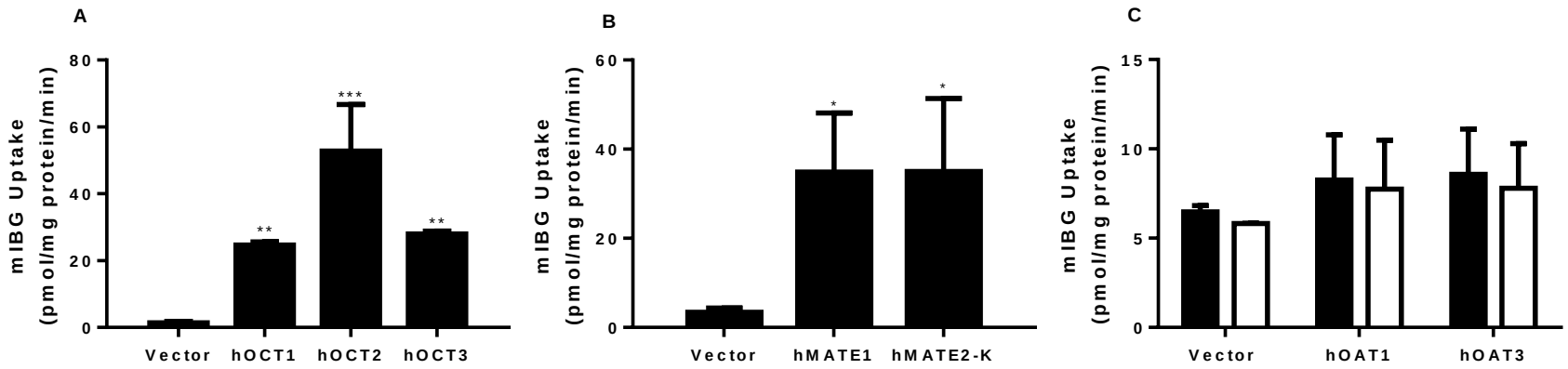

Figure 2.1. Uptake of mIBG by selected drug transporters.

Uptake of 1 µM mIBG by hOCT1-3 (A), hMATE1/2-K (B), and hOAT1/3 (C) was measured in both transporter-expressing and vector control HEK293 cells. For hOAT1/3, the uptake of mIBG was measured in the absence (filled bars) and in the presence of 100 µM probenecid (empty bars). The uptake was measured after a 30-minute incubation at 37°C. Data are presented as the mean ± S.D from three independent experiments. The uptake of mIBG in transporter-expressing HEK293 cells was compared to control HEK293 cells ($^{*}P < 0.05$; $^{**}P < 0.01$; $^{***}P < 0.001$). Statistical significance was determined using a one-way ANOVA followed by Dunnett's test.

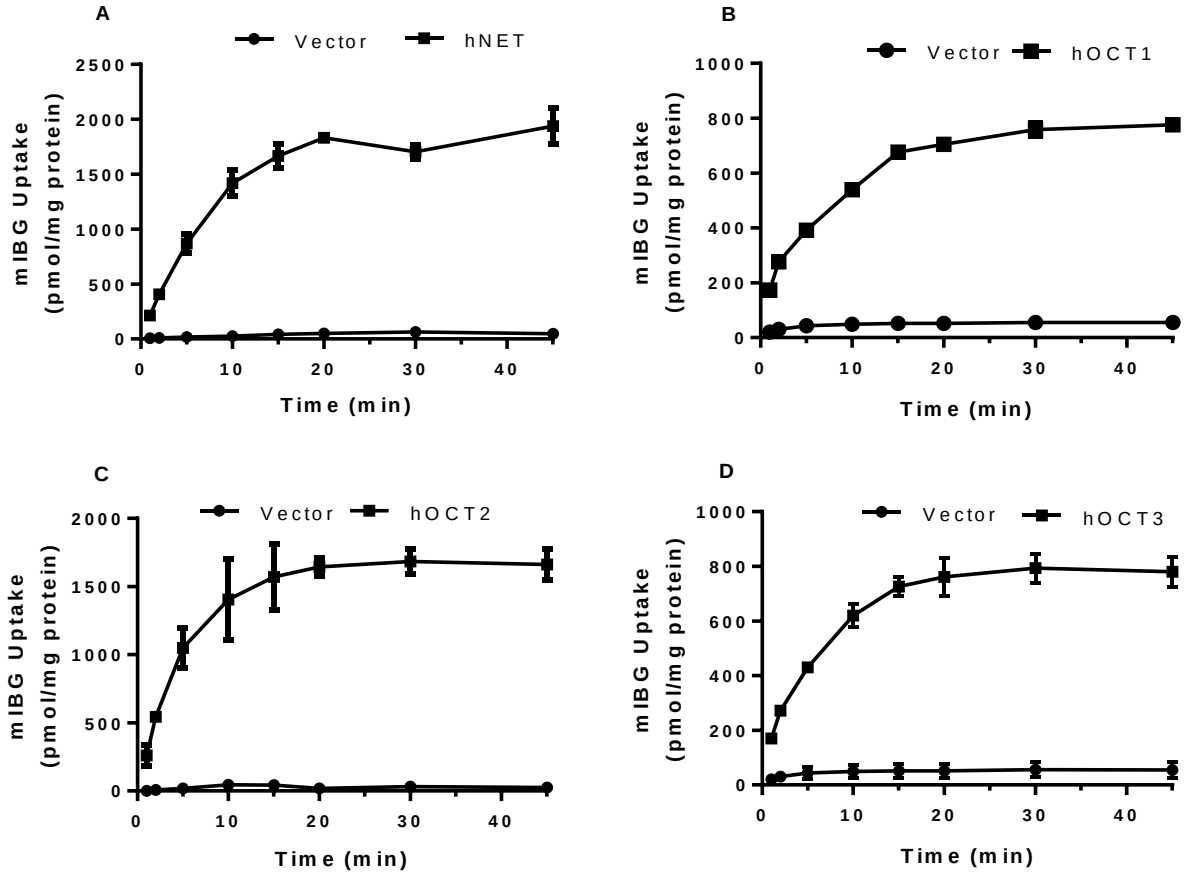

Figure 2.2. Time-dependent uptake of mIBG by hNET and hOCT1-3.

Time-dependent uptake of 1 μM mIBG was measured in control and HEK293 cells expressing hNET (A), hOCT1 (B), hOCT2 (C), and hOCT3 (D) at specified time points at 37°C. Time courses were performed independently three times, and results from one representative experiment conducted in triplicate are shown. Data is presented as mean ± S.D.

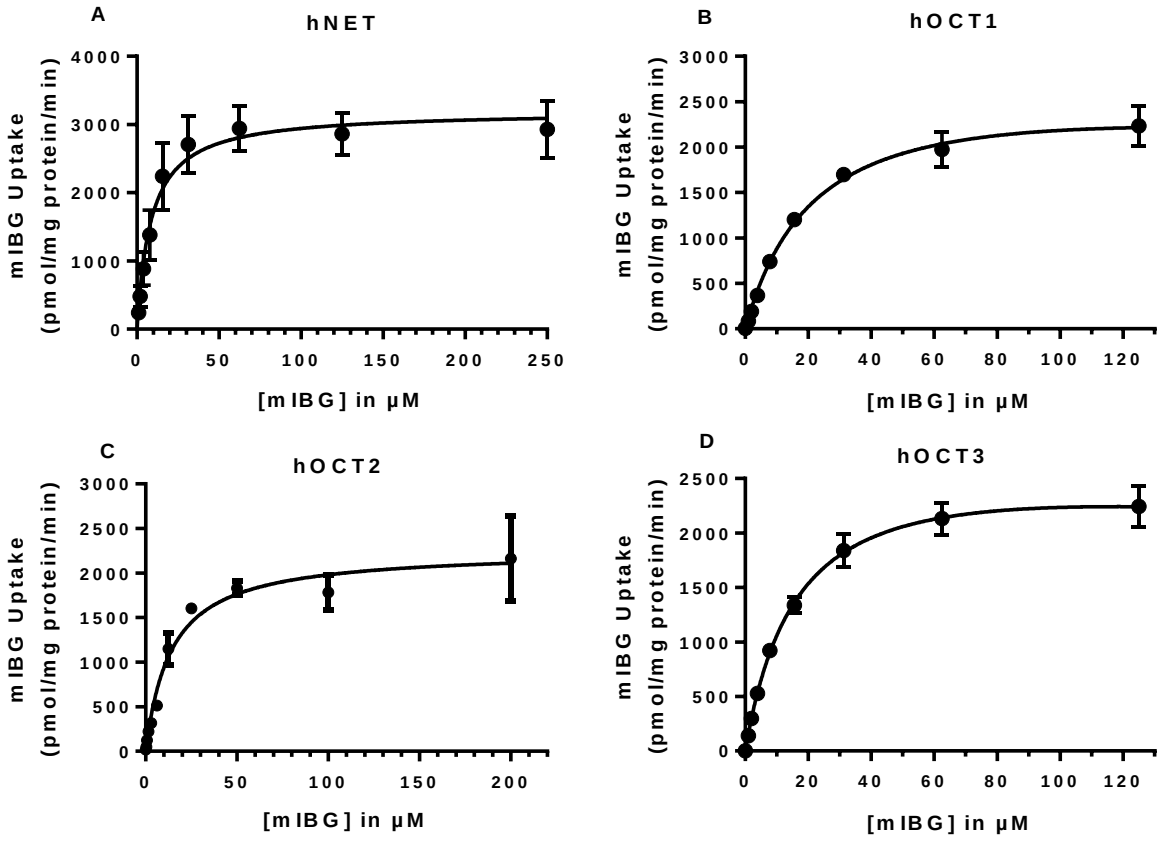

Figure 2.3. Concentration-dependent uptake of mIBG by hNET and hOCT1-3.

Concentration-dependent uptake of mIBG was measured in control and HEK293 cells expressing hNET (A), hOCT1 (B), hOCT2 (C), hOCT3 (D) after a 2-minute incubation. Transporter-specific uptake was obtained by subtracting the activity in control cells from the activity in transporter-expressing cells. A non-linear regression was fit to the data using **Equation 2.1**. Concentration-dependent uptake was performed in triplicate in three independent experiments for each transporter, and results from one representative experiment are shown. Data is presented as mean ± S.D.

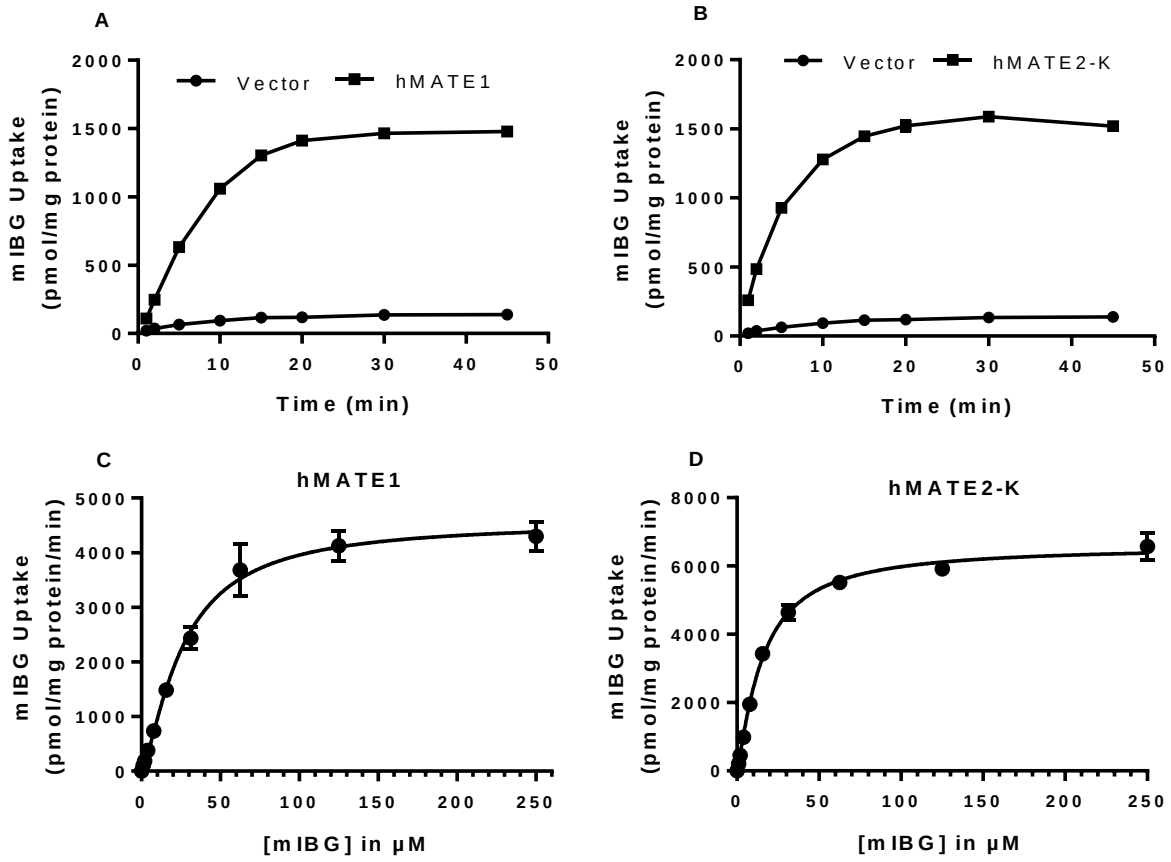

Figure 2.4. mIBG uptake kinetics by hMATE1/2-K.

The time-dependent uptake of 1 µM mIBG was measured in control and HEK293 cells expressing hMATE1 (A), hMATE2-K (B) at specified time points at 37°C in HBSS buffer with pH adjusted to 8.0. Concentration-dependent uptake of mIBG was measured in control and HEK293 cells expressing hMATE1 (C) and hMATE2-K (D) after a 2-minute incubation. Transporter-specific uptake was obtained by subtracting the activity in control cells from the activity in transporter-expressing cells. A non-linear regression was fit to the data using **Equation 2.1**. Uptake was performed in triplicate in three independent experiments, and results from one representative experiment are shown. Data is presented as mean ± S.D.

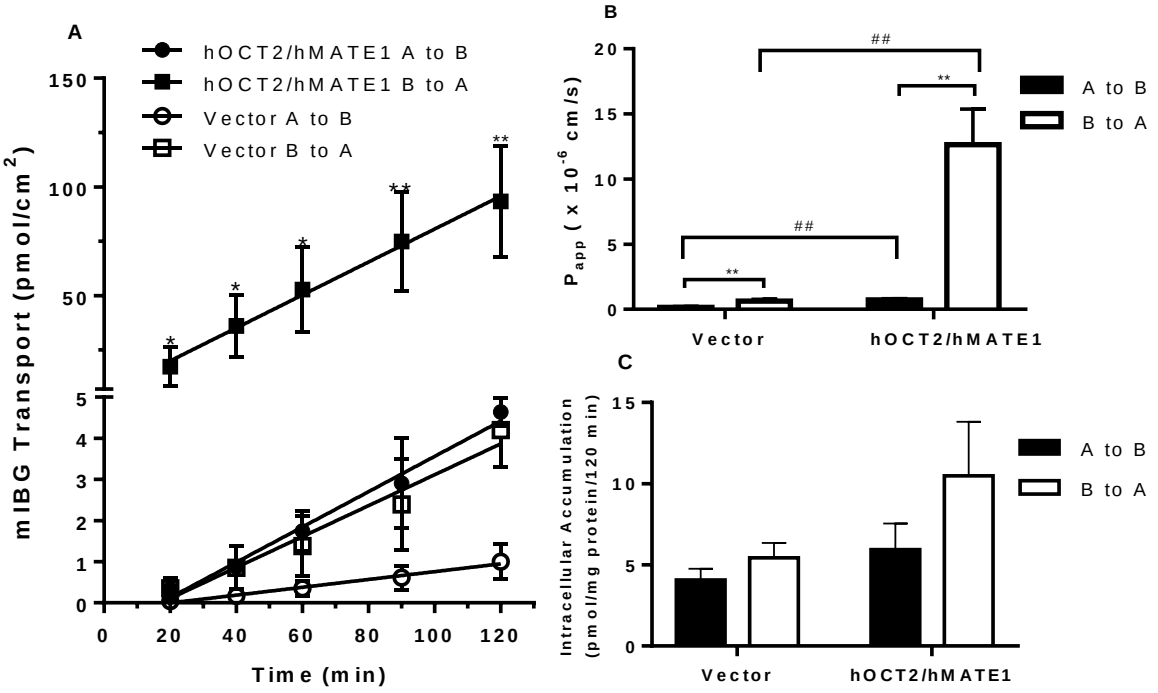

Figure 2.5. Transcellular flux, permeability, and intracellular accumulation of mIBG in vector-transfected (control) and hOCT2/hMATE1 double-transfected MDCK cells.

(A) mIBG transport in control and hOCT2/hMATE1 MDCK monolayers. The MDCK cells were grown for 5 days to form a monolayer on the Falcon insert. On the fifth day, the cells were washed and incubated in HBSS buffer containing 1 μM mIBG in either the apical or basal chamber to initiate transport. An aliquot of buffer (50 μL) was taken periodically from the receiving chamber and replenished with an equal volume of HBSS buffer. mIBG in the aliquot was subsequently measured by LC-MS/MS. The pH of apical and basal chamber was 6.0 and 7.4, respectively. A-to-B, apical to basal; B-to-A, basal to apical. (B) Permeability of mIBG was calculated using **Equation 2.2**. (C) Intracellular accumulation of mIBG was measured at the end of the 120-minute incubation. Transport, permeability, and accumulation in the B-to-A direction were compared to those in the A-to-B direction ($^{*}P < 0.05$; $^{**}P < 0.01$; $^{***}P < 0.001$). Permeability and accumulation in hOCT2/hMATE1 MDCK cells were also compared to those in

the control cells ($^{\#}P < 0.05$; $^{\#\#}P < 0.01$; $^{\#\#\#}P < 0.001$). Statistical significance was determined using an unpaired Student's t test with the Bonferroni method to correct for multiple comparisons. Each data point represents the mean ± S.D from three independent experiments.

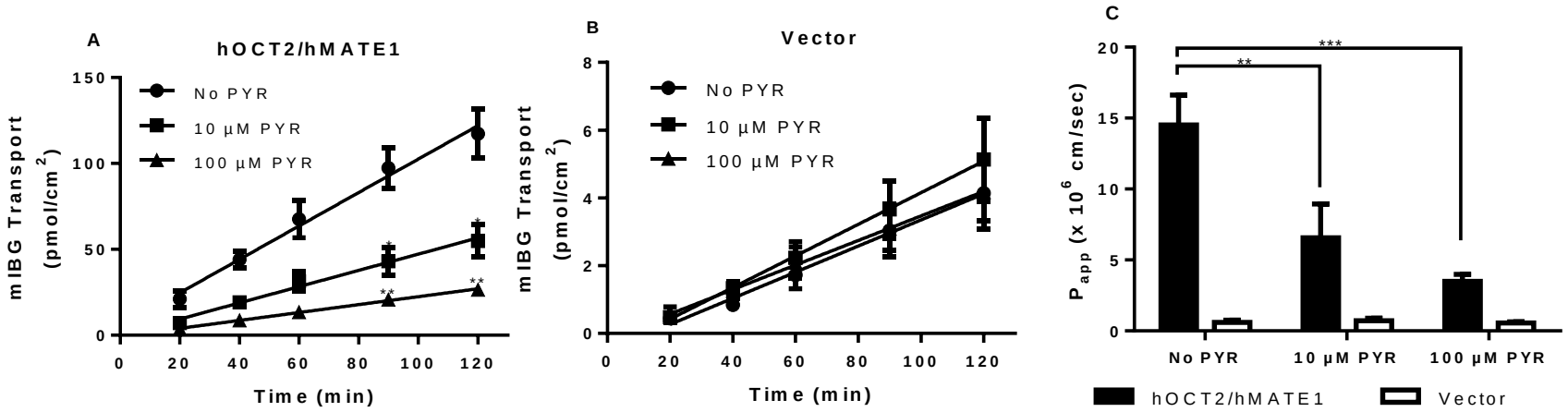

Figure 2.6. Effect of pyrimethamine on B-to-A flux of mIBG in hOCT2/hMATE1 double-transfected and control MDCK cells. mIBG transport in hOCT2/hMATE1 (A) and vector control (B) MDCK monolayers. Cells were incubated in HBSS buffer containing 1 µM mIBG in the basal chamber. B-to-A flux of mIBG was measured in the absence or presence of 10 µM or 100 µM pyrimethamine added to both chamber A and B. At various time points, 50 µL from chamber A was taken and replenished with an equal volume of HBSS buffer with the corresponding concentration of pyrimethamine. The pH of chamber A and B was maintained at 6.0 and 7.4, respectively. (C) Permeability of mIBG was calculated using **Equation 2.2**. The time course data were fitted with linear regression. B-to-A transport and permeability of mIBG in the presence of 10 µM or 100 µM pyrimethamine in hOCT2/hMATE1 MDCK cells were compared to those in the absence of pyrimethamine ($^{*}P < 0.05$; $^{**}P < 0.01$; $^{***}P < 0.001$). The statistical significance was determined using an unpaired Student's t test with the Bonferroni method to correct for multiple comparisons. Each data point represents the mean ± S.D from three independent experiments.

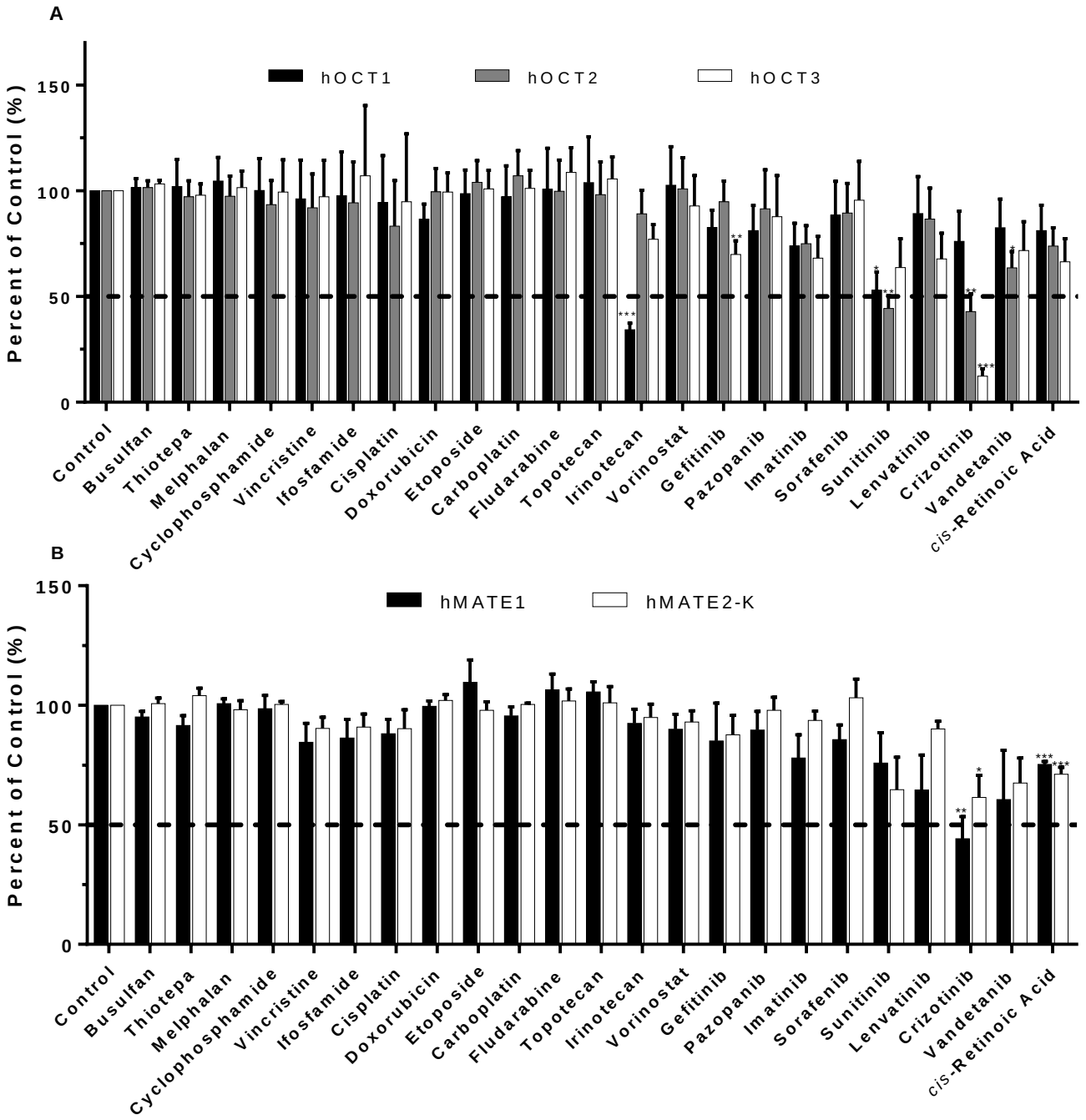
A
hOCT1
hOCT2
hOCT3
Percent of Control (%)
150
100
50
0
Control
Busulfan
Thiotepa
Melphalan
Cyclophosphamide
Vincristine
Ifosfamide
Cisplatin
Doxorubicin
Etoposide
Carboplatin
Fludarabine
Topotecan
Irinotecan
Vorinostat
Gefitinib
Pazopanib
Imatinib
Sorafenib
Sunitinib
Lenvatinib
Crizotinib
Vandetanib
cis-Retinoic Acid
B
hMATE1
hMATE2-K
Percent of Control (%)
150
100
50
0
Control
Busulfan
Thiotepa
Melphalan
Cyclophosphamide
Vincristine
Ifosfamide
Cisplatin
Doxorubicin
Etoposide
Carboplatin
Fludarabine
Topotecan
Irinotecan
Vorinostat
Gefitinib
Pazopanib
Imatinib
Sorafenib
Sunitinib
Lenvatinib
Crizotinib
Vandetanib
cis-Retinoic Acid

Figure 2.7. Effect of selected oncology drugs on mIBG uptake mediated by hOCT1-3 and hMATE1/2-K.

The selected FDA-approved oncology drugs were obtained from the National Cancer Institute. The 2-minute uptake of 1 µM mIBG was measured in the absence and presence of 20 µM of the selected oncology drugs in vector or HEK293 cells expressing hOCT1-3 (A) or hMATE1/2-K (B). Transporter-specific uptake of mIBG was obtained by subtracting the activity in vector-transfected cells from the activity in transporter-expressing cells. The uptake data were expressed as a percentage of mIBG uptake in in the absence of an inhibitor (control). The uptake of mIBG in the presence of an oncology drug was compared to the control ($^{*}P < 0.05$; $^{**}P < 0.01$; $^{***}P < 0.001$). Statistical significance was determined using an unpaired Student's t test with the Bonferroni method to correct for multiple comparisons. Each bar indicates the mean ± S.E. from three independent experiments. The horizontal dashed lines indicate 50% inhibition.

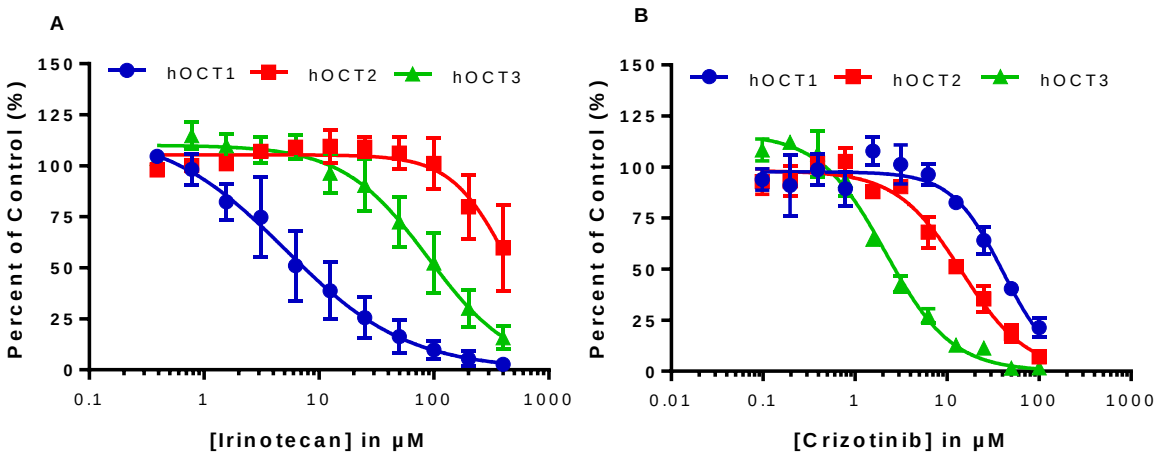

Figure 2.8. Dose-dependent inhibition of hOCT1-3 by irinotecan and crizotinib.

Uptake of 1 µM mIBG in the absence and presence of irinotecan (A) and crizotinib (B) was measured in vector and HEK293 cells expressing hOCT1, hOCT2, and hOCT3 for 2 minutes at 37°C. Transporter-specific uptake of mIBG was obtained by subtracting the activity in vector-transfected cells from the activity in transporter-expressing cells. The uptake data were expressed as a percentage of mIBG uptake in the absence of irinotecan or crizotinib (control). A non-linear regression was fit to the data using **Equation 2.3**. Each data point represents the mean ± S.E. from three independent experiments.

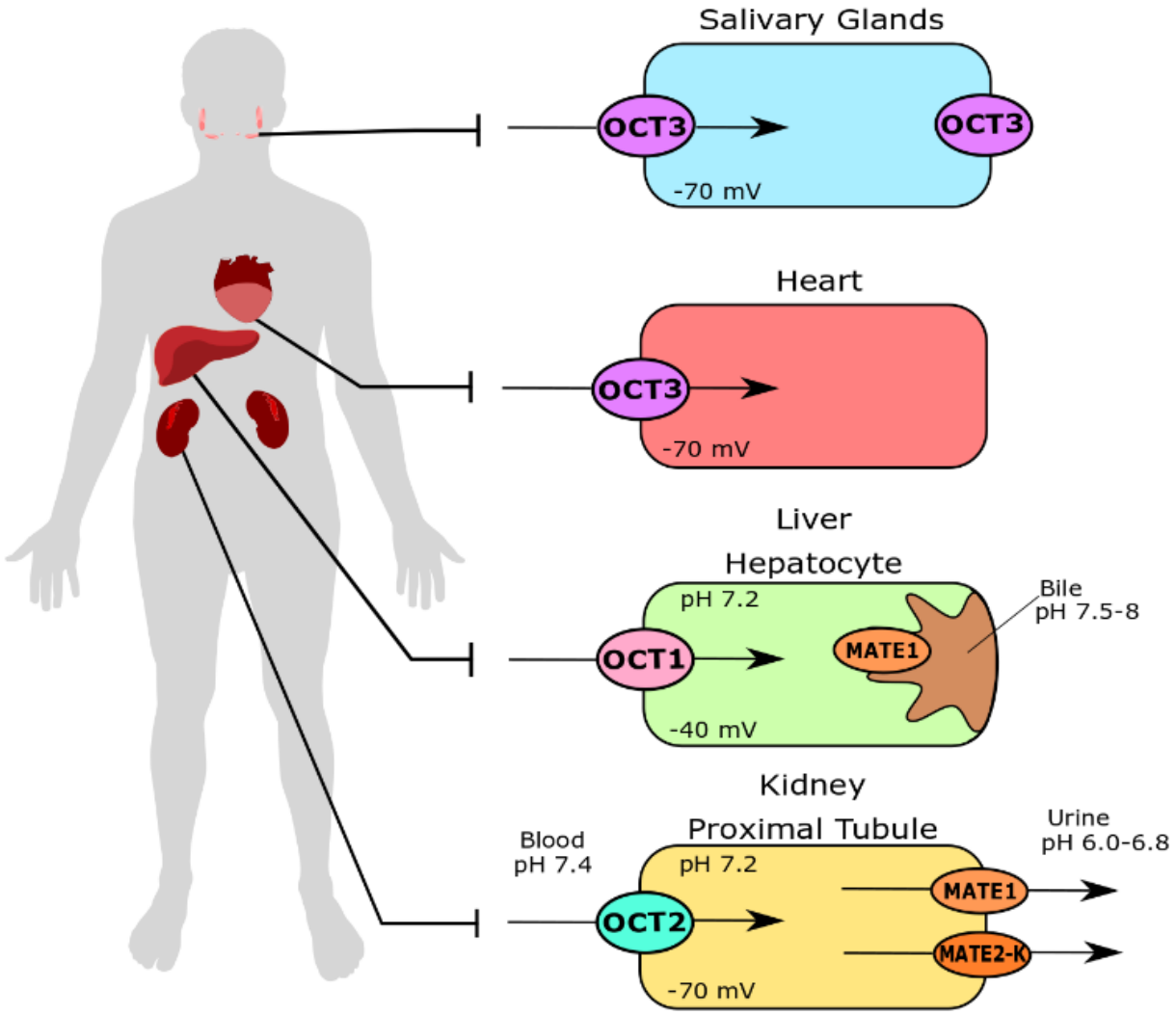

Figure 2.9. Proposed roles of polyspecific organic cation transporters in mIBG disposition.

Table 2.1. Kinetic parameters of mIBG uptake by hNET, hOCT1-3, and hMATE1/2-K. Concentration-dependent uptake was determined in three independent experiments. The K_m and V_{max} values for each experiment were obtained by fitting a non-linear regression using **Equation 2.1** to the data from **Figure 2.3** and **Figure 2.4C** and **D**. The mean values (mean ± S.D.) of the K_m or V_{max} from the three independent experiments are shown in the table.

Transporter	K_m (μM)	V_{max} (nmol/mg protein/min)
hNET	8.7 ± 1.4	6.40 ± 0.25
hOCT1	19.5 ± 6.9	2.46 ± 0.29
hOCT2	17.2 ± 2.8	2.45 ± 0.10
hOCT3	14.5 ± 7.1	3.14 ± 0.48
hMATE1	17.7 ± 10.9	2.60 ± 0.45
hMATE2-K	12.6 ± 5.6	4.28 ± 0.50

Table 2.2. The IC_{50} values of irinotecan and crizotinib for hOCT1-3 mediated mIBG uptake. Inhibition of mIBG uptake by irinotecan and crizotinib was determined in three independent experiments. The IC_{50} values for each experiment were determined by fitting a non-linear regression using **Equation 2.3** to the data from **Figure 2.8**. The mean values (mean ± S.D.) of the IC_{50} from the three independent experiments are shown in the table.

	IC_{50} (μM)	
	Irinotecan	Crizotinib
hOCT1	5.10 ± 2.70	40.3 ± 5.5
hOCT2	>400	14.3 ± 1.7
hOCT3	88.7 ± 14.6	2.14 ± 0.25

Chapter 3. DEVELOPMENT AND VALIDATION OF A HPLC-MS/MS METHOD FOR *IN VIVO* QUANTIFICATION OF MIBG

This chapter is in submission for publication:

López Quiñones, A. J., Shireman, L. M., Wang, J. "Development and Validation of a HPLC/MS/MS method for *in vivo* Quantification of *meta*-Iodobenzylguanidine (mIBG)." *Journal of Chromatography B* (2021).

3.1 ABSTRACT

meta-iodobenzylguanidine (mIBG) is a radiopharmaceutical used for diagnosis and treatment of neuroendocrine cancers. A fast and simple bioanalytical method was developed for the quantification of non-radiolabeled mIBG in mouse plasma and tissue homogenates using high performance liquid chromatography-tandem mass spectrometry. Samples were prepared for analysis by extracting mIBG with a protein precipitation assay with acetonitrile, followed by drying with N_2 gas and a reconstitution step in a 96-well plate format. The method was validated based on selectivity, specificity, linearity, accuracy, precision, matrix effect, and recovery in mouse plasma and liver homogenates. The method was selective, specific, and exhibited linearity from 0.98 to 500 ng/mL of mIBG. The inter-day and intra-day precision deviations and accuracy were within 15% of the nominal concentrations. Additionally, no matrix effect or changes to the extraction recovery were observed in plasma and liver matrices. The proposed quantification method of non-radiolabeled mIBG allows for a safe, fast, and high-throughput analysis of mIBG concentrations to support preclinical studies in mice.

3.2 INTRODUCTION

Radioiodine-labeled *meta*-iodobenzylguanidine (mIBG) is used for diagnosis and targeted radiotherapy of neuroendocrine tumors. ^{131}I-labeled mIBG is approved by the US Food and Drug Administration (FDA) for the treatment of advanced pheochromocytoma and paraganglioma and is also being investigated in multiple clinical trials for the treatment of high-risk neuroblastoma (Parisi et al., 2016; Pryma et al., 2019). These cancers originate from the neural crest and exhibit high expression of the norepinephrine transporter (NET), a transmembrane protein involved in the transport of norepinephrine across cell membranes (Streby et al., 2015). As a structural analog of norepinephrine, ^{131}I-mIBG enters the tumor cells through the NET pathway, where radioactive decay of ^{131}I produces DNA damage, cell death, and tumor necrosis. Besides tumor cells, mIBG accumulates in several normal tissues (e.g. liver, salivary glands, heart), which can lead to tissue toxicity (Chin et al., 2014). Recently, we showed that mIBG is an excellent substrate for polyspecific organic cation transporters and these transporters could play important roles in mIBG tissue uptake and disposition *in vivo* (Bayer et al., 2009; López Quiñones et al., 2020). However, the *in vivo* involvement of these molecular mechanisms in the disposition and tissue uptake of mIBG has not been fully understood.

Previous analytical methods have relied on the use of radioactive iodine isotopes (^{123}I, ^{131}I) to quantify mIBG in biodistribution studies in preclinical species (Bayer et al., 2016; Kölby et al., 2003). Besides safety concerns of handling radioactive iodine, the radiolabeled form of mIBG is not readily available due to limited facilities that can synthesize the compound. Further, the short decay half-lives of ^{123}I and ^{131}I (13 hours and 8 days, respectively) also make the use of radiolabeled mIBG challenging due to the short shelf-life and need to correct analytical results for radioactive decay. Lastly, these methods quantify the radiation emitted by

the iodine radionuclide, and thus cannot differentiate between intact mIBG and the free iodide that can dissociate from mIBG in the body (Ehninger et al., 1987). To support preclinical pharmacokinetic and biodistribution studies of mIBG, a bioanalytical method that measures concentrations of intact, non-radiolabeled mIBG in biological matrices is needed. In the current study, the objective was to develop and validate a reliable and simple liquid chromatography-tandem mass spectrometry (LC-MS/MS) method to quantify non-radiolabeled mIBG in mouse plasma and liver homogenates.

3.3 METHODS

3.3.1 Chemicals and Animals

mIBG was purchased from Sigma Aldrich (St. Louis, MO). 4-hydroxyphenformin (4OHP) purchased from US (Mumbai, India). High-grade of acetonitrile, methanol, and formic acid were obtained from Thermo Fisher (Rockford, IL). Plasma and liver were collected from adult male and female FVB mice. The mice were housed in a specific pathogen-free facility and fed a standard diet. The mice were euthanized by CO_2 overdose, followed by cardiac puncture to collect whole blood using a heparinized needle and syringe. The blood was centrifuged at 2,000 *x g* for 10 mins and the plasma was collected. The liver was collected, snap-frozen, and stored at -80˚C. The liver samples were homogenized at a 1:5 ratio of liver weight to phosphate buffered saline volume with an Omni Bead Ruptor (Omni International, Kennesaw, GA). All animal studies were approved by the Institutional Animal Care and Use Committee of the University of Washington.

3.3.2 Instrument and LC-MS/MS Conditions

An Agilent 6410 Triple Quad mass spectrometer coupled to an Agilent 1290 series HPLC system (Agilent Technologies, Santa Clara, CA) operated in the positive electrospray ionization

mode was used for analysis. A Zorbax Eclipse Plus C18 column (2.1 x 50mm, 1.8 µm; Agilent Technologies, Santa Clara, CA) accompanied with a HPLC SecurityGuard guard column (Phenomenex, Torrance, CA) were used to separate mIBG and 4OHP. The column was maintained at room temperature and the autosampler at 4˚C. The mobile phases consisted of 0.1% (vol/vol) formic acid in water (A) and acetonitrile (B) with gradient elution at 0.4 mL/min flow as follows: 3% B until 0.1 min, increased to 90% B by 2 min and maintained at 90% B for 1 min. The composition was returned to 3% B over 0.1 min and held for 1.9 min for a total run time of 5 min. The mass-to-charge (*m/z*) transitions used for quantification of mIBG and 4OHP were 276.1 → 217.0 and 222.1 → 121, respectively. Instrument control and data processing were performed using Agilent MassHunter software (Agilent Technologies, Santa Clara, CA).

3.3.3 Stock and Working Solutions

Stock standard solutions were prepared in methanol at 5 mg/mL for mIBG and 1 mg/mL for 4OHP. Diluted "working" standard solutions were prepared in methanol with concentrations of 500 µg/mL for mIBG and 20 µg/mL for 4OHP. A protein-precipitation solution was prepared by a 2000-fold dilution of the working solution of 4OHP in acetonitrile.

3.3.4 Calibration Standards and Quality Control Samples

The calibration standards were prepared from the working solutions of mIBG. The highest calibration standard was prepared such that a 2 µL addition to 20 µL of blank plasma or liver homogenate resulted in a concentration of 500 ng/mL of mIBG. The remaining calibration standard solutions were prepared via 2-fold serial dilution. The lower limit of quantification (LLOQ) was defined as the lowest sample with sample-to-noise ratio (S/N) > 5 and accuracy and precision within 15% of the nominal concentration. The standard curve ranged from 0.98 to 500 ng/mL of mIBG, and the quality control samples for low (QC_{low}), mid (QC_{mid}), and high (QC_{high})

samples contained 2, 25, and 200 ng/mL of mIBG, respectively. A zero-calibration sample with only 4OHP and a double blank sample with neither mIBG nor 4OHP were also prepared.

3.3.5 Sample Preparation

Samples were prepared by a protein precipitation method. For each sample, an aliquot of 20 µL of blank plasma or liver homogenate was transferred to a 1.5 mL Eppendorf tube, followed by addition of 178 µL of the protein-precipitation solution. The samples were spiked with 2 µL of acetonitrile with or without mIBG. The samples were vortexed for approximately 5 seconds and centrifuged at 18,000 *x g* for 10 mins at 4˚C. A 100 µL aliquot of the organic supernatant was transferred to a 96-well plate, followed by evaporation under N_2 gas at 40˚C for approximately 20 mins. The samples were re-constituted with 200 µL of 10% acetonitrile in water and analyzed by LC-MS/MS.

3.3.6 Method Validation

Method validation was performed based on the bioanalytical method validation guidance from the FDA (Food and Drug Administration, 2018).

3.3.6.1 Specificity and Selectivity

Specificity was evaluated by analyzing the blank mouse plasma or tissue homogenate for interfering peaks. Selectivity was determined by comparing the signal in the blank mouse plasma or liver homogenate samples to the samples spiked mIBG at the LLOQ concentration.

3.3.6.2 Calibration Model and Linearity

The calibration standard curves described above were run independently four times with duplicate samples for each run. A linear equation with $1/x^2$ weighting was fit to the data using least-squares regression ($y=b_0 + b_1x$), where y is the mIBG to 4OHP peak area ratio (PAR), b_0 is the intercept, b_1 is the slope, and x is the nominal mIBG concentration in ng/mL. The runs were

considered acceptable when 80% of the calibration standards were within ± 15% of the nominal concentrations.

3.3.6.3 Accuracy and Precision

Accuracy was expressed as the deviation of the measured mean concentration from the nominal concentrations. The inter- and intra-day precision were calculated using a root mean squares approach based on the following analysis of variance (ANOVA) equations:

Equation 3.1: $$Intra-day\ precision = \frac{\sqrt{MS_{intra}}}{mean_{all}}\ x\ 100\%$$

Equation 3.2: $$Inter-day\ precision = \frac{\sqrt{(MS_{inter}-MS_{intra})/n}}{mean_{all}}\ x\ 100\%$$

where MS_{intra} and MS_{inter} are the mean squares within a group and between a group, respectively. $mean_{all}$ is the arithmetic mean of all the measured concentrations and n is the number of samples used for the tested concentration. Accuracy and precision of the QC samples were determined in six replicates conducted in four independent experiments. Accuracy and precision were considered acceptable if the values were within 15% of the nominal concentrations.

3.3.6.4 Matrix Effect and Recovery

Three types of samples were used to determine the matrix effect and recovery from mouse plasma and liver homogenates (prepared as described in Section 3.3.5). “Extracted” samples were defined as samples that were spiked with mIBG before adding the protein-precipitation solution to the blank plasma or liver homogenates. Similarly, “non-extracted” samples were samples that were spiked with mIBG after the protein-precipitation solution was added. Last, “neat” samples were prepared using 20 µL of acetonitrile instead of mouse plasma or liver homogenates. The matrix effect was determined by the ratio of the non-extracted samples to that of the neat samples. The extraction recovery was determined by the ratio of the

extracted samples to that of the non-extracted samples. Three independent experiments were run with three to six replicates for QC_{low}, QC_{mid}, and QC_{high} to capture the matrix effect and recovery.

3.4 RESULTS

3.4.1 Specificity and Selectivity

Representative chromatograms of blank and LLOQ-spiked plasma and liver homogenates are shown in **Figure 3.2**. The LLOQ was determined in both plasma and liver homogenates to be 0.98 ng/mL. A small interfering peak for mIBG was observed in some blank samples but was not consistently detected and was deemed negligible as the mean peak area was less than 20% of the LLOQ. The chromatograms showed that the method was selective and specific in both matrices with no expected interference to the quantification of mIBG.

3.4.2 Calibration Model and Linearity

A linear equation was fit to the data using a weighting factor of $1/x^2$ to describe the concentration and PAR relationship. The calibration curves were linear within the concentration range of 0.98-500 ng/mL of mIBG with correlation coefficients ranging from 0.9881-0.9978 and 0.9893-0.9972 for plasma and liver homogenates, respectively (**Figure 3.3**). The mean (± S.D.) for the regression parameters were $b_0 = 0.0086 \pm 0.0025$ and $b_1 = 0.0619 \pm 0.0176$ for plasma and $b_0 = 0.0188 \pm 0.0063$ and $b_1 = 0.0584 \pm 0.0201$ for liver homogenates. The back-calculated concentrations for plasma and liver matrices were accurate to within 5% and had coefficients of variation (CV) less than 10% for each of the standard concentrations, indicating a good fit to the data with the weighted linear regression (**Table 3.1**).

3.4.3 Accuracy and Precision

Accuracy and inter-day and intra-day precision were determined using the extracted samples from plasma and liver homogenates at three concentration levels. The method quantified the mIBG concentrations with accuracies ranging from 96% to 112% in both matrices (**Table 3.2**). Furthermore, the inter-day and intra-day precision values were within 15% for each mIBG concentration in both matrices, indicating that the method was accurate and precise in quantifying mIBG concentrations in plasma and liver homogenate.

3.4.4 Matrix Effect and Recovery

The matrix effect and extraction recovery were determined in plasma and liver homogenate at three concentration levels. The recovery for the extraction in all concentration levels ranged between 98-106% for plasma and 96-102% for liver homogenate (**Table 3.3**). The matrix effect at each tested concentration ranged between 96-100% for plasma and 95-106% for liver homogenate. These data suggest that the extraction method is reproducible, and the matrix from the plasma and liver homogenate has negligible effects on quantification of mIBG.

3.5 DISCUSSION

The proposed *in vivo* quantification method was adapted from an *in vitro* method developed to quantify mIBG from cell lysates (López Quiñones et al., 2020). In the *in vitro* quantification method, glyburide was used as an internal standard. The structure of glyburide is considerably different from mIBG which may prove problematic in complex matrices such as plasma and tissue homogenates. Thus, we developed an *in vivo* quantification method using 4OHP as an internal standard, which is structurally more similar to mIBG than glyburide (**Figure 3.1**). The chromatographic conditions were optimized to achieve distinguishable and sharp peaks for mIBG and 4OHP. The retention times were 1.9 and 1.6 mins for mIBG and 4OHP, respectively, in all

matrices with a total run time of 5 mins (**Figure 3.2**), allowing for rapid and efficient analysis of multiple samples.

Previously published methods for quantification of mIBG in preclinical species relied on counting the gamma radiation emitted by the radioactive iodine in mIBG (Bayer et al., 2016; Kölby et al., 2003). The proposed method provides multiple benefits compared to the use of radioactive mIBG for quantification. First, it completely eradicates the hazards of handling radioactive iodine. Second, it substantially reduces the cost and time constraints of using a radioactive isotope with a short half-life. Third, it eliminates the confounding effects of the radioactive decay half-life when analyzing concentration versus time data. Lastly, it directly quantifies mIBG rather than detecting the radiation emitted by the iodine, which may track free iodine dissociated from mIBG or potential metabolites. The quantification method also requires a relatively small volume of mouse plasma and liver homogenate in a one-step protein precipitation assay.

The validation for the *in vivo* quantification method of mIBG indicates that the method is reproducible, accurate, precise, and is applicable to both plasma and liver matrices. Given the 5 min run time and inexpensive sample preparation by protein precipitation, the proposed quantification method of non-radiolabeled mIBG allows for a safe, fast, and high-throughput analysis of mIBG concentrations in preclinical species.

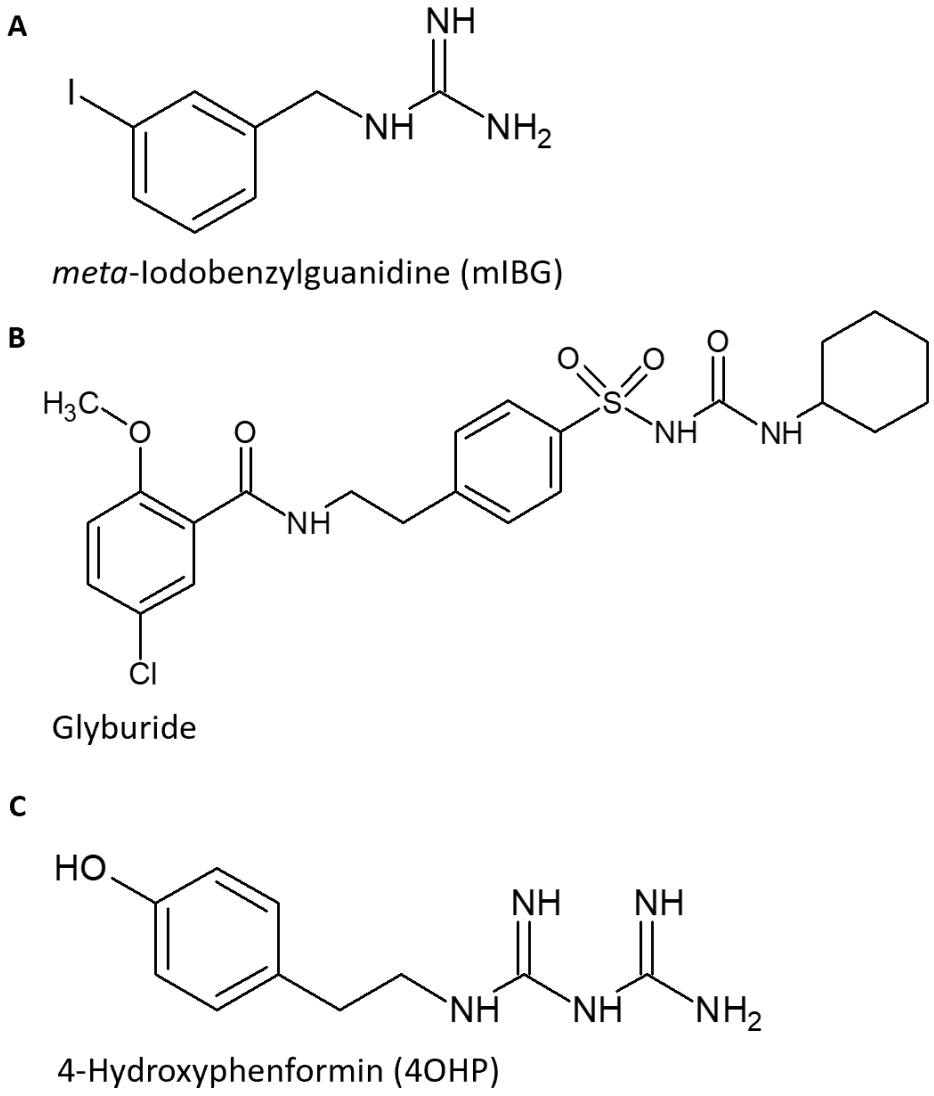

Figure 3.1. Chemical Structures of *meta*-iodobenzylguanidine (A), glyburide (B), and 4-hydroxyphenformin (C).

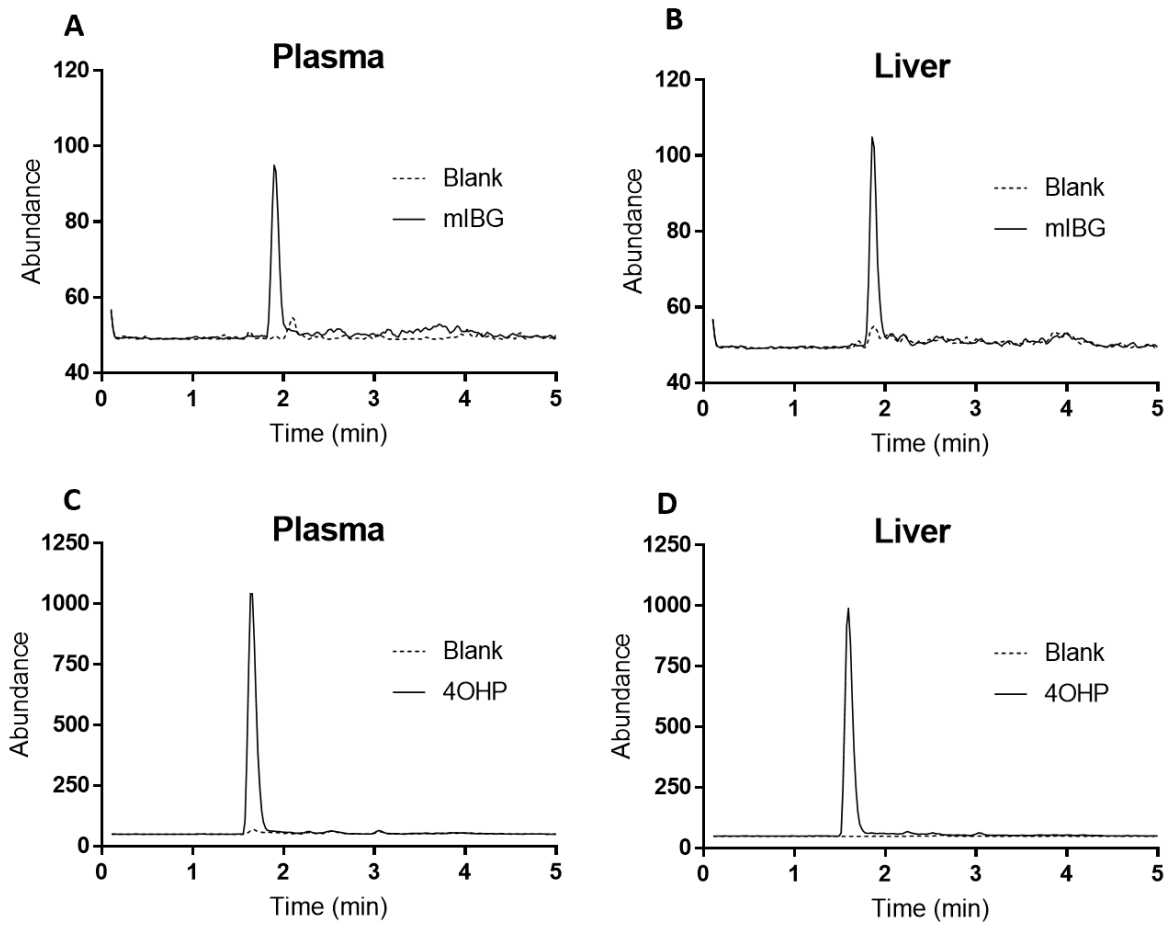

Figure 3.2. Representative chromatograms of mIBG and 4OHP in plasma and liver homogenates.

Chromatograms of blank and 0.98 ng/mL of mIBG spiked in plasma (A) and liver (B), and chromatograms of blank and 20 ng/mL of 4OHP in plasma (C) and liver (D).

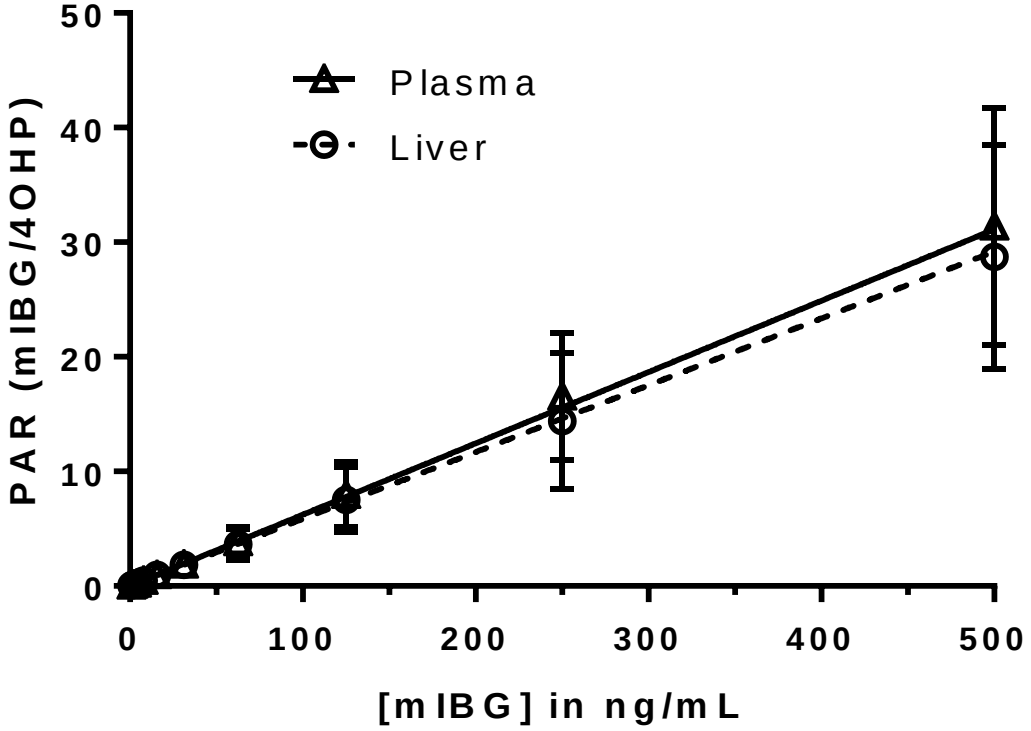

Figure 3.3. Calibration curves for mIBG in mouse plasma and liver homogenates.

Table 3.1. Back-calculated mIBG concentrations from calibrators in plasma and liver homogenates.

Concentration data are represented as mean ± standard deviation (S.D.). The calibrators were run in duplicates in independent experiments (n=4 for plasma and n=3 for liver).

mIBG Nominal Concentrations (ng/mL)	**Plasma**			**Liver**		
	Mean ± S.D. (ng/mL)	CV (%)	Accuracy (%)	Mean ± S.D. (ng/mL)	CV (%)	Accuracy (%)
0.98	0.98 ± 0.04	4	101	0.97 ± 0.04	4	100
1.95	2.0 ± 0.09	5	101	2.0 ± 0.1	6	102
3.91	3.9 ± 0.2	4	99	3.9 ± 0.2	4	99
7.81	7.6 ± 0.2	3	97	7.8 ± 0.4	6	100
15.6	16 ± 1.0	6	102	16 ± 0.7	4	105
31.3	31 ± 1	3	99	31 ± 2	5	99
62.5	62 ± 3	5	99	62 ± 2	3	98
125	128 ± 6	5	102	125 ± 4	3	100
250	260 ± 7	3	103	250 ± 20	7	99
500	500 ± 40	8	101	490 ± 40	9	98

Table 3.2. Intra- and inter-day precision and accuracy for mIBG in plasma and liver homogenates.

The $QC_{low,}$ QC_{mid}, and QC_{high} samples were run on four independent experiments (n=3 to 6).

Matrix	mIBG Nominal Concentration (ng/mL)	Intra-day Precision (%)	Inter-day Precision (%)	Accuracy (%)
Plasma	2	14.4	10.0	112
	25	8.4	6.4	105
	200	5.3	10.2	99
Liver	2	11.3	3.7	96
	25	7.2	9.8	99
	200	5.5	14.1	101

Table 3.3. Recovery and matrix effect for mIBG plasma and liver homogenates.

The $QC_{low,}$ QC_{mid}, and QC_{high} samples were run in four independent experiments (n=3 to 6).

Matrix	mIBG Nominal Concentration (ng/mL)	Recovery (%)	Matrix Effect (%)
Plasma	2	106 ± 7 (6%)	100 ± 10 (13%)
	25	104 ± 9 (8%)	96 ± 6 (6%)
	200	98 ± 3 (3%)	100 ± 4 (4%)
Liver	2	96 ± 7 (7%)	110 ± 10 (11%)
	25	100 ± 6 (6%)	95 ± 7 (7%)
	200	102 ± 2 (2%)	100 ± 10 (11%)

Chapter 4. CARDIAC TRANSPORT OF MIBG IS MEDIATED BY ORGANIC CATION TRANSPORTER 3

4.1 ABSTRACT

Radio-iodinated *meta*-iodobenzylguanidine is utilized as a diagnostic tool (^{123}I-mIBG) and as a targeted radiotherapy (^{131}I-mIBG) for neuroendocrine cancers. Additionally, ^{123}I-mIBG is used to image the sympathetically innervated heart. mIBG selectively accumulates in the cancer cells through uptake by the norepinephrine transporter. However, whole-body scintigraphy also shows extensive mIBG uptake and accumulation in several normal tissues (e.g. heart, salivary glands, liver, lungs) via mechanisms that are not fully understood. The accumulation of radioactive ^{131}I- mIBG in these tissues is associated with a range of adverse reactions and tissue damages due to the untargeted radiation exposure. We hypothesized that the efficacy and safety of ^{131}I-mIBG can be improved by selectively inhibiting mIBG uptake in healthy tissues without affecting its uptake in tumor cells. The goals of these studies were to confirm transport of mIBG by mouse Oct3 (mOct3) and to elucidate the impact of organic cation transporter 3 (OCT3) on the *in vivo* pharmacokinetics and tissue distribution of mIBG using an Oct3 knockout mouse model. We conducted *in vitro* studies in HEK293 cell lines stably transfected with *mOct3* that revealed similar apparent affinities in the uptake of mIBG by hOCT3 and mOct3 (K_m of 14.5 ± 7.1 and 29.4 ± 3.4 μM, respectively), suggesting minimal species difference in mIBG transport by OCT3. For the *in vivo* pharmacokinetic study, wild-type and Oct3 knockout mice were administered 10 mg/kg of mIBG by retro-orbital injection. Full concentration-time profiles over 24 hours were used to calculate the plasma pharmacokinetics and tissue exposure to mIBG. mIBG exhibited extensive accumulation in multiple tissues with exposures ranging from 4 to 90-fold higher than the plasma AUC in *Oct3*$^{+/+}$ mice. In contrast, deletion of *Oct3* significantly reduced mIBG exposure in the heart by approximately 83% (p-value < 0.001). The exposure of mIBG in the skeletal muscle, salivary glands, and the lungs were also significantly reduced in *Oct3*$^{-/-}$ mice, demonstrating an

important role of *Oct3* in mediating uptake and accumulation of mIBG in healthy tissues. On the other hand, the systemic AUC and other pharmacokinetic parameters were similar between the *Oct3*$^{+/+}$ and *Oct3*$^{-/-}$ mice. In summary, we demonstrated that OCT3 transport mediates heart uptake of mIBG and knockout of Oct3 leads to decreased mIBG tissue uptake and accumulation. Furthermore, these findings support inhibition of OCT3 as a viable clinical strategy to reduce ^{131}I-mIBG accumulation and toxicity in healthy tissues in cancer patients undergoing radiotherapy.

4.2 INTRODUCTION

meta-Iodobenzylguanidine (mIBG) is a radiopharmaceutical used for neuroendocrine cancers as a diagnostic imaging agent and as a targeted radiotherapy. Similar to norepinephrine, mIBG is actively transported by the sodium-dependent norepinephrine transporter (NET) into the adrenal chromaffin cells and pre-synaptic terminals. Neuroendocrine cancers, such as neuroblastoma and pheochromocytoma, originate from the sympathoadrenal lineage and exhibit high expression of NET (Lenders et al., 2005; Maris et al., 2007). By selectively accumulating in the neuroendocrine tumor cells, mIBG delivers the radiation emitted by the iodine-123 within the tumor lesions for visualization and to track the disease progression. Patients that exhibit mIBG positive tumors may benefit from using ^{131}I-mIBG as a targeted radiotherapy. ^{131}I-mIBG is approved by the US Food and Drug Administration (FDA) for the treatment of advanced pheochromocytoma and paraganglioma and is currently being investigated in multiple clinical trials for the treatment of high-risk neuroblastoma (Parisi et al., 2016; Pryma et al., 2019). In addition to neuroendocrine cancers, ^{123}I-mIBG has seen broad clinical applications as an imaging agent of the sympathetically innervated heart by detecting alterations to the heart accumulation of mIBG. The reduction of ^{123}I-mIBG accumulation in the heart is used in determining disease prognosis in patients with heart failure, decision-making for heart medication selection, and as a diagnostic tool for cardiovascular and neurodegenerative diseases (Nakajima et al., 2018; Verberne et al., 2009).

Beside its selective uptake into the neuroendocrine tumor cells by NET, mIBG exhibits extensive accumulation in several normal tissues, such as in the heart, salivary glands, and liver (Chin et al., 2014; Coleman et al., 2009). The uptake into normal tissues may interfere with ^{123}I-mIBG scintigraphic imaging and can lead to tissue toxicities during ^{131}I-mIBG therapy (Bleeker

et al., 2013; Vik et al., 2009). Patients require continuous and automated blood pressure monitoring during ^{131}I-mIBG infusions and may present with severe cardiovascular adverse effects, such as tachycardia and hypertension (Parisi et al., 2016). In addition to cardiac toxicities, patients given ^{131}I-mIBG therapy frequently develop painful sialadenitis due to radiation injury to the salivary glands (Modak et al., 2008). To improve the clinical use of mIBG, a major goal is to increase the tumor-specific uptake of mIBG while reducing uptake into normal tissues. However, the molecular mechanisms involved in the tissue distribution of mIBG are not fully understood.

We previously showed that mIBG is efficiently transported by organic cation transporter 1-3 (OCT1-3) and multi-drug and toxin extrusion proteins 1 and 2-K (MATE1/2-K) with comparable transport kinetics to NET (López Quiñones et al., 2020). OCT1 is predominantly expressed in the liver and has been implicated in the hepatic mIBG accumulation (Giacomini et al., 2010; Jonker et al., 2001). About 90% of mIBG is renally eliminated and we showed that OCT2 and MATE1/2-K in the renal proximal tubular cells contribute to the renal secretion of mIBG (Blake et al., 1989; López Quiñones et al., 2020). OCT3, also known as the extra-neuronal monoamine transporter (EMT), is more widely distributed throughout the body relative to the other isoforms, with high expression in the salivary glands, heart, and the skeletal muscle (Lee et al., 2014; Wagner et al., 2016). Using a mouse model with targeted gene deletion of *Oct3* (*Slc22a3)*, our laboratory first demonstrated that OCT3 plays a critical role in the tissue distribution of metformin and *para*-hydroxymethamphetamine in salivary glands and heart *in vivo* (Lee et al., 2014; Wagner et al., 2018). In addition, OCT3 was recently reported as the main transporter mediating doxorubicin accumulation in the heart and that selectively targeting OCT3 can attenuate doxorubicin-induced cardiotoxicity in mice (Huang et al., 2021). Since the OCTs

are not expressed in neuroendocrine tumors, OCTs may be selectively inhibited to reduce mIBG accumulation and radiation exposure in healthy tissues (Dubois et al., 2012). Based on these observations, we hypothesize that OCT3 mediates the physiological tissue distribution of mIBG and contributes to the efficacy and toxicities of radio-iodinated mIBG.

The goal of this study was to investigate the role of OCT3 in the physiological tissue distribution and accumulation of mIBG *in vivo*. We determined the uptake kinetics of mIBG by mOct3 and its pharmacokinetics and tissue distribution in mice. The impact of OCT3 in the tissue distribution of mIBG was investigated using an Oct3 knockout mouse model.

4.3 METHODS

4.3.1 Materials.

meta-Iodobenzylguanidine (mIBG) was purchased from Sigma Aldrich (St. Louis, MO) and 4-hydroxyphenformin (4OHP) was purchased from USV (Mumbai, India). [^{3}H]methyl-4-phenylpyridinium (MPP+, 80 Ci/mmol) was purchased from American Radiolabeled Chemicals, Inc. (St. Louis, MO). High-grade acetonitrile, methanol, and formic acid were obtained from Thermo Fisher (Rockford, IL). Cell culture media and reagents were purchased from Invitrogen (Carlsbad, CA).

4.3.2 Animals.

The *Oct3* (*Slc22a3*) null mice, referred to as *Oct3*$^{-/-}$ mice, were originally developed from the FVB inbred strain by Dr. Denise Barlow (Zwart *et al.*, 2001) and maintained by Dr. Alfred Schinkel (Netherlands Cancer Institute). Breeding pairs of *Oct3*$^{+/+}$ and *Oct3*$^{-/-}$ mice were generously provided to us by Dr. John Markowitz (University of Florida) with approval from Dr. Schinkel. Mice were housed in specific pathogen-free facilities at the University of Washington

with a 14/10-h light/dark cycle and a standard diet. All animal studies were approved by the Institutional Animal Care and Use Committee of the University of Washington.

4.3.3 Uptake Experiments.

Flp-In human embryonic kidney (HEK) 293 cells stably transfected with mOct3 and the empty pcDNA5/FRT vector (control) were previously generated in our laboratory (Lee et al., 2014). The cells were maintained in a 37°C incubator set at 5% CO_2 with Dulbecco's modified Eagle's medium (DMEM) supplemented with 10% fetal bovine serum, 2mM L-glutamine, 100 U/mL penicillin, 100 µg/mL streptomycin, and 150 µg/mL hygromycin B. The surface of the flasks was coated with 0.01% poly-D-lysine in phosphate-buffered saline to promote HEK293 cell attachment. The uptake assays were conducted as previously described (López Quiñones et al., 2020). The cells were seeded on 96-well plates and grown to greater than 90% confluency. Cells were washed with warm Hank's balanced salt solution (HBSS) buffer (1.3 mM $CaCl_2$, 0.4 mM KH_2PO_4, 0.8 mM $MgSO_4$, 0.3 mM Na_2HPO_4, 5.4 mM KCl, 137 mM NaCl, 4.2 mM $NaHCO_3$, and 5.6 mM D-glucose) three times. Uptake experiments were initiated by addition of 100 µL of HBSS containing mIBG at various concentrations. Uptake was quenched by removing the warm HBSS with mIBG and subsequently washing the cells three times with 200 µL ice-cold HBSS. After washing, cells were lysed with 200 µL acetonitrile containing 4OHP as an internal standard. Twenty microliters of lysate were diluted in water to 10% acetonitrile for mIBG quantification by LC-MS/MS analysis. The activity of mOct3 was verified with ^{3}H-MPP+ (data not shown). The cells in these reference experiments were lysed with 100 µL 1 M NaOH and neutralized with 100 µL 1M HCl after one hour. At the end of the uptake experiment, 150 µL was taken from the cell lysate for analysis of the total radioactivity using a Tri-Carb Liquid Scintillation Counter (Perkin Elmer, Waltham, MA). Twenty microliters of the lysate were taken

from the reference cell lysates to estimate the total protein concentration using the BCA method. Variation in total protein concentration was less than 10%. The uptake studies were performed in triplicate and repeated three times independently. The Michaelis-Menten equation was fit to the data by non-linear regression using GraphPad Prism 7.0 (GraphPad Software Inc., La Jolla, CA) to obtain kinetic parameters:

Equation 4.1: $$v = \frac{V_{max} * [S]}{K_m + [S]}$$

where v is the uptake velocity, V_{max} is the maximum uptake velocity of the system, K_m is the Michaelis-Menten constant, and [S] is the substrate concentration.

4.3.4 In vivo Pharmacokinetics Studies.

The *in vivo* pharmacokinetic study was carried out in male FVB mice 4 to 6 months old. Male mice were used as the observed pharmacokinetics and tissue distribution of other organic cations, such as metformin, MPP+, and methamphetamine, were similar between male and female mice (Lee et al., 2014; Zhu et al., 2010; Zwart et al., 2001). Mice were administered 10 mg/kg of mIBG intravenously by retro-orbital injection under isoflurane anesthesia. Mice (n=3 at each time point) were sacrificed by CO_2 overdose, followed by cardiac puncture with a heparinized syringe at various time points (5 mins, 0.5, 1, 2, 4, 8, and 24 hrs). Blood was centrifuged at 2,000 *x g* for 10 mins at 4˚C and the plasma was collected. The tissues (salivary glands, thyroid, adrenal glands, kidney, spleen, liver, heart, lung, and skeletal muscle) were collected, snap-frozen, and stored at -80˚C. The tissue samples were homogenized at a 1:4 (kidney), 1:5 (salivary glands, spleen, liver, lung, and skeletal muscle), 1:6 (heart), and 1:11 (thyroid and adrenal glands) ratio of tissue weight to phosphate buffered saline (PBS) volume with an Omni Bead Ruptor (Omni International, Kennesaw, GA). mIBG was extracted from 20 µL of plasma or tissue homogenates with a protein precipitation method using acetonitrile containing 50 ng/mL of 4OHP. The samples were vortexed

for approximately 5 seconds and centrifuged at 18,000 *x g* for 10 mins at 4˚C. A 100 µL aliquot of the supernatant was transferred to a 96-well plate, followed by evaporation under N_2 gas at 40˚C for approximately 20 mins. The samples were re-constituted with 200 µL of 10% acetonitrile in water and analyzed by LC-MS/MS.

4.3.5 LC-MS/MS Analysis of mIBG

An Agilent 6410 Triple Quad mass spectrometer coupled to an Agilent 1290 series HPLC system (Agilent Technologies, Santa Clara, CA) operated in the positive electrospray ionization mode was used for analysis. A Zorbax Eclipse Plus C18 column (2.1 x 50mm, 1.8 µm; Agilent Technologies, Santa Clara, CA) accompanied with a SecurityGuard guard column (Phenomenex, Torrance, CA) were used to separate mIBG and 4OHP as described in Section 3.3.2. Briefly, the mobile phases consisted of 0.1% (vol/vol) formic acid in water (A) and pure acetonitrile (B) with gradient elution at 0.4 mL/min flow as follows: 3% B until 0.1 min, increased to 90% B by 2 min and maintained at 90% B for 1 min. The composition returned to 3% B over 0.1 min and held for 1.9 min for a total run time of 5 min. The mass-to-charge (*m/z*) transitions used for quantifying mIBG and 4OHP were 276.1 → 217.0 and 222.1 → 121.0, respectively. Data processing were performed using Agilent MassHunter software (Agilent Technologies, Santa Clara, CA). Accuracy and precision for the assay were within 15% for each batch.

4.3.6 Pharmacokinetic data analysis

The pharmacokinetic parameters were estimated from the concentration-time profiles obtained in plasma and tissue homogenates. Since mIBG concentrations were sampled in different animals at each time point, a population-based bootstrap method was used to estimate the pharmacokinetic parameters as previously described (Lee et al., 2014; Mager and Goller, 1998; Wagner et al., 2018). The measured plasma and tissues concentrations of each animal were

resampled 10,000 times to generate pseudo concentration-time profiles and obtain the mean and 95% confidence interval of each pharmacokinetic parameter using the R program (Jaki and Wolfsegger, 2011). The area under concentration-time curve (AUC), clearance (CL), terminal half-life ($t_{1/2,\beta}$), and volume of distribution at steady state (V_{ss}) were calculated by non-compartmental analysis using the following equations:

Equation 4.2: $$AUC_{0-t} = \int_0^t C(t)dt$$

Equation 4.3: $$AUC_{0-\infty} = AUC_{0-t} + {C(t)}/{\beta}$$

Equation 4.4: $$CL = {dose}/{AUC_{0-\infty}}$$

Equation 4.5: $$t_{\frac{1}{2},\beta} = {\ln(2)}/{\beta}$$

Equation 4.6: $$V_{ss} = {dose * AUMC}/{AUC^2}$$

The AUC and area under the moment curve (AUMC) were calculated using the linear trapezoidal rule. The terminal slope (β) was estimated by linear regression of the last three or four time points of the log(concentration)-time profiles. Two-sided *p* values were calculated using permutation tests with 10,000 replications and corrected for multiple comparisons using the Bonferroni method (Wagner et al., 2018; Westfall and Young, 1993). A *p* value of less than 0.05 was considered statistically significant.

4.4 RESULTS

4.4.1 Uptake of mIBG by mOct3.

We previously demonstrated that mIBG is efficiently transported by human OCT3 (hOCT3) (López Quiñones et al., 2020). To confirm that mOct3 transports mIBG, we investigated the uptake of mIBG in HEK293 cells stably transfected with mOct3. mIBG uptake was much higher in mOct3 expressing cells than vector cells and displayed typical Michaelis-

Menten saturation curves (**Figure 4.1**). The apparent affinity (K_m = 29.4 ± 3.4 µM) and the maximum transport rate (V_{max} = 8.60 ± 0.32 nmol/mg protein/min) for mIBG uptake by mOct3 were comparable to those of hOCT3 (K_m = 14.5 ± 7.1 µM and V_{max} = 3.14 ± 0.48 nmol/mg protein/min) (López Quiñones et al., 2020).

4.4.2 Biodistribution of mIBG in Oct3+/+ mice.

The concentration of mIBG was determined in plasma and selected tissues in *Oct3*$^{+/+}$ mice as shown in **Figure 4.2**. For simplicity, the 5 mins, 0.5, 4, and 24 hr time points were shown. The tissues from three mice at each time point were homogenized and concentrations of mIBG were observed in the plasma and all tested tissues within the first 5 mins after IV dosing. Assuming a tissue density of 1 g/mL, the tissue concentrations were consistently higher than the plasma at 5 mins, except for the skeletal muscle. The concentrations of mIBG in the kidney (10,500 ng/g of mIBG) were remarkably higher than any other tissue (146 to 2,580 ng/g of mIBG) and were dramatically decreased at 30 mins. mIBG remained at high and steady levels at 30 mins in the heart, salivary glands, liver, and adrenal glands. At 30 mins, all tissues were consistently higher than the plasma concentrations. Except for the adrenal glands, the concentrations of mIBG continued to decrease in the plasma and most tissues for the following 24 hours. The accumulation and longer retention of mIBG in the adrenal glands was expected and is in line with the scintigraphic images in murine and humans (Kölby et al., 2003; Nakajo et al., 1983). Of note, mIBG was quantifiable in the thyroid for up to 24 hours with comparable concentrations to the other tissues, suggesting that intact mIBG distributed into the thyroid.

4.4.3 Plasma pharmacokinetics in Oct3+/+ and Oct3-/- mice.

To determine the importance of Oct3 in the disposition and tissue distribution of mIBG, we compared the plasma and tissue concentrations in *Oct3*$^{+/+}$ and *Oct3*$^{-/-}$ mice after intravenous

administration of 10 mg/kg of mIBG. The linear and log-transformed concentration-time profiles of mIBG in the plasma of *Oct3*$^{+/+}$ and *Oct3*$^{-/-}$ mice are shown in **Figure 4.3**. In both groups of mice, mIBG exhibited biphasic kinetics with a rapid decrease in concentrations within the first 30 mins followed by a slower terminal phase. The plasma clearance, exposure (AUC), half-life, and volume of distribution for mIBG in *Oct3*$^{+/+}$ and *Oct3*$^{-/-}$ mice were comparable (*p* value > 0.05) (**Table 4.1**). In addition, the observed plasma concentrations of mIBG (0.006-2 µM) did not saturate OCTs, MATEs, or NET as the K_m value was much greater than the concentrations (López Quiñones et al., 2020). These data indicate that deletion of *Oct3* does not have an impact on the pharmacokinetics of mIBG after IV administration.

4.4.4 Impact of Oct3 deletion on mIBG accumulation in the heart

The concentration-time profiles of mIBG in the heart were compared to the respective plasma concentration-time profiles and between *Oct3*$^{+/+}$ and *Oct3*$^{-/-}$ mice (**Figure 4.4**). In the *Oct3*$^{+/+}$ mice, mIBG was rapidly concentrated in the heart and reached a plateau for the first hour after IV administration (**Figure 4.4A**). The heart-to-plasma ratios at all time points in the *Oct3*$^{+/+}$ mice were much greater than 1, implying accumulation of mIBG in the heart (**Figure 4.4D**). Deletion of *Oct3* caused the heart concentration-time profile of mIBG to resemble that of its plasma profile with approximately 3-fold higher concentrations in the heart (**Figure 4.4B**). The pronounced mIBG accumulation in the heart and the early plateau that was present in the *Oct3*$^{+/+}$ mice was abrogated with deletion of *Oct3* (**Figure 4.4C**). The heart concentrations of mIBG in the *Oct3*$^{-/-}$ mice were 65-93% lower than those found in the *Oct3*$^{+/+}$ mice at all time points with an 83% reduction in mIBG overall exposure to the heart (**Table 4.2**). Loss of *Oct3* resulted in heart-to-plasma ratios between 2-7, suggesting there was little contribution of other mechanisms

of mIBG transport in the heart of mice. These data strongly suggest that majority of mIBG is actively accumulated into the heart from the blood by Oct3.

4.4.5 Impact of Oct3 deletion on tissue exposures of mIBG

The contribution of Oct3 to the tissue distribution of mIBG was performed by comparing tissue-specific exposure of mIBG, calculated as the $AUC_{0\text{-}24\ hrs}$, between *Oct3*$^{+/+}$ and *Oct3*$^{-/-}$ mice. The mIBG tissue exposures were consistently higher than the mIBG plasma exposure (**Table 4.1** and **Table 4.2**). The adrenal glands which showed no apparent decrease in mIBG concentrations within 24 hours, had the highest exposure in both groups of mice (**Table 4.2**). The heart and salivary glands also showed very high mIBG exposures. In *Oct3*$^{-/-}$ mice, mIBG was reduced by 83% and 67% for the heart and the skeletal muscle, respectively, and the salivary glands and the lung exhibited a moderate reduction (31~36%) in mIBG exposure. A moderate decrease in mIBG exposure was observed for the thyroid but did not reach statistical significance. No change in mIBG exposure between the genotypes was observed for the spleen, adrenal glands, liver, and the kidney.

4.5 DISCUSSION

Although most drugs exert pharmacological effect in tissues rather than the plasma, the concentrations of drugs in tissues are typically unknown for humans. In the case of radio-iodinated mIBG, the scintigraphic images allow for visualization of its physiological tissue distribution and estimation of the radiation exposure to each tissue (Chin et al., 2014; Coleman et al., 2009). In ^{131}I-mIBG therapy for neuroendocrine cancers, several severe tissue-specific adverse effects have been observed, such as hypertension, hypothyroidism, and sialadenitis (Modak et al., 2008; Parisi et al., 2016). In ^{123}I-mIBG cardiac imaging, alterations to the normal physiological accumulation of mIBG in the heart has shown promising results for diagnosis of

cardiovascular and neurodegenerative diseases, prognosis in heart failure patients, and for decision-making and management of heart-related therapies (Gebhard, 2018). Although there is an abundance of tissue distribution data for mIBG, little is known regarding the molecular mechanisms underlying the transport and accumulation of mIBG in normal, healthy tissues. In this study, we sought out to determine the impact of OCT3 on the pharmacokinetics and tissue distribution of mIBG. We demonstrated that although Oct3 does not alter the plasma pharmacokinetics of mIBG, the transporter plays a critical role in mediating the uptake and accumulation of mIBG in the heart, skeletal muscle, salivary glands, and lungs. To our knowledge, this is the first time that OCT3 has been described as a major transporter involved in the accumulation of mIBG in the heart.

Our data showed that the mouse ortholog of Oct3 efficiently transports mIBG with comparable kinetics to hOCT3 (**Figure 4.1**). Consistent with this finding, we previously showed that transport of metformin and methamphetamine and its metabolites by mouse and human OCT3 exhibited minimal species-differences (Lee et al., 2014; Wagner et al., 2018). Similarly, the human, mouse, and rat orthologs of OCT1 showed little species difference in the transport of several substrates of the OCTs (Floerl et al., 2020). Although mice eliminate mIBG more rapidly than humans, the tissue distribution observed in the *Oct3*$^{+/+}$ mice was in agreement with the biodistribution pattern in other rodent species and in humans with high accumulation in the salivary glands, adrenal glands, and the heart (**Figure 4.2**) (Barrett et al., 2010; Chin et al., 2014; Kölby et al., 2003). In addition, the lack of species-difference in the transport of mIBG by OCT3 suggests the data from this study can be translated to humans. Furthermore, deletion of Oct3 had no effect on the plasma pharmacokinetics of mIBG (**Figure 4.3** and **Table 4.1**). This is consistent with the minimal expression of OCT3 in the kidney and liver, the major organs for

systemic elimination of drugs. Our findings are consistent with previous studies which show a key role of OCT3 in the peripheral tissue uptake of other organic cations *in vivo* (Huang et al., 2021; Wagner et al., 2018; Zwart et al., 2001).

In the heart, mIBG quickly crosses the capillary endothelium and is distributed into neuronal and extra-neuronal cells in the heart. **Figure 4.5** shows a summary of the proposed mechanisms in which OCT3 may mediate mIBG uptake and accumulation in the heart. Similar to norepinephrine, mIBG is actively taken up into the neurons by NET and is concentrated by the vesicular monoamine transporters (VMATs) in the storage vesicles (Kölby et al., 2003). In contrast, the extra-neuronal uptake of catecholamines is thought to be mediated by OCTs, particularly OCT3 as it has a wide tissue and cell-type distribution (Eisenhofer, 2001). In the heart, OCT3 is highly expressed in cardiomyocytes and vascular endothelial cells (Grube et al., 2011; Huang et al., 2021; Solbach et al., 2011). In addition, neuronal expression of OCT3 has been detected in the brain of rats (Gasser et al., 2017). Although non-neuronal uptake of mIBG is thought to play a lesser role than neuronal uptake in humans, most of the data have relied on specific inhibitors of NET, such as desipramine, and pan-inhibitors of non-NET transport mechanisms, which may not have sufficiently inhibited OCT3 to cause visible changes in the heart accumulation (Dae et al., 1992; Sisson et al., 1987). As such, previous studies may not have captured the importance of OCT3 on cardiac accumulation of mIBG.

Our data showed that approximately 83% of mIBG exposure in the heart was mediated by mOct3 (**Figure 4.4** and **Table 4.2**). Consistent with reduced mIBG uptake in the heart, other organic cations, such as MPP+ and metformin, showed reduced heart uptake in *Oct3*$^{-/-}$ mice (Lee et al., 2014; Zwart et al., 2001). Cardiomyocytes have high expression of OCT3 (Grube et al., 2011; Solbach et al., 2011) and may play a significant role in the cardiac accumulation of mIBG

and other organic cations, such as metformin, in rodent species and in humans. Furthermore, the well-established doxorubicin-induced cardiotoxicity was recently shown to be initiated by OCT3 transport in cardiomyocytes (Huang et al., 2021). Alteration to cardiomyocyte function, such as by myocardial ischemia, resulted in a reduction in catecholamines in the myocardium and depletion of adrenergic innervation in the infarcted region (Schomig et al., 1984). In addition, polymorphisms of OCT3 were associated with reduced risk for coronary artery disease in a male Chinese Han population (Zhao et al., 2017). These data suggest that OCT3 function may be altered in disease states and may impact the prognostic value and use of ^{123}I-mIBG scintigraphic imaging.

OCT3 may also play a role in the transport of mIBG across the endothelial cells lining the heart capillaries. Previous experiments have shown conflicting data for the potential role of the trans-endothelial transport of catecholamines and mIBG (Cousineau et al., 1980; Dae et al., 1992; Degrado et al., 1995; Lameris et al., 1999). The expression of OCT3 on the capillary endothelial cells (Grube et al., 2011; Solbach et al., 2011) suggest that mIBG may accumulate in the capillary endothelial cells or may be efficiently transported across the capillary endothelial cells. However, the functionality of OCT3 in the capillary endothelial cells has not been explored and it is not known whether mIBG accumulates in the endothelial cells. The efflux of mIBG out of the capillary endothelial cells and cardiomyocytes may be mediated by MATE1 (Hiasa et al., 2006) or the multidrug resistance associated protein 1 and 4 (MRP1/4) (Kobayashi et al., 2020; Sassi et al., 2012). The involvement of MATE1 and the MRPs in the cardiac distribution of mIBG are currently unknown and is beyond the scope of this study. Nonetheless, localization and functional studies with MATE1 and MRP1/4 inhibitors and knockout mice models may provide a clearer picture about the retention and efflux of mIBG in the extra-neuronal

compartments. Similarly, the contribution of both OCT3 and NET in heart accumulation warrants further studies in humans.

Muscle accumulation of mIBG is often used as a reference tissue to analyze ^{123}I-mIBG scintigraphic images (Kitamura et al., 2021; Kobayashi et al., 2020; Watanabe et al., 2010). Although accumulation of mIBG is low in the muscle, the signal is homogenous throughout the muscle and is higher than the background signal (Kitamura et al., 2021). Consistent with the imaging data in humans, our data revealed low accumulation of mIBG in the mouse skeletal muscle (**Table 4.2**). Most importantly, with deletion of Oct3, a 67% reduction in mIBG exposure in the skeletal muscle was observed. This finding is consistent with metformin and *para*-hydroxymethamphetamine that also exhibited decreased muscle accumulation in Oct3 knockout mice (Lee et al., 2014; Wagner et al., 2018). These data suggest that OCT3 is a major determinant of transport of mIBG and other organic cations in the skeletal muscle.

Our data also demonstrates that OCT3 contributes to the accumulation of mIBG in the salivary glands (**Table 4.2**). Deletion of Oct3 caused a moderate reduction in exposure, indicating that OCT3 partially contributes to mIBG uptake in salivary glands. We previously showed expression of OCT3 and NET in the submandibular, parotid, and sublingual salivary glands (Lee et al., 2014). In pheochromocytoma patients undergoing visualization of the salivary glands with ^{131}I-mIBG, dosing with 40-75 mg/day of imipramine reduced accumulation of mIBG in the salivary gland (Nakajo et al., 1984). Withdrawal of imipramine restored accumulation of mIBG in the salivary glands of the same patients, suggesting that active uptake of mIBG into the salivary glands is inhibitable with imipramine. The plasma concentrations of imipramine at the given dose are expected to be in the low nanomolar range (Nagy and Johansson, 1975) that may inhibit NET but not OCT3. These data suggest that both OCT3 and NET mediate mIBG

accumulation in the salivary gland. In the context of neuroendocrine cancers, inhibition of NET can reduce tumor uptake of mIBG and thus may lead to reduced efficacy of ^{131}I-mIBG therapy. Conversely, inhibition of OCT3 can decrease accumulation of mIBG in the salivary glands while not altering the tumor uptake. Similar to the salivary glands, our data revealed a moderate contribution of OCT3 to the mIBG exposure in the lung (**Table 4.2**). The pulmonary circulation is involved in the regulation of the vasoactive catecholamines (Bousvaros, 1962). The OCTs and NET have been shown to be expressed throughout the lung, suggesting that transport of mIBG may be mediated by multiple transporters in this tissue (Ingoglia et al., 2015; Lips et al., 2005; Tseng and Padbury, 1998).

Our data showed that mIBG was distributed into the thyroid at comparable concentrations to the other tissues (**Figure 4.2** and **Table 4.2**). Free iodine from ^{131}I-mIBG synthesis and/or de-iodination by the liver is believed to be taken up by the thyroid and can lead to radiation damage (Quach et al., 2011). To minimize thyroid uptake, patients are typically administered potassium iodide prior to ^{131}I-mIBG therapy to saturate the thyroid (Parisi et al., 2016). Despite the use of thyroid blockage, patients still present with primary hypothyroidism in approximately 15-64% of cases (Friedman et al., 2014; Van Santen et al., 2002). Our data indicate that intact mIBG can contribute to the radiation exposure in the thyroid. Although a partial decrease in mIBG exposure was noted with deletion of *Oct3*, the reduction was not statistically significant, suggesting there are other mechanisms of transport involved in thyroid uptake of mIBG. A comprehensive analysis of putative mIBG transporters in thyroid tissues may help to identify the transporter involved in mIBG uptake and toxicity in this tissue.

OCT3 as a mediator of mIBG transport in the heart and other normal tissues has several clinical implications. Recently, OCT3 was shown to mediate the accumulation of doxorubicin in

the heart of mice and humans (Huang et al., 2021). Concomitant administration with nilotinib, a tyrosine kinase inhibitor (TKI) that potently inhibits OCT3, alleviated the doxorubicin-induced cardiomyocyte toxicities (Huang et al., 2021). Similarly, we previously showed that crizotinib, a TKI under investigation as treatment for neuroblastoma, preferentially inhibited mIBG uptake by hOCT3 relative to hOCT1 and hOCT2 (López Quiñones et al., 2020). Inhibiting OCT3-mediated uptake of mIBG may prevent its accumulation in the heart and reduce radiation-associated cardiac toxicities.

Moreover, patients undergoing ^{123}I-mIBG scans for diagnosis or to track disease progression may have deleterious drug-drug interactions (DDIs) that could confound the results. Drug interactions with mIBG have been focused on its NET-mediated transport (Stefanelli et al., 2013). A systematic review of the effect of heart medications on mIBG uptake emphasized a lack of information on the effect of known OCT3 inhibitors on mIBG uptake (Jacobson and Travin, 2015). In addition, unlike OCT1 and OCT2, the FDA does not suggest screening OCT3 for new drugs in development (Food and Drug Administration, 2020). Since changes to the OCT3-mediated tissue uptake are not reflected in plasma pharmacokinetics, ^{123}I-mIBG may be a useful imaging tool as an *in vivo* probe to gauge at tissue specific interactions of OCT3, particularly those pertaining to the heart.

In summary, we demonstrated that OCT3 is the main transporter responsible for the distribution of mIBG in the heart. Deletion of Oct3 also reduced the distribution of mIBG to the skeletal muscle, salivary glands, and lungs while not affecting the plasma pharmacokinetics. Our data suggests that targeting OCT3 can substantially reduce the accumulation of mIBG in sensitive tissues and may lead to reduced tissue-specific toxicities with ^{131}I-mIBG therapy.

Additionally, these findings provide further evidence for the clinical relevance of OCT3-mediated transport of xenobiotics in the heart and other peripheral tissues.

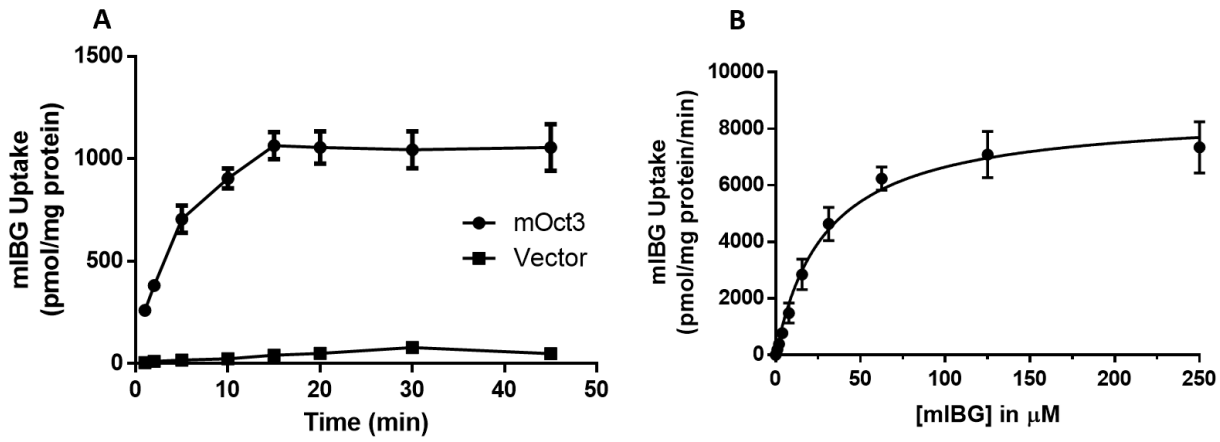

Figure 4.1. Time- and concentration-dependent uptake of mIBG by mOct3.

The time-dependent uptake of 1 μM mIBG was measured in vector control and mOct3-expressing HEK293 cells at specified time points at 37°C (A). Concentration-dependent uptake of mIBG was measured in vector control and mOct3 cells after a 2-min incubation at 37°C. Transporter-specific uptake was obtained by subtracting the activity in control cells from the activity in transporter-expressing cells (B). Non-linear regression was used to fit **Equation 4.1** to the data. Uptake was performed in triplicate in three independent experiments. Each data point represents the mean ± S.D. from all three experiments.

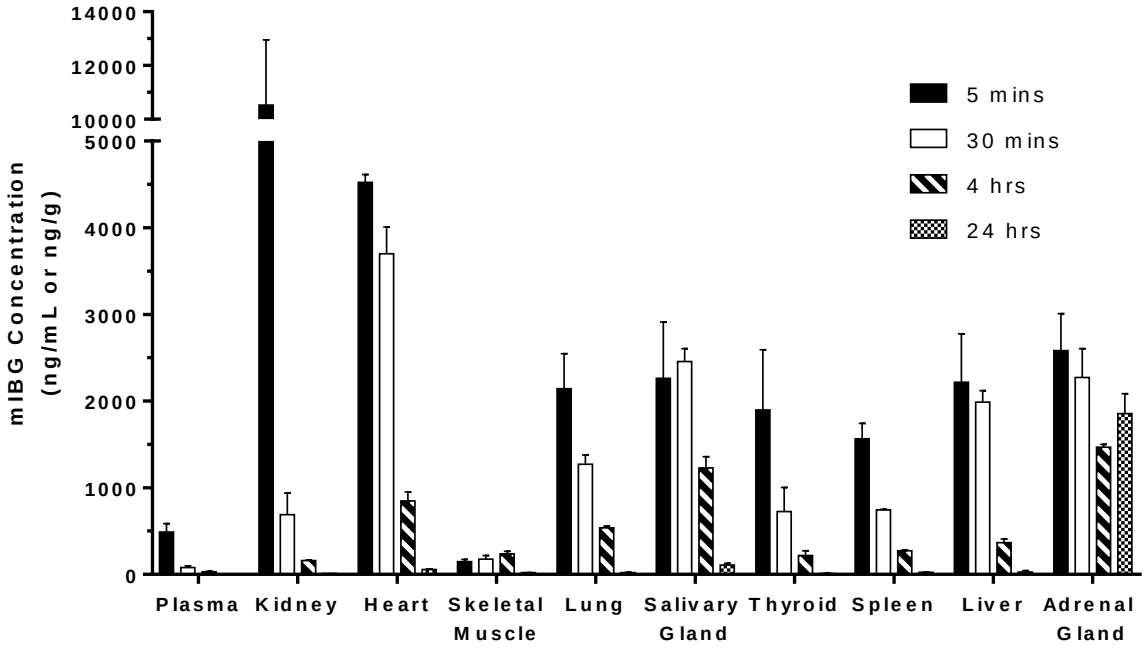

Figure 4.2. Biodistribution of mIBG in *Oct3*$^{+/+}$ mice.

The concentrations of mIBG in plasma and tissues were determined in *Oct3*$^{+/+}$ mice sacrificed after 5 mins to 24 hrs following an intravenous administration of 10 mg/kg of mIBG. The 5 min, 30 min, 4 hr, and 24 hr time points were chosen as visual representation of the concentrations in the plasma and selected tissues. Blood was collected and centrifuged at 2,000 *x g* for 10 mins at 4˚C to obtain plasma. Each tissue was homogenized with PBS and mIBG was extracted by protein precipitation, followed by quantification using LC-MS/MS. Each bar represents the mean and standard deviation from 3 mice.

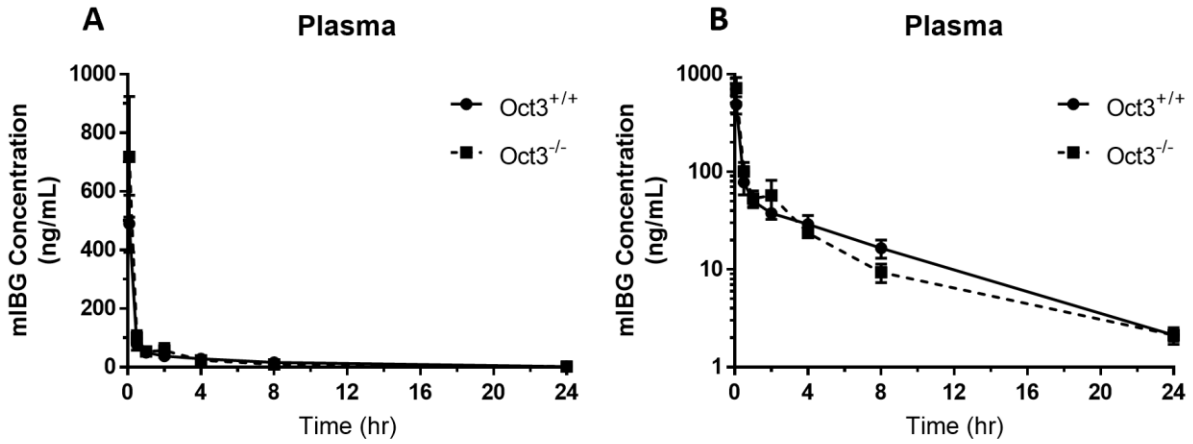

Figure 4.3. Plasma concentration-time profiles of mIBG for *Oct3*$^{+/+}$ and *Oct3*$^{-/-}$ mice.

The linear (A) and log-transformed (B) plasma concentration-time profiles of mIBG are shown. *Oct3*$^{+/+}$ (circles and solid line) and *Oct3*$^{-/-}$ (squares and dashed line) mice were administered 10 mg/kg of mIBG intravenously. Mice were sacrificed at various time points (5 mins to 24 hrs) after mIBG administration. Blood was collected and centrifuged at 2,000 *x g* for 10 mins at 4˚C to obtain plasma, followed by quantification using LC-MS/MS. Each data point represents the mean and standard deviation from 3 mice.

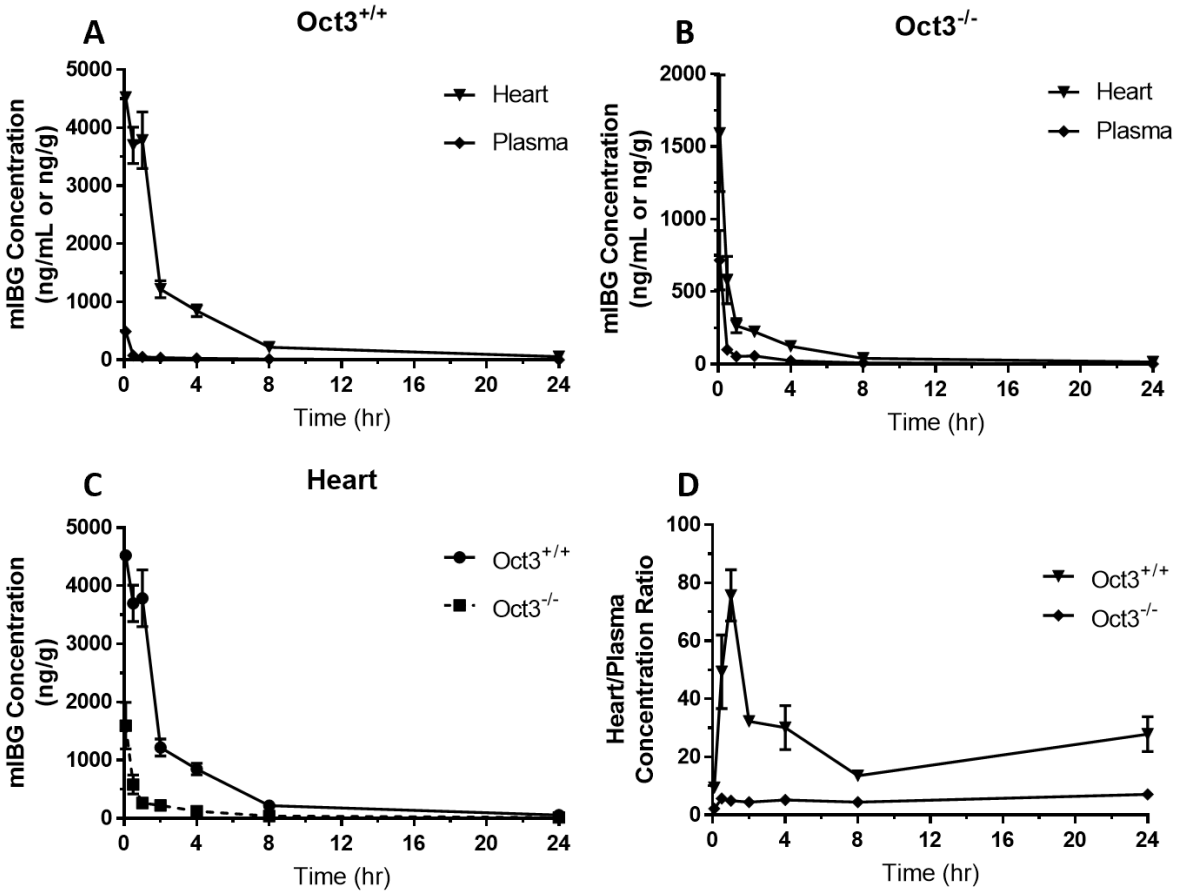

Figure 4.4. Heart concentration-time profiles of mIBG for *Oct3*$^{+/+}$ and *Oct3*$^{-/-}$ mice.

The *Oct3*$^{+/+}$ (A) and *Oct3*$^{-/-}$ (B) heart and plasma concentration-time profiles of mIBG are shown for comparison. The heart concentration-time profiles (C) in *Oct3*$^{+/+}$ (circles and solid line) and *Oct3*$^{-/-}$ (squares and dashed line) mice are shown. Concentrations of mIBG in the heart at all time points were normalized to the corresponding plasma concentrations to obtain the heart-to-plasma concentration ratio profile (D). The mice were administered 10 mg/kg of mIBG intravenously. Mice were sacrificed at various time points (5 mins to 24 hrs) after mIBG administration. The heart was collected, snap-frozen, and homogenized at a ratio of 1:6 tissue weight to volume of PBS. mIBG was extracted by protein precipitation and was quantified using LC-MS/MS. Each data point represents the mean and standard deviation of 3 mice.

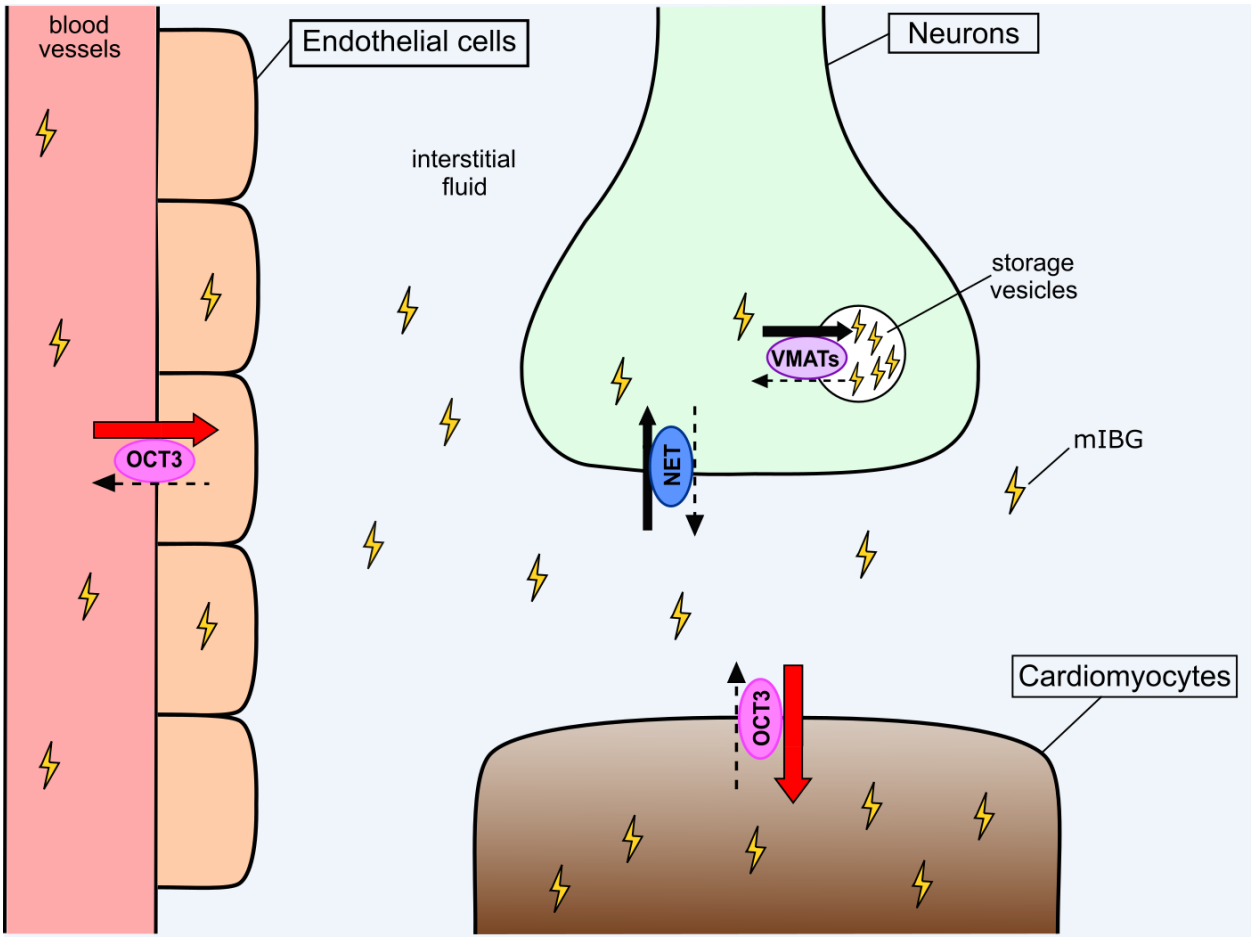

Figure 4.5. Proposed model for OCT3-mediated transport of mIBG in the neurons, cardiomyocytes, and endothelial cells in the heart.

Based on OCT3 expression and localization data, OCT3 is expressed in cardiomyocytes and vascular endothelial cells. In the cardiomyocytes, OCT3 may mediate the uptake and accumulation of mIBG within the heart. Alternatively, OCT3 on the endothelial cells may mediate mIBG uptake into the heart. As OCT3 can act as a bidirectional transporter, OCT3 may also contribute to the efflux of mIBG out of the cardiomyocytes and the endothelial cells. At neuronal sites, mIBG is actively transported into the neurons by NET and is subsequently stored in the storage vesicles by VMATs.

Table 4.1. Plasma pharmacokinetic parameters of mIBG for *Oct3*$^{+/+}$ and *Oct3*$^{-/-}$ mice. Data are presented as the mean estimate with the 95% confidence interval in parentheses. Statistical significance was determined between genotypes for each parameter using a permutation test with Bonferroni correction for multiple comparisons. The differences in each parameter between each genotype were not statistically significant (p value > 0.05).

Parameter	*Oct3*$^{+/+}$	*Oct3*$^{-/-}$
$AUC_{0-\infty}$ (μg×hr/mL)	0.55 (0.49 – 0.65)	0.58 (0.46 – 0.68)
$t_{1/2,\beta}$ (hr)	3.38 (2.87 – 3.85)	2.57 (2.15 – 3.08)
CL (L/hr/kg)	17.6 (14.8 – 19.7)	16.8 (14.2 – 20.4)
V_{ss} (L/kg)	85.9 (70.3 – 101)	62.2 (44.3 – 90.1)

Table 4.2. Tissue $AUC_{0\text{-}24\ hrs}$ in *Oct3*$^{+/+}$ and *Oct3*$^{-/-}$ mice.

Data are presented as mean with the 95% confidence interval in parentheses. Statistical significance was determined between genotypes in each tissue using a permutation test with Bonferroni correction for multiple comparisons. The differences in AUC in the heart, skeletal muscle, salivary glands, and lung were statistically significant (*** p value < 0.001) between the genotypes. The AUC difference between the genotypes in the thyroid, spleen, adrenal glands, liver, and kidney were not statistically significant (p value > 0.05).

Tissue	*Oct3*$^{+/+}$ (µg×hr/g)	*Oct3*$^{-/-}$ (µg×hr/g)	Change (%)
Heart	12.7 (11.8 – 13.5)	2.10 (1.86 – 2.33)	↓ 83 ***
Skeletal Muscle	2.50 (2.21 – 2.82)	0.83 (0.60 – 1.00)	↓ 67 ***
Salivary Glands	15.1 (13.5 – 16.1)	9.69 (7.98 – 10.8)	↓ 36 ***
Lung	6.22 (5.77 – 6.70)	4.30 (3.89 – 4.61)	↓ 31 ***
Thyroid	3.55 (2.89 – 4.42)	2.50 (1.89 – 3.18)	↓ 30
Spleen	4.04 (3.89 – 4.23)	3.52 (2.57 – 4.32)	↓ 13
Adrenal Glands	52.3 (47.4 – 61.0)	45.7 (29.2 – 62.0)	↓ 13
Liver	5.80 (5.49 – 6.24)	5.36 (4.83 – 5.75)	↓ 8
Kidney	4.96 (1.98 – 7.41)	5.10 (2.41 – 7.51)	↑ 3

Chapter 5. CONCLUSIONS AND FUTURE DIRECTIONS

Radio-iodinated *meta*-iodobenzylguanidine (mIBG) is used for the diagnosis and treatment of neuroendocrine cancers, as well as an imaging tool of the sympathetically innervated heart (Parisi et al., 2016; Pryma et al., 2019; Wan and Travin, 2020). Scintigraphic images of ^{123}I-mIBG reveal rapid urinary elimination and extensive accumulation of mIBG in normal tissues (Chin et al., 2014). Understanding the mechanisms of transport involved in the disposition of mIBG is important for optimizing the efficacy of ^{131}I-mIBG targeted therapy and minimizing tissue-specific toxicities due to radiation exposure. This dissertation research focused on understanding the role of the polyspecific organic cation transporters and their influence on the disposition, interactions, and tissue-specific toxicity of mIBG. The studies were designed to: 1) characterize the uptake kinetics of the polyspecific organic cation transporters and the role of these transporters in the disposition of mIBG; 2) develop an *in vivo* quantification method of mIBG in biological matrices; 3) elucidate the impact of OCT3 on the pharmacokinetics and tissue distribution of mIBG.

In Chapter 2, we showed that mIBG was efficiently transported by hOCT1-3 and hMATE1/2-K with comparable uptake kinetics to NET. Furthermore, we demonstrated that mIBG was transported across a hOCT2/hMATE1 double-transfected MDCK monolayer, suggesting that the hOCT2/hMATE pathway is involved in renal secretion of mIBG. Inhibition by pyrimethamine dramatically decreased the calculated apparent permeability in the hOCT2/hMATE1 pathway, indicating that inhibition of renal secretion may alter the elimination of mIBG from the body. Based on its hOCT2/hMATE transport, ^{123}I-mIBG could be used as a marker to study renal secretion *in vivo* using scintigraphic imaging as changes to the bladder, kidney, and systemic exposure due to drug-drug interactions can be visualized and assessed. Studies in Oct1/2 double

knockout mouse models with non-radiolabeled or radiolabeled mIBG can further test the potential for mIBG as an *in vivo* probe of renal secretory function. Lastly, we screened 23 anticancer drugs to see if any of these drugs affect the renal secretion of mIBG. Although we found little to no inhibition with most drugs, the preferential inhibition of OCT3-mediated uptake of mIBG by crizotinib suggests that crizotinib may block peripheral uptake of ^{131}I-mIBG, without affecting mIBG systemic elimination or its tumor uptake. The potential to minimize ^{131}I-mIBG toxicity with a compound that can inhibit the off-target tissue transport of mIBG requires further *in vivo* preclinical and human studies.

In Chapter 3, we developed a bioanalytical LC-MS/MS method for the quantification of non-radiolabeled mIBG in biological matrices. We showed that mIBG can be extracted from plasma and liver homogenate samples with a protein precipitation with acetonitrile, followed by drying with N_2 gas and a reconstitution step in a 96-well format. The method was validated based on the bioanalytical method validation guidance from the US FDA (Food and Drug Administration, 2018). We demonstrated that the method was selective, specific, linear, and had acceptable precision and accuracy at all tested concentrations. Additionally, we showed that there was no matrix effect or changes to the recovery in the different matrices. This quantification method offers unique precision and safety advantages and can be used to support mIBG pharmacokinetic and mechanistic studies in preclinical animal models using non-radiolabeled mIBG.

In Chapter 4, we showed that the mouse ortholog of OCT3 efficiently transported mIBG with comparable uptake kinetics to hOCT3. With the quantification method developed in Chapter 3, we showed that intact mIBG, rather than just the free iodine dissociating from radiolabeled mIBG, distributed to the thyroid. The lack of change in thyroid transport of mIBG with deletion

of *Oct3* suggested that other transporters may be involved in the disposition of mIBG that we have not considered. An interesting candidate is *SLC35F2* that is highly expressed in various cancers and is expressed in normal thyroid and salivary glands (Nishimura et al., 2009). *SLC35F2* transports YM155, a cationic drug that suppresses survivin (Winter et al., 2014). It would be interesting to see if *SLC35F2* transports mIBG and if the transport characteristics are similar or dissimilar to mIBG transport by NET and OCTs.

We also demonstrated that OCT3 does not affect the plasma pharmacokinetics of mIBG. Most importantly, the changes in heart exposure were the most exciting data derived from this study. We showed that majority (>80%) of the accumulation of mIBG in the heart is abrogated by the deletion of *Oct3*, indicating that OCT3 is a key facilitator of mIBG accumulation in the heart. This dramatic reduction of cardiac exposure to mIBG in *Oct3* knockout mice was quite remarkable. Previous organic cations like metformin and MPP+ have decreased heart uptake with deletion of *Oct3*, but not at the levels we observed with mIBG. Our study was limited by the fact that we homogenized the heart and treated it as a homogenous organ though the heart is composed of many different cell types. It would be important to confirm the major heart cell types that express OCT3 and would be the main targets of mIBG uptake and toxicity. Solidifying the role of OCT3 in heart uptake and accumulation would be paramount in understanding and interpreting results of cardiac ^{123}I-mIBG scintigraphic images. Further studies in mice and with human samples can help in creating a full picture of the distribution of mIBG in the heart involving OCT3 and other transporters like NET, MATE1, and MRPs. Moreover, elucidating the role of OCT3 in polymorphic populations would answer whether variants of OCT3 with reduced activity leads to changes to heart accumulation in humans and whether neuroendocrine cancer patients with these polymorphisms exhibit lower incidence and severity of cardiac toxicities. We found that OCT3

played a role in mIBG accumulation in the skeletal muscle, salivary glands, and the lung in mice. Targeting OCT3-mediated uptake of mIBG can lead to drastic changes in the tissue exposure that may lead to reduced toxicities of ^{131}I-mIBG therapy. Lastly, mIBG may be used as a selective and sensitive *in vitro* and *in vivo* probe of the OCTs and MATEs. mIBG exhibits minimal metabolism, has no toxicities, and does not interact with adrenergic receptors, thus ^{123}I-mIBG may be used as a non-invasive imaging agent to detect changes in tissue concentrations and exposures due to OCT/MATE transport. These characteristics are worthwhile in exploring clinical DDIs with ^{123}I-mIBG as a substrate.

In summary, this dissertation research has contributed greatly to our understanding of the molecular mechanisms underlying systemic and tissue-specific mIBG disposition. My research demonstrated that the polyspecific organic cation transporters facilitate the elimination and physiological tissue distribution of mIBG. Significant gaps in knowledge on how mIBG distributes in the heart cells need to be addressed. A major finding from my research is the discovery of OCT3 as a key facilitator of mIBG accumulation in the heart and other tissues. These findings have practical and translational values to help develop clinical strategies to improve the diagnostic and therapeutic efficacy of mIBG in neuroendocrine cancers and other diseases.

BIBLIOGRAPHY

Anderson GH, Jr., Blakeman N and Streeten DH (1994) The effect of age on prevalence of secondary forms of hypertension in 4429 consecutively referred patients. *J Hypertens* **12**(5): 609-615.

Anderson JL, Patterson E, Wagner JG, Stewart JR, Behm HL and Lucchesi BR (1980) Oral and intravenous bretylium disposition. *Clinical Pharmacology and Therapeutics* **28**(4): 468-478.

Balis FM, Thompson PA, Mosse YP, Blaney SM, Minard CG, Weigel BJ and Fox E (2017) First-dose and steady-state pharmacokinetics of orally administered crizotinib in children with solid tumors: a report on ADVL0912 from the Children's Oncology Group Phase 1/Pilot Consortium. *Cancer Chemother Pharmacol* **79**(1): 181-187.

Barrett JA, Joyal JL, Hillier SM, Maresca KP, Femia FJ, Kronauge JF, Boyd M, Mairs RJ and Babich JW (2010) Comparison of High-Specific-Activity Ultratrace 123/131I-MIBG and Carrier-Added 123/131I-MIBG on Efficacy, Pharmacokinetics, and Tissue Distribution. *Cancer Biotherapy and Radiopharmaceuticals* **25**(3): 299-308.

Bayer M, Kuçi Z, Schömig E, Gründemann D, Dittmann H, Handgretinger R and Bruchelt G (2009) Uptake of mIBG and catecholamines in noradrenaline- and organic cation transporter-expressing cells: potential use of corticosterone for a preferred uptake in neuroblastoma- and pheochromocytoma cells. *Nuclear Medicine and Biology* **36**(3): 287-294.

Bayer M, Schmitt J, Dittmann H, Handgretinger R, Bruchelt G and Sauter AW (2016) Improved selectivity of mIBG uptake into neuroblastoma cells in vitro and in vivo by inhibition of organic cation transporter 3 uptake using clinically approved corticosteroids. *Nuclear Medicine and Biology* **43**(9): 543-551.

Beierwaltes WH (1987) Update on basic research and clinical experience with metaiodobenzylguanidine. *Med Pediatr Oncol* **15**(4): 163-169.

Beierwaltes WH, Wieland DM, Yu T, Swanson DP and Mosley ST (1978) Adrenal imaging agents: rationale, synthesis, formulation and, metabolism. *Semin Nucl Med* **8**(1): 5-21.

Belzer M, Morales M, Jagadish B, Mash EA and Wright SH (2013) Substrate-Dependent Ligand Inhibition of the Human Organic Cation Transporter OCT2. *Journal of Pharmacology and Experimental Therapeutics* **346**(2): 300-310.

Biasotti S, Garaventa A, Villavecchia GP, Cabria M, Nantron M and De Bernardi B (2000) False-negative metaiodobenzylguanidine scintigraphy at diagnosis of neuroblastoma. *Med Pediatr Oncol* **35**(2): 153-155.

Blake GM, Lewington VJ, Zivanovic MA and Ackery DM (1989) Glomerular filtration rate and the kinetics of 123I-metaiodobenzylguanidine. *Eur J Nucl Med* **15**(9): 618-623.

Bleeker G, Schoot RA, Caron HN, De Kraker J, Hoefnagel CA, Van Eck BL and Tytgat GA (2013) Toxicity of upfront 131I-metaiodobenzylguanidine (131I-MIBG) therapy in newly diagnosed neuroblastoma patients: a retrospective analysis. *European Journal of Nuclear Medicine and Molecular Imaging* **40**(11): 1711-1717.

Blom T, Meinsma R, Rutgers M, Buitenhuis C, Dekken-Van Den Burg M, Van Kuilenburg ABP and Tytgat GAM (2020) Selective serotonin reuptake inhibitors (SSRIs) prevent meta-iodobenzylguanidine (MIBG) uptake in platelets without affecting neuroblastoma tumor uptake. *EJNMMI Research* **10**(1).

Bousvaros GA (1962) EFFECTS OF NOREPINEPHRINE ON HUMAN PULMONARY CIRCULATION. *Heart* **24**(6): 738-744.

Bresler SC, Weiser DA, Huwe PJ, Park JH, Krytska K, Ryles H, Laudenslager M, Rappaport EF, Wood AC, McGrady PW, Hogarty MD, London WB, Radhakrishnan R, Lemmon MA and Mosse YP (2014) ALK mutations confer differential oncogenic activation and sensitivity to ALK inhibition therapy in neuroblastoma. *Cancer Cell* **26**(5): 682-694.

Brouwer KL, Keppler D, Hoffmaster KA, Bow DA, Cheng Y, Lai Y, Palm JE, Stieger B, Evers R and International Transporter C (2013) In vitro methods to support transporter evaluation in drug discovery and development. *Clin Pharmacol Ther* **94**(1): 95-112.

Carr EA, Gleason G, Shaw J and Krontz B (1964) The direct diagnosis of myocardial infarction by photoscanning after administration of cesium-131. *American Heart Journal* **68**(5): 627-636.

Chabot GG (1997) Clinical Pharmacokinetics of Irinotecan. *Clinical Pharmacokinetics* **33**(4): 245-259.

Chin BB, Kronauge JF, Femia FJ, Chen J, Maresca KP, Hillier S, Petry NA, James OG, Oldan JD, Armor T, Stubbs JB, Stabin MG and Babich JW (2014) Phase-1 Clinical Trial Results of High-Specific-Activity Carrier-Free 123I-Iobenguane. *Journal of Nuclear Medicine* **55**(5): 765-771.

Coleman RE, Stubbs JB, Barrett JA, de la Guardia M, Lafrance N and Babich JW (2009) Radiation dosimetry, pharmacokinetics, and safety of ultratrace Iobenguane I-131 in patients with malignant pheochromocytoma/paraganglioma or metastatic carcinoid. *Cancer Biother Radiopharm* **24**(4): 469-475.

Counsell RE, Yu T, Ranade VV, Buswink AA, Carr EA, Jr. and Carroll M (1974) Radioiodinated bretylium analogs for myocardial scanning. *J Nucl Med* **15**(11): 991-996.

Cousineau D, Rose CP and Goresky CA (1980) Labeled catecholamine uptake in the dog heart. Interactions between capillary wall and sympathetic nerve uptake. *Circulation Research* **47**(3): 329-338.

Dae MW, De Marco T, Botvinick EH, O'Connell JW, Hattner RS, Huberty JP and Yuen-Green MS (1992) Scintigraphic assessment of MIBG uptake in globally denervated human and canine hearts--implications for clinical studies. *J Nucl Med* **33**(8): 1444-1450.

Dahlin A, Xia L, Kong W, Hevner R and Wang J (2007) Expression and immunolocalization of the plasma membrane monoamine transporter in the brain. *Neuroscience* **146**(3): 1193-1211.

de Kraker J, Hoefnagel KA, Verschuur AC, van Eck B, van Santen HM and Caron HN (2008) Iodine-131-metaiodobenzylguanidine as initial induction therapy in stage 4 neuroblastoma patients over 1 year of age. *Eur J Cancer* **44**(4): 551-556.

Degrado TR, Zalutsky MR and Vaidyanathan G (1995) Uptake mechanisms of meta-[123I]iodobenzylguanidine in isolated rat heart. *Nuclear Medicine and Biology* **22**(1): 1-12.

Dhingra J and Halkar R (2020) I-131 MIBG therapy has been used as the first line therapy in pheochromocytoma. *Journal of Nuclear Medicine* **61**: 1452.

Duan H and Wang J (2010) Selective Transport of Monoamine Neurotransmitters by Human Plasma Membrane Monoamine Transporter and Organic Cation Transporter 3. *Journal of Pharmacology and Experimental Therapeutics* **335**(3): 743-753.

Duan H and Wang J (2013) Impaired Monoamine and Organic Cation Uptake in Choroid Plexus in Mice with Targeted Disruption of the Plasma Membrane Monoamine Transporter (Slc29a4) Gene. *Journal of Biological Chemistry* **288**(5): 3535-3544.

Dubois SG, Geier E, Batra V, Yee SW, Neuhaus J, Segal M, Martinez D, Pawel B, Yanik G, Naranjo A, London WB, Kreissman S, Baker D, Attiyeh E, Hogarty MD, Maris JM, Giacomini K and Matthay KK (2012) Evaluation of Norepinephrine Transporter Expression and Metaiodobenzylguanidine Avidity in Neuroblastoma: A Report from the Children's Oncology Group. *Int J Mol Imaging* **2012**: 250834.

DuBois SG, Groshen S, Park JR, Haas-Kogan DA, Yang X, Geier E, Chen E, Giacomini K, Weiss B, Cohn SL, Granger MM, Yanik GA, Hawkins R, Courtier J, Jackson H, Goodarzian F, Shimada H, Czarnecki S, Tsao-Wei D, Villablanca JG, Marachelian A and Matthay KK (2015) Phase I Study of Vorinostat as a Radiation Sensitizer with 131I-Metaiodobenzylguanidine (131I-MIBG) for Patients with Relapsed or Refractory Neuroblastoma. *Clin Cancer Res* **21**(12): 2715-2721.

DuBois SG, Kalika Y, Lukens JN, Brodeur GM, Seeger RC, Atkinson JB, Haase GM, Black CT, Perez C, Shimada H, Gerbing R, Stram DO and Matthay KK (1999) Metastatic sites in stage IV and IVS neuroblastoma correlate with age, tumor biology, and survival. *J Pediatr Hematol Oncol* **21**(3): 181-189.

Dutt M, Wehrle CJ and Jialal I (2021) Physiology, Adrenal Gland, in *StatPearls*, Treasure Island (FL).

Ehninger G, Klingebiel T, Kumbier I, Schuler U, Feine U, Treuner J and Waller HD (1987) Stability and pharmacokinetics of m-[131I]iodobenzylguanidine in patients. *Cancer Res* **47**(22): 6147-6149.

Eisenhofer G (2001) The role of neuronal and extraneuronal plasma membrane transporters in the inactivation of peripheral catecholamines. *Pharmacol Ther* **91**(1): 35-62.

Eisenhofer G, Goldstein DS, Walther MM, Friberg P, Lenders JWM, Keiser HR and Pacak K (2003) Biochemical Diagnosis of Pheochromocytoma: How to Distinguish True- from False-Positive Test Results. *The Journal of Clinical Endocrinology & Metabolism* **88**(6): 2656-2666.

Engel K and Wang J (2005) Interaction of Organic Cations with a Newly Identified Plasma Membrane Monoamine Transporter. *Molecular Pharmacology* **68**(5): 1397-1407.

Engel K, Zhou M and Wang J (2004) Identification and characterization of a novel monoamine transporter in the human brain. *J Biol Chem* **279**(48): 50042-50049.

Floerl S, Kuehne A and Hagos Y (2020) Functional and Pharmacological Comparison of Human, Mouse, and Rat Organic Cation Transporter 1 toward Drug and Pesticide Interaction. *International Journal of Molecular Sciences* **21**(18): 6871.

Food and Drug Administration US (2018) Bioanalytical Method Validation Guidance for Industry

Food and Drug Administration US (2020) In Vitro Drug Interaction Studies — Cytochrome P450 Enzyme- and Transporter-Mediated Drug Interactions Guidance for Industry.

Fowler JS, Wolf AP, Christman DR, MacGregor RR, Ansari A and Atkins H (1975) Carrier-Free 11C-labeled catecholamines in nuclear medicine and biochemical research, in *Radiopharmaceuticals* pp 196-204.

Friedman NC, Hassan A, Grady E, Matsuoka DT and Jacobson AF (2014) Efficacy of Thyroid Blockade on Thyroid Radioiodine Uptake in 123I-mIBG Imaging. *Journal of Nuclear Medicine* **55**(2): 211-215.

Gasser PJ, Hurley MM, Chan J and Pickel VM (2017) Organic cation transporter 3 (OCT3) is localized to intracellular and surface membranes in select glial and neuronal cells within the basolateral amygdaloid complex of both rats and mice. *Brain Structure and Function* **222**(4): 1913-1928.

Gebhard C (2018) Imaging of cardiac sympathetic activity in heart failure: Not out of the woods yet. *Journal of Nuclear Cardiology* **25**(4): 1172-1177.

Giacomini KM, Huang SM, Tweedie DJ, Benet LZ, Brouwer KL, Chu X, Dahlin A, Evers R, Fischer V, Hillgren KM, Hoffmaster KA, Ishikawa T, Keppler D, Kim RB, Lee CA, Niemi M, Polli JW, Sugiyama Y, Swaan PW, Ware JA, Wright SH, Yee SW, Zamek-Gliszczynski MJ and Zhang L (2010) Membrane transporters in drug development. *Nat Rev Drug Discov* **9**(3): 215-236.

Giros B, El Mestikawy S, Bertrand L and Caron MG (1991) Cloning and functional characterization of a cocaine-sensitive dopamine transporter. *FEBS Letters* **295**(1-3): 149-154.

Glowniak JV, Kilty JE, Amara SG, Hoffman BJ and Turner FE (1993) Evaluation of metaiodobenzylguanidine uptake by the norepinephrine, dopamine and serotonin transporters. *J Nucl Med* **34**(7): 1140-1146.

Gong L, Goswami S, Giacomini KM, Altman RB and Klein TE (2012) Metformin pathways. *Pharmacogenetics and Genomics* **22**(11): 820-827.

Gorboulev V, Ulzheimer JC, Akhoundova A, Ulzheimer-Teuber I, Karbach U, Quester S, Baumann C, Lang F, Busch AE and Koepsell H (1997) Cloning and characterization of two human polyspecific organic cation transporters. *DNA Cell Biol* **16**(7): 871-881.

Gordan R, Gwathmey JK and Xie L-H (2015) Autonomic and endocrine control of cardiovascular function. *World Journal of Cardiology* **7**(4): 204.

Gordon I, Peters AM, Gutman A, Morony S, Dicks-Mireaux C and Pritchard J (1990) Skeletal assessment in neuroblastoma--the pitfalls of iodine-123-MIBG scans. *J Nucl Med* **31**(2): 129-134.

Graefe KH, Bossle F, Wolfel R, Burger A, Souladaki M, Bier D, Dutschka K, Farahati J and Bonisch H (1999) Sympathomimetic effects of MIBG: comparison with tyramine. *J Nucl Med* **40**(8): 1342-1351.

Grube M, Ameling S, Noutsias M, Köck K, Triebel I, Bonitz K, Meissner K, Jedlitschky G, Herda LR, Reinthaler M, Rohde M, Hoffmann W, Kühl U, Schultheiss H-P, Völker U, Felix SB, Klingel K, Kandolf R and Kroemer HK (2011) Selective Regulation of Cardiac Organic Cation Transporter Novel Type 2 (OCTN2) in Dilated Cardiomyopathy. *The American Journal of Pathology* **178**(6): 2547-2559.

Gründemann D, Schechinger B, Rappold G and Schömig E (1998) Molecular identification of the corticosterone-sensitive extraneuronal catecholamine transporter. *Nature Neuroscience* **1**(5): 349-351.

Gu H, Wall SC and Rudnick G (1994) Stable expression of biogenic amine transporters reveals differences in inhibitor sensitivity, kinetics, and ion dependence. *Journal of Biological Chemistry* **269**(10): 7124-7130.

Hiasa M, Matsumoto T, Komatsu T and Moriyama Y (2006) Wide variety of locations for rodent MATE1, a transporter protein that mediates the final excretion step for toxic organic cations. *Am J Physiol Cell Physiol* **291**(4): C678-686.

Hoffman BJ, Hansson SR, Mezey É and Palkovits M (1998) Localization and Dynamic Regulation of Biogenic Amine Transporters in the Mammalian Central Nervous System. *Frontiers in Neuroendocrinology* **19**(3): 187-231.

Höltje M, Winter S, Walther D, Pahner I, Hörtnagl H, Ottersen OP, Bader M and Ahnert-Hilger G (2003) The Vesicular Monoamine Content Regulates VMAT2 Activity through Gαq in Mouse Platelets. *Journal of Biological Chemistry* **278**(18): 15850-15858.

Huang KM, Zavorka Thomas M, Magdy T, Eisenmann ED, Uddin ME, DiGiacomo DF, Pan A, Keiser M, Otter M, Xia SH, Li Y, Jin Y, Fu Q, Gibson AA, Bonilla IM, Carnes CA, Corps KN, Coppola V, Smith SA, Addison D, Nies AT, Bundschuh R, Chen T, Lustberg MB, Wang J, Oswald S, Campbell MJ, Yan PS, Baker SD, Hu S, Burridge PW and Sparreboom A (2021) Targeting OCT3 attenuates doxorubicin-induced cardiac injury. *Proc Natl Acad Sci U S A* **118**(5).

Ingoglia F, Visigalli R, Rotoli BM, Barilli A, Riccardi B, Puccini P and Dall'Asta V (2015) Functional characterization of the organic cation transporters (OCTs) in human airway pulmonary epithelial cells. *Biochimica et Biophysica Acta (BBA) - Biomembranes* **1848**(7): 1563-1572.

Irwin MS and Park JR (2015) Neuroblastoma: paradigm for precision medicine. *Pediatr Clin North Am* **62**(1): 225-256.

Ito S, Kusuhara H, Yokochi M, Toyoshima J, Inoue K, Yuasa H and Sugiyama Y (2012) Competitive inhibition of the luminal efflux by multidrug and toxin extrusions, but not basolateral uptake by organic cation transporter 2, is the likely mechanism underlying the pharmacokinetic drug-drug interactions caused by cimetidine in the kidney. *J Pharmacol Exp Ther* **340**(2): 393-403.

Jacobson AF and Travin MI (2015) Impact of medications on mIBG uptake, with specific attention to the heart: Comprehensive review of the literature. *Journal of Nuclear Cardiology* **22**(5): 980-993.

Jaki T and Wolfsegger MJ (2011) Estimation of pharmacokinetic parameters with the R package PK. *Pharmaceutical Statistics* **10**(3): 284-288.

Janoueix-Lerosey I, Lequin D, Brugieres L, Ribeiro A, de Pontual L, Combaret V, Raynal V, Puisieux A, Schleiermacher G, Pierron G, Valteau-Couanet D, Frebourg T, Michon J, Lyonnet S, Amiel J and Delattre O (2008) Somatic and germline activating mutations of the ALK kinase receptor in neuroblastoma. *Nature* **455**(7215): 967-970.

Johnson K, McGlynn B, Saggio J, Baniewicz D, Zhuang H, Maris JM and Mosse YP (2011) Safety and efficacy of tandem 131I-metaiodobenzylguanidine infusions in relapsed/refractory neuroblastoma. *Pediatr Blood Cancer* **57**(7): 1124-1129.

Jonker JW, Wagenaar E, Mol CA, Buitelaar M, Koepsell H, Smit JW and Schinkel AH (2001) Reduced hepatic uptake and intestinal excretion of organic cations in mice with a targeted disruption of the organic cation transporter 1 (Oct1 [Slc22a1]) gene. *Mol Cell Biol* **21**(16): 5471-5477.

Kasama S, Toyama T and Kurabayashi M (2016) Usefulness of Cardiac Sympathetic Nerve Imaging Using ¹²³Iodine-Metaiodobenzylguanidine Scintigraphy for Predicting Sudden Cardiac Death in Patients With Heart Failure. *International Heart Journal* **57**(2): 140-144.

Kimelberg HK and Katz DM (1985) High-affinity uptake of serotonin into immunocytochemically identified astrocytes. *Science* **228**(4701): 889-891.

Kitamura Y, Baba S, Isoda T, Maruoka Y, Sasaki M, Kamitani T, Koga Y, Kawakubo N, Matsuura T and Ishigami K (2021) 123I metaiodobenzylguanidine (MIBG) uptake predicts early relapse of neuroblastoma using semi-quantitative SPECT/CT analysis. *Annals of Nuclear Medicine*.

Kline RC, Swanson DP, Wieland DM, Thrall JH, Gross MD, Pitt B and Beierwaltes WH (1981) Myocardial imaging in man with I-123 meta-iodobenzylguanidine. *J Nucl Med* **22**(2): 129-132.

Kobayashi M, Mizutani A, Nishi K, Muranaka Y, Nishii R, Shikano N, Nakanishi T, Tamai I, Kleinerman ES and Kawai K (2020) [(131)I]MIBG exports via MRP transporters and inhibition of the MRP transporters improves accumulation of [(131)I]MIBG in neuroblastoma. *Nucl Med Biol* **90-91**: 49-54.

Koehler MR, Wissinger B, Gorboulev V, Koepsell H and Schmid M (1997) The two human organic cation transporter genes SLC22A1 and SLC22A2 are located on chromosome 6q26. *Cytogenet Cell Genet* **79**(3-4): 198-200.

Koepsell H (2004) Polyspecific organic cation transporters: their functions and interactions with drugs. *Trends Pharmacol Sci* **25**(7): 375-381.

Kölby L, Bernhardt P, Levin-Jakobsen AM, Johanson V, Wängberg B, Ahlman H, Forssell-Aronsson E and Nilsson O (2003) Uptake of meta-iodobenzylguanidine in neuroendocrine tumours is mediated by vesicular monoamine transporters. *British Journal of Cancer* **89**(7): 1383-1388.

Kotecka-Blicharz A, Hasse-Lazar K, Handkiewicz-Junak D, Gawlik T, Pawlaczek A, Oczko-Wojciechowska M, Michalik B, Szpak-Ulczok S, Krajewska J, Jurecka-Lubieniecka B and Jarząb B (2018) Terapia radioizotopowa 131-MIBG złośliwych guzów chromochłonnych i przyzwojaków — badanie jednoośrodkowe. *Endokrynologia Polska* **69**(3): 246-251.

Lam AK-Y (2017) Update on Adrenal Tumours in 2017 World Health Organization (WHO) of Endocrine Tumours. *Endocrine Pathology* **28**(3): 213-227.

Lameris TW, van Den Meiracker AH, Boomsma F, Alberts G, de Zeeuw S, Duncker DJ, Verdouw PD and Veld AJ (1999) Catecholamine handling in the porcine heart: a microdialysis approach. *Am J Physiol* **277**(4): H1562-1569.

Lashford LS, Hancock JP and Kemshead JT (1991) Meta-iodobenzylguanidine (mIBG) uptake and storage in the human neuroblastoma cell line SK-N-BE(2C). *Int J Cancer* **47**(1): 105-109.

Lashford LS, Moyes J, Ott R, Fielding S, Babich J, Mellors S, Gordon I, Evans K and Kemshead JT (1988) The biodistribution and pharmacokinetics of meta-iodobenzylguanidine in childhood neuroblastoma. *Eur J Nucl Med* **13**(11): 574-577.

Lee N, Duan H, Hebert MF, Liang CJ, Rice KM and Wang J (2014) Taste of a Pill. *Journal of Biological Chemistry* **289**(39): 27055-27064.

Lee N, Hebert MF, Wagner DJ, Easterling TR, Liang CJ, Rice K and Wang J (2018) Organic Cation Transporter 3 Facilitates Fetal Exposure to Metformin during Pregnancy. *Mol Pharmacol* **94**(4): 1125-1131.

Lenders JW, Eisenhofer G, Mannelli M and Pacak K (2005) Phaeochromocytoma. *The Lancet* **366**(9486): 665-675.

Lips KS, Volk C, Schmitt BM, Pfeil U, Arndt P, Miska D, Ermert L, Kummer W and Koepsell H (2005) Polyspecific cation transporters mediate luminal release of acetylcholine from bronchial epithelium. *Am J Respir Cell Mol Biol* **33**(1): 79-88.

Liu B, Zhuang H and Servaes S (2013) Comparison of [123I]MIBG and [131I]MIBG for imaging of neuroblastoma and other neural crest tumors. *Q J Nucl Med Mol Imaging* **57**(1): 21-28.

Lo CY, Lam KY, Wat MS and Lam KS (2000) Adrenal pheochromocytoma remains a frequently overlooked diagnosis. *Am J Surg* **179**(3): 212-215.

Loh K-C, Fitzgerald PA, Matthay KK, Yeo PPB and Price DC (1997) The treatment of malignant pheochromocytoma with Iodine-131 metaiodobenzylguanidine (131I-MIBG): A comprehensive review of 116 reported patients. *Journal of Endocrinological Investigation* **20**(11): 648-658.

López Quiñones AJ, Wagner DJ and Wang J (2020) Characterization of Meta-Iodobenzylguanidine (mIBG) Transport by Polyspecific Organic Cation Transporters: Implication for mIBG Therapy. *Molecular Pharmacology* **98**(2): 109-119.

Mager H and Goller G (1998) Resampling methods in sparse sampling situations in preclinical pharmacokinetic studies. *J Pharm Sci* **87**(3): 372-378.

Mangner TJ, Tobes MC, Wieland DW, Sisson JC and Shapiro B (1986) Metabolism of iodine-131 metaiodobenzylguanidine in patients with metastatic pheochromocytoma. *J Nucl Med* **27**(1): 37-44.

Maris JM, Hogarty MD, Bagatell R and Cohn SL (2007) Neuroblastoma. *Lancet* **369**(9579): 2106-2120.

Martinez-Guerrero LJ and Wright SH (2013) Substrate-dependent inhibition of human MATE1 by cationic ionic liquids. *J Pharmacol Exp Ther* **346**(3): 495-503.

Masuda S, Terada T, Yonezawa A, Tanihara Y, Kishimoto K, Katsura T, Ogawa O and Inui K-I (2006) Identification and Functional Characterization of a New Human Kidney–Specific H+/Organic Cation Antiporter, Kidney-Specific Multidrug and Toxin Extrusion 2. *Journal of the American Society of Nephrology* **17**(8): 2127-2135.

Matthay KK, Shulkin B, Ladenstein R, Michon J, Giammarile F, Lewington V, Pearson ADJ and Cohn SL (2010) Criteria for evaluation of disease extent by 123I-metaiodobenzylguanidine scans in neuroblastoma: a report for the International Neuroblastoma Risk Group (INRG) Task Force. *British Journal of Cancer* **102**(9): 1319-1326.

Matthay KK, Tan JC, Villablanca JG, Yanik GA, Veatch J, Franc B, Twomey E, Horn B, Reynolds CP, Groshen S, Seeger RC and Maris JM (2006) Phase I Dose Escalation of Iodine-131–Metaiodobenzylguanidine With Myeloablative Chemotherapy and Autologous Stem-Cell Transplantation in Refractory Neuroblastoma: A New Approaches to Neuroblastoma Therapy Consortium Study. *Journal of Clinical Oncology* **24**(3): 500-506.

Matthay KK, Villablanca JG, Seeger RC, Stram DO, Harris RE, Ramsay NK, Swift P, Shimada H, Black CT, Brodeur GM, Gerbing RB and Reynolds CP (1999) Treatment of high-risk neuroblastoma with intensive chemotherapy, radiotherapy, autologous bone marrow transplantation, and 13-cis-retinoic acid. Children's Cancer Group. *N Engl J Med* **341**(16): 1165-1173.

Matthay KK, Yanik G, Messina J, Quach A, Huberty J, Cheng S-C, Veatch J, Goldsby R, Brophy P, Kersun LS, Hawkins RA and Maris JM (2007) Phase II Study on the Effect of Disease Sites, Age, and Prior Therapy on Response to Iodine-131-Metaiodobenzylguanidine Therapy in Refractory Neuroblastoma. *Journal of Clinical Oncology* **25**(9): 1054-1060.

Merlet P, Valette H, Dubois-Rande JL, Moyse D, Duboc D, Dove P, Bourguignon MH, Benvenuti C, Duval AM, Agostini D and et al. (1992) Prognostic value of cardiac metaiodobenzylguanidine imaging in patients with heart failure. *J Nucl Med* **33**(4): 471-477.

Metra M and Teerlink JR (2017) Heart failure. *The Lancet* **390**(10106): 1981-1995.

Modak S, Pandit-Taskar N, Kushner BH, Kramer K, Smith-Jones P, Larson S and Cheung NK (2008) Transient sialoadenitis: a complication of 131I-metaiodobenzylguanidine therapy. *Pediatr Blood Cancer* **50**(6): 1271-1273.

Mosse YP, Lim MS, Voss SD, Wilner K, Ruffner K, Laliberte J, Rolland D, Balis FM, Maris JM, Weigel BJ, Ingle AM, Ahern C, Adamson PC and Blaney SM (2013) Safety and activity of crizotinib for paediatric patients with refractory solid tumours or anaplastic large-cell lymphoma: a Children's Oncology Group phase 1 consortium study. *Lancet Oncol* **14**(6): 472-480.

Nagy A and Johansson R (1975) Plasma levels of imipramine and desipramine in man after different routes of administration. *Naunyn Schmiedebergs Arch Pharmacol* **290**(2-3): 145-160.

Nakajima K, Matsunari I and Jacobson AF (2018) I-123 metaiodobenzylguanidine innervation imaging as a tool for norepinephrine transporter research: A possible application for genetic analysis in heart failure. *Journal of Nuclear Cardiology* **25**(3): 907-910.

Nakajo M, Shapiro B, Copp J, Kalff V, Gross MD, Sisson JC and Beierwaltes WH (1983) The normal and abnormal distribution of the adrenomedullary imaging agent m-[I-131]iodobenzylguanidine (I-131 MIBG) in man: evaluation by scintigraphy. *J Nucl Med* **24**(8): 672-682.

Nakajo M, Shapiro B, Sisson JC, Swanson DP and Beierwaltes WH (1984) Salivary gland accumulation of meta-[131I]iodobenzylguanidine. *J Nucl Med* **25**(1): 2-6.

Neumann H, Berger DP, Sigmund G, Blum U, Schmidt D, Parmer RJ, Volk B and Kirste G (1993) Pheochromocytomas, Multiple Endocrine Neoplasia Type 2, and von Hippel-Lindau Disease. *New England Journal of Medicine* **329**(21): 1531-1538.

Nielsen JT, Nielsen BV and Rehling M (1996) Location of adrenal medullary pheochromocytoma by I-123 metaiodobenzylguanidine SPECT. *Clin Nucl Med* **21**(9): 695-699.

Nishimura M, Suzuki S, Satoh T and Naito S (2009) Tissue-specific mRNA expression profiles of human solute carrier 35 transporters. *Drug Metab Pharmacokinet* **24**(1): 91-99.

Otsuka M, Matsumoto T, Morimoto R, Arioka S, Omote H and Moriyama Y (2005) A human transporter protein that mediates the final excretion step for toxic organic cations. *Proc Natl Acad Sci U S A* **102**(50): 17923-17928.

Pacholczyk T, Blakely RD and Amara SG (1991) Expression cloning of a cocaine-and antidepressant-sensitive human noradrenaline transporter. *Nature* **350**(6316): 350-354.

Parisi MT, Eslamy H, Park JR, Shulkin BL and Yanik GA (2016) 131I-Metaiodobenzylguanidine Theranostics in Neuroblastoma: Historical Perspectives; Practical Applications. *Seminars in Nuclear Medicine* **46**(3): 184-202.

Parisi MT, Sandler ED and Hattner RS (1992) The biodistribution of metaiodobenzylguanidine. *Seminars in Nuclear Medicine* **22**(1): 46-48.

Park JR, Eggert A and Caron H (2008) Neuroblastoma: biology, prognosis, and treatment. *Pediatr Clin North Am* **55**(1): 97-120, x.

Peter D, Liu Y, Sternini C, De Giorgio R, Brecha N and Edwards R (1995) Differential expression of two vesicular monoamine transporters. *The Journal of Neuroscience* **15**(9): 6179-6188.

Pryma DA, Chin BB, Noto RB, Dillon JS, Perkins S, Solnes L, Kostakoglu L, Serafini AN, Pampaloni MH, Jensen J, Armor T, Lin T, White T, Stambler N, Apfel S, Dipippo VA, Mahmood S, Wong V and Jimenez C (2019) Efficacy and Safety of High-Specific-Activity 131I-MIBG Therapy in Patients with Advanced Pheochromocytoma or Paraganglioma. *Journal of Nuclear Medicine* **60**(5): 623-630.

Quach A, Ji L, Mishra V, Sznewajs A, Veatch J, Huberty J, Franc B, Sposto R, Groshen S, Wei D, Fitzgerald P, Maris JM, Yanik G, Hawkins RA, Villablanca JG and Matthay KK (2011) Thyroid and hepatic function after high-dose 131I-metaiodobenzylguanidine (131I-MIBG) therapy for neuroblastoma. *Pediatric Blood & Cancer* **56**(2): 191-201.

Raffel DM and Wieland DM (2010) Development of mIBG as a Cardiac Innervation Imaging Agent. *JACC: Cardiovascular Imaging* **3**(1): 111-116.

Ramamoorthy S, Bauman AL, Moore KR, Han H, Yang-Feng T, Chang AS, Ganapathy V and Blakely RD (1993) Antidepressant- and cocaine-sensitive human serotonin transporter: molecular cloning, expression, and chromosomal localization. *Proc Natl Acad Sci U S A* **90**(6): 2542-2546.

Rao D, Van Berkel A, Piscaer I, Young WF, Gruber L, Deutschbein T, Fassnacht M, Beuschlein F, Spyroglou A, Prejbisz A, Hanus K, Eisenhofer G, Manelli M, Canu L, Lenders JWM, Bancos I and Timmers HJLM (2019) Impact of 123I-MIBG Scintigraphy on Clinical Decision-Making in Pheochromocytoma and Paraganglioma. *The Journal of Clinical Endocrinology & Metabolism* **104**(9): 3812-3820.

Sassi Y, Abi-Gerges A, Fauconnier J, Mougenot N, Reiken S, Haghighi K, Kranias EG, Marks AR, Lacampagne A, Engelhardt S, Hatem SN, Lompre AM and Hulot JS (2012) Regulation of cAMP homeostasis by the efflux protein MRP4 in cardiac myocytes. *The FASEB Journal* **26**(3): 1009-1017.

Schomig A, Dart AM, Dietz R, Mayer E and Kubler W (1984) Release of endogenous catecholamines in the ischemic myocardium of the rat. Part A: Locally mediated release. *Circ Res* **55**(5): 689-701.

Schroeter S, Levey AI and Blakely RD (1997) Polarized Expression of the Antidepressant-Sensitive Serotonin Transporter in Epinephrine-Synthesizing Chromaffin Cells of the Rat Adrenal Gland. *Molecular and Cellular Neuroscience* **9**(3): 170-184.

Sharp SE, Trout AT, Weiss BD and Gelfand MJ (2016) MIBG in Neuroblastoma Diagnostic Imaging and Therapy. *Radiographics* **36**(1): 258-278.

Short JH and Darby TD (1967) Sympathetic nervous system blocking agents. 3. Derivatives of benzylguanidine. *J Med Chem* **10**(5): 833-840.

Shusterman S, Grant FD, Lorenzen W, Davis RT, Laffin S, Drubach LA, Fahey FH and Treves ST (2011) Iodine-131–labeled Meta-Iodobenzylguanidine Therapy of Children with Neuroblastoma: Program Planning and Initial Experience. *Seminars in Nuclear Medicine* **41**(5): 354-363.

Sisson JC, Wieland DM, Sherman P, Mangner TJ, Tobes MC and Jacques S, Jr. (1987) Metaiodobenzylguanidine as an index of the adrenergic nervous system integrity and function. *J Nucl Med* **28**(10): 1620-1624.

Solbach TF, Grube M, Fromm MF and Zolk O (2011) Organic cation transporter 3: expression in failing and nonfailing human heart and functional characterization. *J Cardiovasc Pharmacol* **58**(4): 409-417.

Sprowl JA, Ong SS, Gibson AA, Hu S, Du G, Lin W, Li L, Bharill S, Ness RA, Stecula A, Offer SM, Diasio RB, Nies AT, Schwab M, Cavaletti G, Schlatter E, Ciarimboli G, Schellens JHM, Isacoff EY, Sali A, Chen T, Baker SD, Sparreboom A and Pabla N (2016) A phosphotyrosine switch regulates organic cation transporters. *Nat Commun* **7**: 10880.

Stefanelli A, Treglia G, Bruno I, Rufini V and Giordano A (2013) Pharmacological interference with 123I-metaiodobenzylguanidine: a limitation to developing cardiac innervation imaging in clinical practice? *Eur Rev Med Pharmacol Sci* **17**(10): 1326-1333.

Streby KA, Shah N, Ranalli MA, Kunkler A and Cripe TP (2015) Nothing but NET: A review of norepinephrine transporter expression and efficacy of 131 I-mIBG therapy. *Pediatric Blood & Cancer* **62**(1): 5-11.

Talvenheimo J and Rudnick G (1980) Solubilization of the platelet plasma membrane serotonin transporter in an active form. *Journal of Biological Chemistry* **255**(18): 8606-8611.

Teresińska A (2012) Metaiodobenzylguanidine scintigraphy of cardiac sympathetic innervation. **15**(1): 61-70.

Torres GE, Gainetdinov RR and Caron MG (2003) Plasma membrane monoamine transporters: structure, regulation and function. *Nature Reviews Neuroscience* **4**(1): 13-25.

Treuner J, Gerein V, Klingebiel T, Schwabe D, Feine U, Happ J, Niethammer D, Maul F, Dopfer R, Kornhuber B and et al. (1988) MIBG-treatment in neuroblastoma; experiences of the Tubingen/Frankfurt group. *Prog Clin Biol Res* **271**: 669-678.

Trigg RM and Turner SD (2018) ALK in Neuroblastoma: Biological and Therapeutic Implications. *Cancers (Basel)* **10**(4).

Tseng YT and Padbury JF (1998) Expression of a pulmonary endothelial norepinephrine transporter. *Journal of Neural Transmission* **105**(10): 1187.

Umapathy G, Mendoza-Garcia P, Hallberg B and Palmer RH (2019) Targeting anaplastic lymphoma kinase in neuroblastoma. *APMIS* **127**(5): 288-302.

Van Santen HM, De Kraker J, Van Eck BLF, De Vijlder JJM and Vulsma T (2002) High incidence of thyroid dysfunction despite prophylaxis with potassium iodide during 131I-meta-iodobenzylguanidine treatment in children with neuroblastoma. *Cancer* **94**(7): 2081-2089.

Verberne HJ, Somsen GA, Povinec P, Van Eck-Smit BLF and Jacobson AF (2009) Impact of mediastinal, liver and lung 123I-metaiodobenzylguanidine (123I-MIBG) washout on calculated 123I-MIBG myocardial washout. *European Journal of Nuclear Medicine and Molecular Imaging* **36**(8): 1322-1328.

Verschure DO, de Wit TC, Bongers V, Hagen PJ, Sonneck-Koenne C, D'Aron J, Huber K, van Eck-Smit BL, Knoll P, Somsen GA, Mirzaei S and Verberne HJ (2015) (1)(2)(3)I-MIBG heart-to-mediastinum ratio is influenced by high-energy photon penetration of collimator septa from liver and lung activity. *Nucl Med Commun* **36**(3): 279-285.

Vik TA, Pfluger T, Kadota R, Castel V, Tulchinsky M, Farto JCA, Heiba S, Serafini A, Tumeh S, Khutoryansky N and Jacobson AF (2009) 123I-mIBG scintigraphy in patients with known or suspected neuroblastoma: Results from a prospective multicenter trial. *Pediatric Blood & Cancer* **52**(7): 784-790.

Wade P, Chen J, Jaffe B, Kassem I, Blakely R and Gershon M (1996) Localization and function of a 5-HT transporter in crypt epithelia of the gastrointestinal tract. *The Journal of Neuroscience* **16**(7): 2352-2364.

Wagner DJ, Hu T and Wang J (2016) Polyspecific organic cation transporters and their impact on drug intracellular levels and pharmacodynamics. *Pharmacol Res* **111**: 237-246.

Wagner DJ, Sager JE, Duan H, Isoherranen N and Wang J (2017) Interaction and Transport of Methamphetamine and its Primary Metabolites by Organic Cation and Multidrug and Toxin Extrusion Transporters. *Drug Metab Dispos* **45**(7): 770-778.

Wagner DJ, Shireman LM, Ahn S, Shen DD and Wang J (2018) Disposition of Methamphetamine and Major Metabolites in Mice: Role of Organic Cation Transporter 3 in Tissue-Selective Accumulation of Para-Hydroxymethamphetamine. *Drug Metabolism and Disposition* **46**(9): 1277-1284.

Wakabayashi H, Inaki A, Yoshimura K, Murayama T, Imai Y, Higuchi T, Jinguji M, Shiga T and Kinuya S (2019) A phase I clinical trial for [131I]meta-iodobenzylguanidine therapy in patients with refractory pheochromocytoma and paraganglioma. *Scientific Reports* **9**(1).

Wan N and Travin MI (2020) Cardiac Imaging With 123I-meta-iodobenzylguanidine and Analogous PET Tracers: Current Status and Future Perspectives. *Seminars in Nuclear Medicine* **50**(4): 331-348.

Ward E, DeSantis C, Robbins A, Kohler B and Jemal A (2014) Childhood and adolescent cancer statistics, 2014. *CA Cancer J Clin* **64**(2): 83-103.

Watanabe S, Hanaoka H, Liang JX, Iida Y, Endo K and Ishioka NS (2010) PET Imaging of Norepinephrine Transporter-Expressing Tumors Using 76Br-meta-Bromobenzylguanidine. *Journal of Nuclear Medicine* **51**(9): 1472-1479.

Weihe E, Schafer MK, Erickson JD and Eiden LE (1994) Localization of vesicular monoamine transporter isoforms (VMAT1 and VMAT2) to endocrine cells and neurons in rat. *J Mol Neurosci* **5**(3): 149-164.

Westfall PH and Young SS (1993) *Resampling-based multiple testing: Examples and methods for p-value adjustment*. Wiley, New York.

Wieland DM, Brown LE, Rogers WL, Worthington KC, Wu JL, Clinthorne NH, Otto CA, Swanson DP and Beierwaltes WH (1981) Myocardial imaging with a radioiodinated norepinephrine storage analog. *J Nucl Med* **22**(1): 22-31.

Wieland DM, Mangner TJ, Inbasekaran MN, Brown LE and Wu JL (1984) Adrenal medulla imaging agents: a structure-distribution relationship study of radiolabeled aralkylguanidines. *J Med Chem* **27**(2): 149-155.

Wieland DM, Wu J, Brown LE, Mangner TJ, Swanson DP and Beierwaltes WH (1980) Radiolabeled adrenergi neuron-blocking agents: adrenomedullary imaging with [131I]iodobenzylguanidine. *J Nucl Med* **21**(4): 349-353.

Willenberg HS and Bornstein SR (2000) Adrenal Cortex; Development, Anatomy, Physiology, in *Endotext* (Feingold KR, Anawalt B, Boyce A, Chrousos G, de Herder WW, Dhatariya K, Dungan K, Grossman A, Hershman JM, Hofland J, Kalra S, Kaltsas G, Koch C, Kopp P, Korbonits M, Kovacs CS, Kuohung W, Laferrere B, McGee EA, McLachlan R, Morley JE, New M, Purnell J, Sahay R, Singer F, Stratakis CA, Trence DL and Wilson DP eds), South Dartmouth (MA).

Wimalasena K (2011) Vesicular monoamine transporters: structure-function, pharmacology, and medicinal chemistry. *Med Res Rev* **31**(4): 483-519.

Winter GE, Radic B, Mayor-Ruiz C, Blomen VA, Trefzer C, Kandasamy RK, Huber KVM, Gridling M, Chen D, Klampfl T, Kralovics R, Kubicek S, Fernandez-Capetillo O, Brummelkamp TR and Superti-Furga G (2014) The solute carrier SLC35F2 enables YM155-mediated DNA damage toxicity. *Nature Chemical Biology* **10**(9): 768-773.

Wiseman GA, Pacak K, O'Dorisio MS, Neumann DR, Waxman AD, Mankoff DA, Heiba SI, Serafini AN, Tumeh SS, Khutoryansky N and Jacobson AF (2009) Usefulness of 123I-MIBG Scintigraphy in the Evaluation of Patients with Known or Suspected Primary or Metastatic Pheochromocytoma or Paraganglioma: Results from a Prospective Multicenter Trial. *Journal of Nuclear Medicine* **50**(9): 1448-1454.

Xia L, Engel K, Zhou M and Wang J (2007) Membrane localization and pH-dependent transport of a newly cloned organic cation transporter (PMAT) in kidney cells. *American Journal of Physiology-Renal Physiology* **292**(2): F682-F690.

Yanik GA, Villablanca JG, Maris JM, Weiss B, Groshen S, Marachelian A, Park JR, Tsao-Wei D, Hawkins R, Shulkin BL, Jackson H, Goodarzian F, Shimada H, Courtier J, Hutchinson R, Haas-Koga D, Hasenauer CB, Czarnecki S, Katzenstein HM and Matthay KK (2015) 131I-Metaiodobenzylguanidine with Intensive Chemotherapy and Autologous Stem Cell Transplantation for High-Risk Neuroblastoma. A New Approaches to Neuroblastoma Therapy (NANT) Phase II Study. *Biology of Blood and Marrow Transplantation* **21**(4): 673-681.

Yin J, Duan H, Shirasaka Y, Prasad B and Wang J (2015) Atenolol Renal Secretion Is Mediated by Human Organic Cation Transporter 2 and Multidrug and Toxin Extrusion Proteins. *Drug Metab Dispos* **43**(12): 1872-1881.

Yin J, Duan H and Wang J (2016) Impact of Substrate-Dependent Inhibition on Renal Organic Cation Transporters hOCT2 and hMATE1/2-K-Mediated Drug Transport and Intracellular Accumulation. *J Pharmacol Exp Ther* **359**(3): 401-410.

Yin J, Wagner DJ, Prasad B, Isoherranen N, Thummel KE and Wang J (2019) Renal secretion of hydrochlorothiazide involves organic anion transporter 1/3, organic cation transporter 2, and multidrug and toxin extrusion protein 2-K. *Am J Physiol Renal Physiol* **317**(4): F805-F814.

Zhang L, Dresser MJ, Gray AT, Yost SC, Terashita S and Giacomini KM (1997) Cloning and functional expression of a human liver organic cation transporter. *Mol Pharmacol* **51**(6): 913-921.

Zhao Q, Wei H, Liu D, Shi B, Li L, Yan M, Zhang X, Wang F and Ouyang Y (2017) PHACTR1 and SLC22A3 gene polymorphisms are associated with reduced coronary artery disease risk in the male Chinese Han population. *Oncotarget* **8**(1): 658-663.

Zhou M, Duan H, Engel K, Xia L and Wang J (2010) Adenosine Transport by Plasma Membrane Monoamine Transporter: Reinvestigation and Comparison with Organic Cations. *Drug Metabolism and Disposition* **38**(10): 1798-1805.

Zhou M, Xia L and Wang J (2007) Metformin Transport by a Newly Cloned Proton-Stimulated Organic Cation Transporter (Plasma Membrane Monoamine Transporter) Expressed in Human Intestine. *Drug Metabolism and Disposition* **35**(10): 1956-1962.

Zhu H-J, Appel DI, Gründemann D and Markowitz JS (2010) Interaction of organic cation transporter 3 (SLC22A3) and amphetamine. *Journal of Neurochemistry*: no-no.

Zwart R, Verhaagh S, Buitelaar M, Popp-Snijders C and Barlow DP (2001) Impaired Activity of the Extraneuronal Monoamine Transporter System Known as Uptake-2 inOrct3/Slc22a3-Deficient Mice. *Molecular and Cellular Biology* **21**(13): 4188-4196.

VITA

Antonio Jesús López Quiñones was born in and lived part of his childhood in Ponce, Puerto Rico where he attended Colegio El Ave María. He moved to Leander, Texas where he attended Leander High School and received his International Baccalaureate diploma. He earned his Bachelor of Science in Chemistry and Spanish with a minor in Biology from Southwestern University in Georgetown, Texas.